Dissertation

SUBMITTED TO THE
Combined Faculty of Mathematics, Engineering and Natural Sciences
of Heidelberg University, Germany

FOR THE DEGREE OF
Doctor of Natural Sciences

PUT FORWARD BY
Sebastian Jonas Geier
BORN IN: Eberbach, Germany
ORAL EXAMINATION: December 19th, 2023

Shaping the Hamiltonian of many-body spin systems on a Rydberg-atom quantum simulator

---

How periodic driving and spin-encoding states tune the dynamics of strongly interacting quantum systems

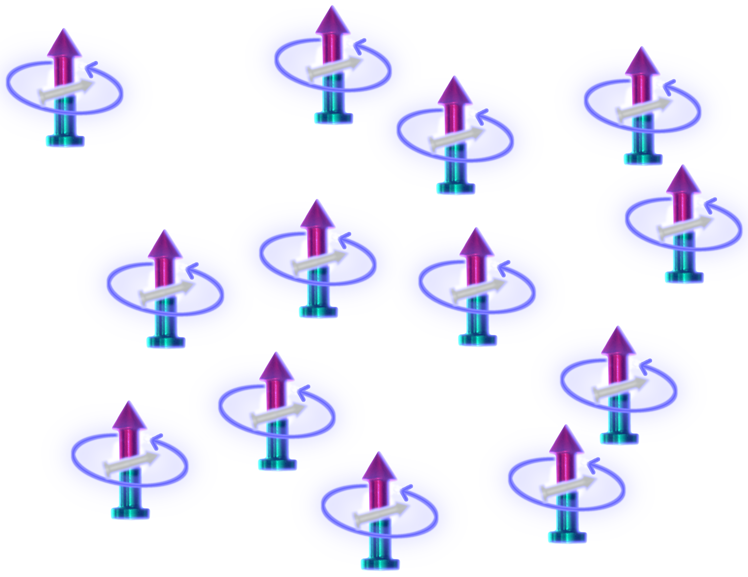

Referees: **Prof. Dr. Matthias Weidemüller**
Prof. Dr. Markus K. Oberthaler

Abstract

Quantum simulation enables the experimental investigation of simplified physical models that capture the fundamental aspects of complex quantum many-body systems. In order to understand how interaction parameters impact the macroscopic properties of the system, it is essential to modify the Hamiltonian in a controlled fashion. This thesis presents novel approaches to perform tunable quantum simulations in an isolated many-body spin-1/2 system represented by dipolar interacting Rydberg atoms. These approaches are employed to study out-of-equilibrium dynamics in different regimes. The four major achievements are as follows: (i) Using various spin-encoding states within the Rydberg manifold, we realize XX, XXZ, and Ising models with spatial disorder and study magnetization relaxation dynamics. We identify a universal behavior that is independent of the microscopic properties and explained by the emergence of effective spin pairs. (ii) To introduce new effective interactions into the system, we employ a time-periodic drive to transform the natural dipolar interaction Hamiltonian into a desired target form. This method, known as Floquet engineering, is validated using both a gas of Rydberg atoms and individually trapped Rydberg atoms. We demonstrate its potential for tunable quantum simulation of Heisenberg spin models by altering symmetry and transport properties. (iii) Combining the methods developed in (i) and (ii), we devise and implement a time reversal protocol. The versatility of the approach is demonstrated by reversing quantum dynamics for a variety of many-body Hamiltonian with tunable symmetry, which we realize through Floquet engineering. (iv) Beyond experimental demonstration, we propose alternative approaches to engineer many-body systems, including a new approach to realize time-reversal operations, and an approach for introducing mobile dopants into Rydberg spin systems. The Hamiltonian engineering methods can be directly applied to further study the extend to which the emergence of effective spin pairs is the common feature of disordered quantum spin systems. In general, engineering a wide range of Hamiltonians opens up several new opportunities for investigating fields that range from spin transport and spin glasses to quantum thermalization.

Zusammenfassung

Die Quantensimulation ermöglicht die experimentelle Untersuchung vereinfachter physikalischer Modelle, die die grundlegenden Aspekte komplexer Quanten-Vielteilchensysteme erfassen. Um zu verstehen, wie sich die Wechselwirkungsparameter auf die makroskopischen Eigenschaften des Systems auswirken, ist eine kontrollierte Manipulation des Hamiltonians unerlässlich. In dieser Arbeit werden neue Ansätze zur Durchführung von einstellbaren Quantensimulationen in einem isolierten Vielteilchen-Spin-1/2-System vorgestellt, das durch dipolar wechselwirkende Rydberg-Atome dargestellt wird. Diese Ansätze werden eingesetzt, um die Dynamik außerhalb des Gleichgewichts in verschiedenen Regimen zu untersuchen. Die vier wichtigsten Ergebnisse sind die folgenden: (i) Unter Verwendung verschiedener Spin-Kodierungszustände innerhalb der Rydberg-Mannigfaltigkeit realisieren wir XX-, XXZ- und Ising-Modelle mit räumlicher Unordnung und untersuchen die Dynamik der Magnetisierungsrelaxation. Wir identifizieren ein universelles Verhalten, das unabhängig von den mikroskopischen Eigenschaften ist und durch das Auftreten von effektiven Spinpaaren erklärt wird. (ii) Um neue effektive Wechselwirkungen in das System einzuführen, wenden wir ein zeitperiodischen Treiben an, um den natürlichen Hamiltonian der dipolaren Wechselwirkung in eine gewünschte Zielform umzuwandeln. Diese als Floquet-Engineering bekannte Methode wird sowohl mit einem Gas aus Rydberg-Atomen als auch mit einzelnen gefangenen Rydberg-Atomen validiert. Wir demonstrieren ihr Potenzial für die einstellbare Quantensimulation von Heisenberg-Spinmodellen durch Veränderung der Symmetrie und der Transporteigenschaften. (iii) Indem wir die in (i) und (ii) entwickelten Methoden kombinieren, entwickeln und implementieren wir ein Zeitumkehrprotokoll. Die Vielseitigkeit des Ansatzes wird durch die Umkehrung der Quantendynamik für eine Vielzahl von Vielteilchen-Hamiltonians mit einstellbarer Symmetrie demonstriert, die wir durch Floquet Engineering erreichen. (iv) Über die experimentelle Demonstration hinaus schlagen wir alternative Ansätze zum Engineering von Vielteilchensystemen vor, einschließlich eines neuen Ansatzes zur Realisierung von Zeitumkehroperationen und eines Ansatzes zur Einführung mobiler Defekte in Ryderg-Spinsysteme. Diese Hamiltonian Engineering-Methoden können direkt angewandt werden, um weiter zu untersuchen, inwieweit die Entstehung effektiver Spinpaare ein gemeinsames Merkmal ungeordneter Quantenspinsysteme ist. Generell eröffnet das Engineering eines breiten Spektrums von Hamiltonians zahlreiche neue Möglichkeiten für die Untersuchung von Bereichen, die von Spintransport und Spin-Gläsern bis zur Quanten-Thermalisierung reichen.

Publications

This thesis is based on the following manuscripts and publications:

- **Floquet Hamiltonian Engineering of an Isolated Many-Body Spin System**
  S. Geier*, N. Thaicharoen*, C. Hainaut*, T. Franz, A. Salzinger, A. Tebben, D. Grimshandl, G. Zürn, M. Weidemüller
  Science 374, 1149 (2021)

- **Microwave-engineering of programmable XXZ Hamiltonians in arrays of Rydberg atoms**
  P. Scholl*, H.J. Williams*, G. Bornet*, F. Wallner, D. Barredo, T. Lahaye, A. Browaeys, L. Henriet, A. Signoles, C. Hainaut, T. Franz, **S. Geier**, A. Tebben, A. Salzinger, G. Zürn, M. Weidemüller
  Phys. Rev. X Quantum 3, 020303 (2022)

- **Time-reversal in a quantum many-body spin system**
  S. Geier, A. Braemer, E. Braun, M. Müllenbach, T. Franz, M. Gärttner, G. Zürn, M. Weidemüller
  Submitted

- **Observation of universal relaxation dynamics in disordered quantum spin systems**
  T. Franz*, **S. Geier***, C. Hainaut, A. Braemer, N. Thaicharoen, M. Hornung, E. Braun, M. Gärttner, G. Zürn, M. Weidemüller
  arXiv:2209.08080 (Submitted)

The author furthermore contributed to the following publications:

- **Absence of thermalization in an interacting system of thousands of quantum spins**
  T. Franz, **S. Geier**, C. Hainaut, A. Signoles, N. Thaicharoen, A. Tebben, A. Salzinger, A. Braemer, M. Gärttner, G. Zürn, M. Weidemüller
  arXiv:2207.14216

- **Glassy quantum dynamics of disordered Ising spins**
  P. Schultzen*, T. Franz*, **S. Geier**, A. Salzinger, A. Tebben, C. Hainaut, G. Zürn, M. Weidemüller, M. Gärttner
  Phys. Rev. B 105, L020201 (2022)

- **Semiclassical simulations predict glassy dynamics for disordered Heisenberg models**
  P. Schultzen*, T. Franz*, C. Hainaut*, **S. Geier**, A. Salzinger, A. Tebben, G. Zürn, M. Gärttner, M. Weidemüller
  Phys. Rev. B 105, L100201 (2022)

- **Nonlinear absorption in interacting Rydberg electromagnetically-induced-transparency spectra on two-photon resonance**
  A. Tebben, C. Hainaut, A. Salzinger, **S. Geier**, T. Franz, T. Pohl, M. Gärttner, G. Zürn, M. Weidemüller
  Phys. Rev. A 103, 063710 (2021)

- **Measuring the Fluctuation–Dissipation Relation of Quantum Spins via Engineered Dephasing**
  A. Salzinger, K. T. Geier, T. Franz, **S. Geier**, N. Thaicharoen, A. Tebben, C. Hainaut, R. Ott, M. Gärttner, P. Hauke, G. Zürn, M. Weidemüller
  In preparation

* These authors contributed equally.

Contents

CHAPTER 1

Introduction

1.1 Quantum systems and Quantum simulators

Quantum physics, often regarded as one of the most fascinating fields of science, has fundamentally changed our understanding of nature. It predicts behaviors that often defy intuition and contradict our everyday experiences. In quantum mechanics, a single object in its simplest form can be characterized by two discrete basis states, denoted $|\downarrow\rangle$ and $|\uparrow\rangle$, which pertains, for instance, to the intrinsic angular momentum states of a particle known as *spin*. Despite being in either $|\downarrow\rangle$ or $|\uparrow\rangle$, the most general spin state can be expressed as $|\psi\rangle = c_\downarrow |\downarrow\rangle + c_\uparrow |\uparrow\rangle$. Here, $c_\downarrow$ and $c_\uparrow$ are complex numbers denoted as amplitudes. This is the principle of superposition, which allows for the unexpected possibility of a particle existing in a state with contradictory properties simultaneously. When subjected to a measurement, the particle "collapses" into one of the spin states $|\downarrow\rangle$ or $|\uparrow\rangle$ with probability $|c_\downarrow|^2$ and $|c_\uparrow|^2$, respectively. Similarly, in the case of two such particles, the most general state reads $|\psi\rangle = c_{\downarrow\downarrow} |\downarrow\downarrow\rangle + c_{\uparrow\downarrow} |\uparrow\downarrow\rangle + c_{\downarrow\uparrow} |\downarrow\uparrow\rangle + c_{\uparrow\uparrow} |\uparrow\uparrow\rangle$, where the first/second instance in the $|.\rangle$ represents the first/second particle. From this structure arises the possibility for a state $|\psi^+\rangle = \frac{|\downarrow\downarrow\rangle + |\uparrow\uparrow\rangle}{\sqrt{2}}$, known as a Bell state, which serves as a fundamental example of quantum entanglement. Two particles with entangled spin, will remain connected and correlated, regardless of their physical distance [1]. Remarkably, measuring one particle's spin state, instantaneously determines the spin state of the other particle. Such a phenomenon appears unsatisfying, and even Albert Einstein struggled with its acceptance, referring to it as *"spooky action at a distance"*.

Over the decades, our understanding of quantum physics has evolved, and seemingly unsatisfying concepts have been confirmed. Early pioneering experiments were conducted by Otto Stern and Walther Gerlach in 1922, where they demonstrated that particles indeed possess an intrinsic angular momentum that only takes a certain quantized value i.e. being $|\uparrow\rangle$ or $|\downarrow\rangle$ [2]. Similarly, groundbreaking experiments conducted by Alain Aspect, John F. Clauser, and Anton Zeilinger significantly contributed to our understanding of entangled systems, earning them the Nobel Prize in 2022 [3–5]. These and similar other achievements laid the foundation for our current understanding of quantum physics and settled many concepts.

When dealing with many interacting quantum particles, the situation changes. For systems with thousands of interacting particles, it remains an open question how complex macroscopic behaviors emerge from simple microscopic rules. This is particularly relevant for a broad range of fields, including condensed matter systems, in which quantum systems of spins reveal unconventional magnetic properties, such as spin glasses [6]. Simulating these so-called quantum many-body systems on a classical device is extremely challenging due to the large amount of entanglement these systems feature. As previously seen, the most general state for two spins is described by superposition of all possible configuration. Therefore, for a system with N particles, an extensive amount of information, corresponding to 2^N numbers, is required to represent the state. This exponential scaling makes it impossible to calculate the behavior of strongly-correlated quantum systems using even the most advanced classical computers currently available.

In 1982, Richard Feynman came up with an intriguing idea to overcome this bottleneck. He proposed building synthetic quantum systems in the laboratory that could be arbitrarily controlled to mimic the behavior of the quantum many-body system of interest [7]. In these so-called *quantum simulators*, the implemented model is a simplified version of the real, complex quantum system, yet it retains the fundamental features. In order to study phenomena which are driven by the underlying quantum mechanical interactions, these synthetic quantum systems need to be well isolated from the environment. Quantum simulators further need to provide the capability to ”program” the models of interest to access various regimes. Establishing such an universal platform has the potential to uncover new insights and provides the means to investigate fundamental questions in quantum physics ranging from quantum magnetism [8] to quantum thermalization [9, 10] and beyond.

Over the past decades there have been enormous effort to isolate and manipulate individual quantum objects ranging from charge particles trapped in an electric field [11,12], neutral atoms that are cooled with laser light [13–15], and single photons in optical cavities [16], which has provided a starting point to the development of quantum simulation platforms [17, 18]. For instance, neutral atom in optical lattices can be used to study Hubbard models [19, 20], which serve as prototypical scenario for mimicking interacting electrons in a solid-state materials [21–24].

A paradigmatic example of a quantum many-body system, describing the mutual interactions between quantum spins, is the Heisenberg model [25, 26]. Formulated by Werner Heisenberg in the early 20th century, this model serves as a template for studying quantum magnetism [8]. Furthermore, spin models offer broad versatility, as general quantum mechanical two-level systems can be mapped on a spin-1/2 system. Various experimental platforms have started to implemented versions of the Heisenberg model, including trapped ions [27–30], ultracold molecules [31–35] and superconducting circuits [36–38].

In recent years, quantum simulators based on neutral atoms in highly excited electronic states, known as Rydberg states, experienced significant interest because they offer extraordinary properties for implementing quantum spin models [39–43]. In Rydberg atoms, one can easily induce large dipole moments. As a consequence, they exhibit strong dipolar interactions, exceeding the typical strength of external magnetic and electric noise. In addition, those interactions are large compared to the lifetime associated with the spontaneous and black body decay rates [44]. These properties are the primary resources for studying the dynamics of Rydberg atoms, which are purely driven by the interaction Hamiltonian in an isolated environment.

The Rydberg atom platform is extremely versatile. Experiments have begun to implement building blocks, enabling the control of certain Hamiltonian parameters of quantum spin models. By encoding the spin-1/2 degree of freedom to two internal atomic states, first implementations of XX [45–49], XXZ [50], and Ising models [51–57] have been realized and started studies on exciting phenomena ranging from quantum phase transitions [55] and topological phases [46] to magnetic ordering [51]. In addition to these abilities, approaches based on neutral atoms trapped in optical tweezer arrays allow for arbitrarily controlling the position degree of freedom of particles in the Hamiltonian in one, two, and three dimensions [58–60].

These achievements present a first step towards tunable quantum simulation and have facilitated initial explorations of quantum many-body systems with a few adjustable Hamiltonian parameters. Nevertheless, the field of quantum simulation is still in its early stages, lacking complete control over every implemented Hamiltonian parameter. A collective effort is focused on developing systems capable of realizing arbitrary interaction Hamiltonians in a programmable fashion and employing them to explore new regimes.

1.2 Thesis outline

This thesis is dedicated to advancing the Rydberg atom platform into a quantum simulator with tunable interaction parameters. We develop various novel techniques to shape the many-body interaction Hamiltonian of isolated quantum spin systems in a desired manner and we exploit these capabilities to study out-of-equilibrium dynamics of general XYZ quantum spin models. To our knowledge, many of the realized spin models had not been studied on Rydberg platforms before.

We begin with a didactic introduction about how atomic interactions naturally encode quantum spin-1/2 models in chapter 2. In this chapter, we also demonstrate the implementation of three distinct Heisenberg models through the proper selection of the principal quantum number. We employ this method to study out-of-equilibrium magnetization dynamics under different spatially disordered XX, XXZ, and Ising models in a single experimental setup. Our investigations reveal that the magnetization dynamics in these systems are universal in the sense that they collapse onto a single curve when rescaling time. We explain this behavior using an effective model that only considers pairs of spins. In chapter 3, we present how periodically applied drives can introduce new effective XYZ dipolar interactions that go beyond those naturally accessible. We extensively benchmark this technique in two scenarios: one involving an ordered atom array and another featuring a disordered atomic gas. We realize this by engineering coherent two-particle oscillations and freezing many-body dynamics. This method is employed to explore out-of-equilibrium relaxation dynamics in different regimes, consecutively breaking $SU(2)$ and $U(1)$ symmetries in the XYZ model. We further investigate the melting of domain wall states under XXZ Hamiltonians with tunable anisotropy. In chapter 4, we introduce a protocol that enables the realization of time-reversal in isolated quantum spin systems. This is realized by carefully selecting the spin-encoding states in the Rydberg manifold, effectively changing the sign of the interaction Hamiltonian. We employ this protocol and demonstrate how an initially magnetized state that has relaxed into a demagnetized state evolves back-in-time into a magnetized state. Combining this technique with the periodic driving of chapter 3, we realize the reversal for a wide range of spin models with tunable symmetry. Finally, in chapter 5, before concluding in chapter 6, we proposes two alternative methods for engineering many-body systems on the Rydberg platform. These include an approach to engineer a Hamiltonian that naturally occurs in nuclear magnetic resonance, enabling the application of sophisticated multi-pulse sequences. Finally, we propose a protocol that introduces mobile dopants into the Rydberg spin system by encoding the spin and hole degree of freedoms into three Rydberg states, enabling the study of doped quantum magnets.

CHAPTER 2

Universal relaxation behavior of tunable quantum spin systems

Parts of this chapter is based on the following manuscript, from which parts of the text have been taken verbatim:

Observation of universal relaxation dynamics in disordered quantum spin systems [a]

T. Franz*, S. Geier*, C. Hainaut, A. Braemer, N. Thaicharoen, M. Hornung, E. Braun, M. Gärttner, G. Zürn, M. Weidemüller

arXiv:2209.08080

---

[a] Parts from the earlier version of this manuscript also appear in the dissertation of Titus Franz [61]. While Titus Franz focuses on the aspect of the observed universality and its relation to prethermalization, this chapter explicitly focuses on the experimental implementation of the three quantum spin models. We further discuss an extended version of the pair model and introduce a new rescaling.

Quantum simulation, utilizing highly tunable synthetic systems, has emerged as a powerful tool for addressing unresolved problems in modern physics. Many platforms, such as neutral atoms [62–64], ultracold molecules [32, 33, 65, 66], trapped ions [28, 29, 67], and superconducting circuits [36, 68, 69], have reached a level of sophistication that allows for the exploration of prototypical quantum systems relevant to condensed matter physics. These models encompass Bose- and Fermi-Hubbard models, as well as Heisenberg spin-1/2 models. The strength of quantum simulation platforms lies in their ability to finely tune interactions as well as the geometric arrangement of particles with high precision.

Rydberg atoms have emerged as an exceptional platform for studying quantum spin-1/2 systems under precisely controlled conditions, enabling the fine-tuning of a wide range of experimental parameters [39–43]. The most important properties of Rydberg atoms are outlined in Appendix A. As described in Chap. 1, the Rydberg platform is capable of implementing XX [45–49], XXZ [50], and Ising models [51–57] by encoding the spin into two internal atomic states. Furthermore, ongoing technological advancements enable the manipulation of individual atoms and the arrangement of multiple atoms into desired spatial configurations, effectively control the positional degree of freedom in the Hamiltonian [43, 65]. These capabilities have been effectively employed to explore scientific and technological questions in the field of quantum simulation [43, 50, 55–57, 70, 71], quantum sensing [72–74] as well as quantum computing [40, 75–77].

In this context, our team on the Heidelberg Rydberg experiment has conducted quantum simulation experiments on quantum spin-1/2 systems represented by Rydberg atoms over the past years. Specifically, we explored the impact of spatial disorder on many-body out-of-equilibrium dynamics. In the course of these investigations, the group studied Rabi oscillations in a dipolar interacting XX model [70]. It was demonstrated that the relaxation of these oscillations was primary driven by interactions and was consistent with numerical simulations. Additionally, we discovered that the magnetization relaxation dynamics in a spatially disordered system with hundreds of quantum spins can be described by a stretched exponential function [78]. The observation that a complex system follows a simple stretched exponential law is a phenomenon often associated with the physics of spin glasses.

What is even more remarkable is that the stretching exponent, which characterizes the observed relaxation, remained independent of the degree of disorder, at least up to a certain degree.

This raised questions about the generality of this relaxation behavior and its relationship to the specific interaction Hamiltonian. This chapter addresses the above questions and is divided into two parts, organized as follows:

- **Section 2.1:** This first section serves as an instructive introduction to quantum spin systems involving Rydberg atoms. We begin by explaining the approach used to describe atomic interactions among Rydberg atoms. We discuss approximations that justify addressing these interactions using a multipole expansion. By considering states possessing opposite parity, we discuss how to isolate an atomic two-level system, which is crucial to represent spin-1/2 systems. We then introduce second-order van der Waals interactions and elaborate how to realize a two-level system with different types of interactions. Finally, we show how these atomic interactions mimic Heisenberg quantum spin models and introduce the tunability of the spin Hamiltonian with respect to the principal quantum number.
- **Section 2.2:** The second section expands upon the concepts introduced previously and experimentally explores the magnetization relaxation behavior for three different Hamiltonians, each tuned by the principal quantum number. We perform a comparative analysis of the relaxation curves for the XX, XXZ, and Ising models, revealing a universal behavior among them. Finally, we introduce an effective model that reproduces the experimental data and offers insight into the motivation behind the rescaling.

2.1 From atomic interactions to quantum spin models

In this first section, we provide a didactic introduction to the most important aspect of Rydberg atoms: strong Rydberg-Rydberg interactions and how these interactions are employed to implement quantum spin systems. An overview of other relevant properties of Rydberg atoms is provided in Appendix A. The first experimental evidence of Rydberg-Rydberg interactions dates back the observation of a line broadening in the Rydberg transitions in the early 19th [79, 80]. Since then, the field of Rydberg atoms has rapidly developed, with the exceedingly strong interactions becoming one of the key tools in quantum science [39, 43].

For a single atom in a given Rydberg state, the dipole moment is zero due to the dipole selection rules. However, the separation between the electron and the atomic core is, on average, up to four orders of magnitude larger for Rydberg states compared to ground states. Therefore, the electron is weakly bound, and significant dipole moments can be induced by mixing nearby Rydberg states. Moreover, the large polarizability enables the generation of a dipole moment even with minor disturbances, such as the presence of another Rydberg atom positioned at an average separation of a few micrometers. In general, Rydberg-Rydberg interactions can be extremely complicated and challenging to calculate. However, in certain regimes, these interactions can be represented by a comparatively simple Hamiltonian. Most experiments operate in a regime where the distance between the atoms is so large that the electron clouds do not overlap. For two atoms, the critical distance is typically characterized by the Le Roy radius [81, 82]:

$$R_{\mathrm{LR}} = 2\left(\sqrt{\langle n_1 l_1 j_1|\hat{r}^2|n_1 l_1 j_1\rangle} + \sqrt{\langle n_2 l_2 j_2|\hat{r}^2|n_2 l_2 j_2\rangle}\right) \quad , \tag{2.1}$$

with $|n_{1,2} l_{1,2} j_{1,2}\rangle$ being the specific Rydberg state under consideration. This value needs to be compared to the typical separation between Rydberg atoms in experiments. The distance between Rydberg atoms has a lower bound, denoted as r_b, which is determined by the Rydberg blockade induced by the laser excitation process (see Appendix A). This Rydberg blockade radius is approximately an order of magnitude larger than the Le Roy radius for the experiments presented in this manuscript: $R_{\mathrm{LR}} \ll r_b$. For instance, in the case of two atoms in the $|48S\rangle$ Rydberg state $R_{\mathrm{LR}} \approx 674$ nm, while the typical blockade radius is $r_b \approx 5\ \mu$m.

Working in this regime simplifies the calculation of Rydberg-Rydberg interactions significantly. One can think of the two Rydberg atoms as classical charge distributions, with their electrostatic interaction energy given by:

$$\hat{H}_{\text{int}} = \frac{e^2}{4\pi\epsilon_0}\left(\frac{1}{|r + r_e^2 - r_e^1|} + \frac{1}{|r|} - \frac{1}{|r - r_e^1|} - \frac{1}{|r + r_e^2|}\right) \quad . \tag{2.2}$$

Here, r denotes the distance between two atoms and $r_e^{1,2}$ distance of the electrons with respective atom body:

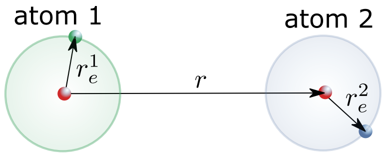

This energy can further be expanded in a multipole expansion [83–85]. For neutral atoms with no net charge, the leading-order term in this expansion is given by the dipole-dipole interaction Hamiltonian, which is introduced next.

2.1.1 Dipolar exchange interaction between Rydberg atoms

We consider a scenario in which neutral atoms are positioned at a distance r, orders of magnitude greater than the Le Roy radius. In leading order, this scenario can be described by dipole-dipole interactions. For ease of analysis, we focus on a scenario involving just two atoms. However, the result can directly be extended to systems with multiple atoms. In this setting, the dipole-dipole Hamiltonian is given by

$$\hat{H}_{\text{DDI}} = \frac{1}{4\pi\epsilon_0}\frac{\hat{\mathbf{d}}_1 \cdot \hat{\mathbf{d}}_2 - 3\left(\hat{\mathbf{d}}_1 \cdot \mathbf{e}_r\right)\left(\hat{\mathbf{d}}_2 \cdot \mathbf{e}_r\right)}{r^3} \quad . \tag{2.3}$$

Here, $\hat{\mathbf{d}}_i = e\hat{\mathbf{r}}_\mathbf{i} = (\hat{d}_i^x, \hat{d}_i^y, \hat{d}_i^z)$ is the dipole operator of atom i, $\mathbf{e}_r$ is the unit vector connecting two atoms, and r is their distance. This scenario is illustrated in Fig. 2.1 a) on the left panel. For convenience, we now change to a spherical basis and rewrite the expression for the dipole operator as well as for the unit vector. In doing so, the unit vector reads

$$\mathbf{e}_r = (\cos\phi \sin\theta, \sin\phi \sin\theta, \cos\theta) \tag{2.4}$$

while the dipole operators read

$$\hat{d}_i^0 = \hat{d}_i^z \tag{2.5}$$

$$\hat{d}_i^+ = -1/\sqrt{2}(\hat{d}_i^x + i\hat{d}_i^y) \tag{2.6}$$

$$\hat{d}_i^- = 1/\sqrt{2}(\hat{d}_i^x - i\hat{d}_i^y) \quad . \tag{2.7}$$

Here, we have chosen z as the direction of the magnetic field. Therefore, $\hat{d}_i^0$ conserves the total magnetic quantum number $M = m_j^{(1)} + m_j^{(2)}$, while $\hat{d}_i^\pm$ changes its value by $\Delta M = \pm 1$. We also denote θ as the angle between the atoms and the quantization. The dipole-dipole interaction Hamiltonian in the new basis is given by

$$\hat{H}_{\mathrm{DDI}} = \frac{1}{4\pi\epsilon_0}\left[\frac{1-3\cos^2\theta}{2r^3}\left(2\hat{d}_1^0\hat{d}_2^0 + \hat{d}_1^+\hat{d}_2^- + \hat{d}_1^-\hat{d}_2^+\right)\right. \tag{2.8}$$

$$-\frac{3\sin\theta\cos\theta}{\sqrt{2}r^3}\left((\hat{d}_1^+\hat{d}_2^0 + \hat{d}_1^0\hat{d}_2^+)e^{-i\phi} - (\hat{d}_1^0\hat{d}_2^- + \hat{d}_1^-\hat{d}_2^0)e^{i\phi}\right) \tag{2.9}$$

$$\left.-\frac{3\sin^2\theta}{2r^3}\left(\hat{d}_1^+\hat{d}_2^+e^{-2i\phi} + \hat{d}_1^-\hat{d}_2^-e^{2i\phi}\right)\right] \quad . \tag{2.10}$$

The resulting Hamiltonian possess three different terms. Each of these terms change the total magnetic quantum number M by $\Delta M = 0$ (2.8), $\Delta M = \pm 1$ (2.9) and $\Delta M = \pm 2$ (2.10), respectively. Phase factor $e^{\pm i\phi}$ and $e^{\pm 2i\phi}$ emerges as a consequence of the conservation of the total angular momentum.

Isolating an atomic two-level system We now consider the two-atom system in the pair state $|r_1 r_2\rangle \equiv |r_1\rangle \otimes |r_2\rangle$ within the Rydberg manifold. In the most general case, $\hat{H}_{\mathrm{DDI}}$ couples this system to other pair states involving various Rydberg states $|r_i r_j\rangle$. Here, we illustrate how one can reduce the interaction to resonant dipole-dipole interactions confined to a subspace spanned by $|r_1\rangle$ and $|r_2\rangle$, where $\{|r_1 r_1\rangle, |r_1 r_2\rangle, |r_2 r_1\rangle, |r_2 r_2\rangle\}$ are the relevant basis states. We will demonstrate this procedure using an example of two Rydberg states, $|r_1\rangle = |nS_{1/2}, m_j = 1/2\rangle$ and $|r_2\rangle = |nP_{3/2}, m_j = 1/2\rangle$, which are particularly relevant for the experiments in this thesis. The most important contribution for the interactions arises from coupling the initial pair state $|r_1 r_2\rangle$ with energy $E_{r_1 r_2}$ to pair states $|r_i r_j\rangle$ with energy $E_{r_i r_j}$.

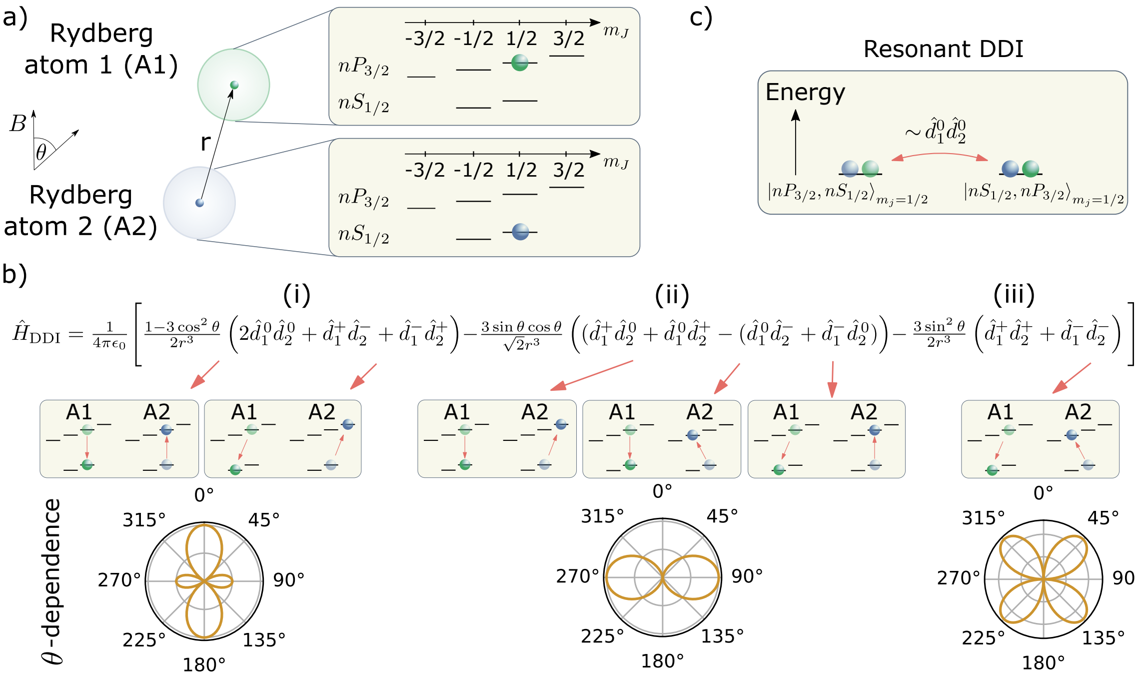

Figure 2.1: Dipole-dipole interactions induced processes. a) Left: Illustration of the system under consideration, consisting of two Rydberg atoms at distance r. Right: Atoms are initialized in states: atom 1 (A1) $|r_1\rangle = |nP_{3/2}, m_j = 1/2\rangle$ and atom 2 (A2) $|r_2\rangle = |nS_{1/2}, m_j = 1/2\rangle$. **b)** Illustration of the different processes induced by the dipole-dipole interactions. (i) Processes that do not change the total magnetic quantum number $\Delta M = 0$. (ii) Processes characterized by $\Delta M = \pm\, 1$. (iii) Processes characterized by $\Delta M = \pm\, 2$. Lower panels: angle dependencies of the various terms. **c)** Illustration of resonant dipole-dipole interactions with one remaining term.

The various possible processes induced by $\hat{H}_{\text{DDI}}$ on this two-atom pair state $|r_1 r_2\rangle$ are sketched in Fig. 2.1 b) (i) - (iii).

- **(i)** The first term (2.8) contains three distinct contributions. Each of these contributions involves coupling to pair states $|r_i r_j\rangle$ while conserving the total magnetic quantum number, such that $\Delta M = 0$. Typically, experiments apply a magnetic field to remove the degeneracy within the Zeeman sub-states. Consequently, only the interaction term $\hat{d}_1^0 \hat{d}_2^0$ is resonant as $E_{r_1 r_2} = E_{r_2 r_1}$ (see left panel in Fig. 2.1 b)). Other processes involve pair states that are detuned by $\Delta E = E_{r_1 r_2} - E_{r_i r_j}$. The resonant term results in an exchange between the Rydberg atomic states, featuring the characteristic angular dependence of $\propto 1 - 3\cos^2\theta$.

(ii) The second term (2.9) contains four distinct contributions, each coupling pair states that change the total magnetic quantum number by $\Delta M = \pm 1$. In the presence of a magnetic field, these processes become off-resonant and exhibit a detuning $\Delta E = E_{r_1 r_2} - E_{r_i r_j}$, which is tunable with the magnetic field. The angle dependence is characterized by $\propto \sin\theta\cos\theta$.

(iii) The third term (2.10) contains two distinct contributions, each coupling pair states that change the total magnetic quantum number by $\Delta M = \pm 2$. Similar to the scenario in (ii), these processes can be tuned out of resonance with a magnetic field. The angle dependence is characterized by $\propto \sin^2\theta$.

To implement a two-level system, we require that pair states outside the $|r_1\rangle$ and $|r_2\rangle$ subspace are detuned by an energy ΔE much larger than the typical interaction energies E_{int} that couple those pair states:

$$\Delta E \gg E_{\text{int}} \quad . \tag{2.11}$$

This is achieved by applying a magnetic field with a strength exceeding 30 G, resulting in a significant energy splitting of the different Zeeman sub-levels, which tunes undesired pair states out of resonance. With our magnetic field control, we are able to shift Zeeman sub-states by more than 100 MHz (see Appendix B), an order of magnitude larger than typical interaction strength.

So far, the discussion has been based on the particular example of $|r_1 r_2\rangle$. However, with the same reasoning, also the other pair states $|r_1 r_1\rangle$ and $|r_2 r_2\rangle$, in the two-level basis are energetically well isolated by this procedure. As a result, they are not significantly coupled to other pair states. In particular, $|r_1 r_1\rangle$ is typically detuned by several GHz from $|r_2 r_2\rangle$, even though it would have remained in the two-level system. Furthermore, the coupling of each pair state to itself is dipole forbidden. This situation allows us to treat the system as an isolated two-level system within the $|r_1\rangle$ and $|r_2\rangle$ subspace. Therefore, as illustrated in Fig. 2.1 c), we approximate systems of atoms including Rydberg $|r_1\rangle = |nS_{1/2}, m_j = 1/2\rangle$ and $|r_2\rangle = |nP_{3/2}, m_j = 1/2\rangle$ states by the resonant dipole-dipole interaction Hamiltonian $\hat{H}_{\mathrm{DDI}} = \frac{1}{4\pi\epsilon_0}\frac{1-3\cos^2\theta}{r^3}\,\hat{d}_1^0\hat{d}_2^0$.

The previous derivation is based on a specific choice of the magnetic quantum numbers: $|r_1\rangle \propto m_j = 1/2$ and $|r_2\rangle \propto m_j = 1/2$. For state combinations involving different m_j's, such as $|r_1\rangle \propto m_j = 1/2$ and $|r_2\rangle \propto m_j = -1/2$ ($|r_1\rangle \propto m_j = 1/2$ and $|r_2\rangle \propto m_j = 3/2$), the $\hat{d}_1^+\hat{d}_2^-$ ($\hat{d}_1^-\hat{d}_2^+$) terms provide a resonant interaction, considering the pair state energies. Therefore, for general Rydberg state combinations in the $|r_1\rangle = |nS_{1/2}\rangle$ and $|r_2\rangle = |nP_{3/2}\rangle$ manifold, the Hamiltonian reads:

$$\hat{H}_{\mathrm{DDI}} = \frac{1}{4\pi\epsilon_0}\frac{1-3\cos^2\theta}{r^3}\left(\hat{d}_1^0\hat{d}_2^0 + 1/2(\hat{d}_1^+\hat{d}_2^- + \hat{d}_1^-\hat{d}_2^+)\right) \tag{2.12}$$

$$= \begin{pmatrix} 0 & 0 & 0 & 0 \\ 0 & 0 & \frac{J}{2} & 0 \\ 0 & \frac{J}{2} & 0 & 0 \\ 0 & 0 & 0 & 0 \end{pmatrix} . \tag{2.13}$$

The second line expresses the Hamiltonian in the basis $\{|r_1r_1\rangle, |r_1r_2\rangle, |r_2r_1\rangle, |r_2r_2\rangle\}$ with $J = \frac{2C_3\,(1-3\cos^2\theta)}{r^3}$. The interaction coefficient reads

$$C_3 = \langle r_1r_2|\hat{d}_1^0\hat{d}_2^0 + 1/2(\hat{d}_1^+\hat{d}_2^- + \hat{d}_1^-\hat{d}_2^+)|r_2r_1\rangle /4\pi\epsilon_0 \quad . \tag{2.14}$$

We emphasize once again that only one of the above three terms is non-zero for a specific state combination.

Later in this chapter, we derive how Rydberg atoms in this interaction regime naturally implement Heisenberg XX spin models. The off-resonant terms become especially relevant when Rydberg atoms are prepared in states with the same parity. This scenario will be discussed in the next section.

2.1.2 van der Waals interaction between Rydberg atoms

In the previous section, we have seen how two atoms in opposite parity states, such as $|nS_{1/2}, m_j\rangle$ and $|nP_{3/2}, m_j\rangle$, realize specific regimes where pair states outside the two-level subspace are not significantly coupled, and the interactions are described by the resonant dipole-dipole Hamiltonian.

We now consider state combinations with the same parity, such as $|r_1\rangle = |nS_{1/2}, m_j\rangle$ and $|r_2\rangle = |n'S_{1/2}, m_j'\rangle$. As before, a magnetic field is employed to select a regime in which the pair states $\{|r_1r_1\rangle, |r_1r_2\rangle, |r_2r_1\rangle, |r_2r_2\rangle\}$ are energetically well isolated from pair states outside this subsystem. Therefore, we approximate this scenario once again as a two-level system. In this situation, direct dipole-dipole coupling between different pair states is forbidden by the selection rules. Instead, the leading-order process is of second order and proceeds through virtually excited intermediate pair states $\{|r_ir_j\rangle\}$ that are dipole-dipole coupled. These pair states are detuned by the so-called Förster defect $\Delta_F^{ij} = E_{r_\alpha, r_\beta} - E_{r_i, r_j}$, with $\alpha, \beta \in \{1, 2\}$, and are not physically populated.

In this regime, the Hamiltonian reads [86–88]:

$$\hat{H}_{\text{vdW}} = -\sum_{ij} \frac{\hat{H}_{\text{DDI}} |r_ir_j\rangle \langle r_ir_j| \hat{H}_{\text{DDI}}}{\Delta_F^{ij}} \sim \frac{1}{r^6} \,. \tag{2.15}$$

We now consider how this Hamiltonian couples the pair states within $\in \{|r_1r_1\rangle,$ $|r_1r_2\rangle, |r_2r_1\rangle, |r_2r_2\rangle\}$, which belong to the two-level system.

Exchange and van der Waals processes The van der Waals Hamiltonian in Eq. 2.15 induces two types of interactions, which we discuss using a specific example of $|r_1\rangle = |nS_{1/2}, m_j = 1/2\rangle = |nS\rangle$ and $|r_2\rangle = |(n+1)S_{1/2}, m_j = 1/2\rangle = |n+1S\rangle$. In general, many intermediate pair states $|r_ir_j\rangle$ contribute to the sum in Eq. 2.15. However, there are typically a few states with small Förster defects, dominating the interactions. The leading-order contribution of these processes is illustrated in Fig. 2.2.

(i) Exchange process: The first type of interaction is a coupling between different pair states (see (i) in Fig. 2.2). The most relevant coupling occurs between pair states $|nS, n+1S\rangle$ and $|n+1S, nS\rangle$, for which the main contributions come from virtually populated intermediate pair states in the nP manifold. Each sub-state in this manifold has a different Förster defect $\Delta_F(J, m_j)$, which can also be tuned by the applied magnetic field. Furthermore, the coupling through the intermediate state via dipole-dipole interactions involves different magnetic quantum numbers. Therefore, the various intermediate pair states in the sum of Eq. 2.15 contribute with different angle dependencies, as given by the dipole-dipole Hamiltonian in Eq. 2.8 - 2.10.

(ii) van der Waals process: The second type of interaction induced by $\hat{H}_{\mathrm{vdW}}$ includes coupling of each pair state to itself, as illustrated in Fig. 2.2 (ii). For each pair state, a different intermediate pair state provides the largest contribution. For example, $|nS, n+1S\rangle$ is coupled to itself through the intermediate nP manifold.

The above processes occur within the two-level system spanned by $|r_1\rangle$ and $|r_2\rangle$. Therefore, we express the interaction Hamiltonian for the two atoms in a matrix form using the pair state basis $\{|r_1r_1\rangle, |r_1r_2\rangle, |r_2r_1\rangle, |r_2r_2\rangle\}$:

$$\hat{H}_{\mathrm{vdW}} = \begin{pmatrix} E_{r_1r_1} & 0 & 0 & 0 \\ 0 & E_{r_1r_2} & \frac{J}{2} & 0 \\ 0 & \frac{J}{2} & E_{r_1r_2} & 0 \\ 0 & 0 & 0 & E_{r_2r_2} \end{pmatrix}, \tag{2.16}$$

with the matrix elements $E_{r_\alpha r_\beta} = \frac{C_6^{\|,\alpha\beta}(\theta)}{r^6} = \langle r_\alpha r_\beta|\hat{H}_{\mathrm{vdW}}|r_\alpha r_\beta\rangle$ and $J = \frac{C_6^{\perp,12}(\theta)}{r^6} = \langle r_1r_2|\hat{H}_{\mathrm{vdW}}|r_2r_1\rangle$. $C_6^{\|,\alpha\beta}$ and $C_6^{\perp,12}$ are the interaction coefficients.

In general, these coefficients are strongly influenced by the coupled intermediate state and might have different strengths, angle dependencies, and even signs. However, in many cases, there exist a few intermediate pair states with the smallest Förster defects that dominate the interactions, as previously seen. For state combinations where $|r_1\rangle$ and $|r_2\rangle$ are composed of nS and $(n+1)S$ states, the second-order processes are driven by the intermediate nP, $(n+1)P$ and $(n-1)P$ states. For Förster defects larger than the fine structure splitting, an evaluation of the sum in Eq. 2.15, results in isotropic interaction with only little angle dependence [89]. However, Förster defects of the individual fine structure states can be tuned with the magnetic field, resulting in a rich interaction Hamiltonian. This property and regime will be explicitly used in Chap. 5 to tune spin-1/2 Hamiltonian with mobile dopants.

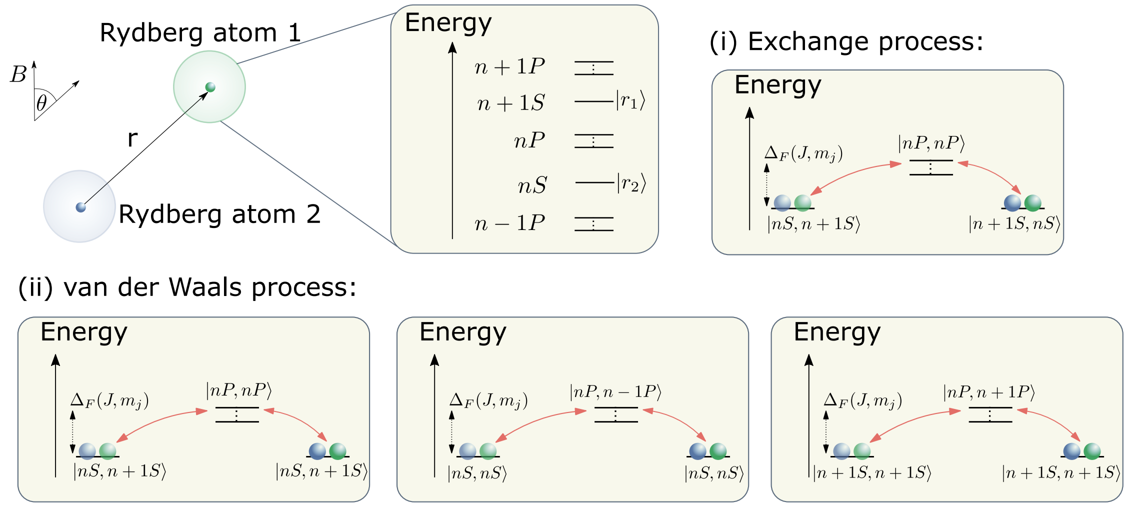

Figure 2.2: Van der Waals interactions induced processes. Left upper panel: Illustration of the two Rydberg atoms within the $|r_1\rangle = |(n+1)S\rangle$ and $|r_2\rangle = |nS\rangle$ subspace. (i) Second order exchange process through the intermediate $|nP\rangle$ state manifold, detuned by the Förster defect $\Delta_F(J,m_j)$. (ii) Van der Waals processes inducing an energy shift, by coupling each pair state to itself.

Limitations and Förster resonances The above description is valid as long as the virtually populated intermediate pair states are not resonantly coupled. However, for short distances, interactions are so strong that the intermediate pair states might be significantly coupled and populated. In this regime, the interactions transition from a $1/r^6$ scaling to resonant dipole-dipole interactions scaling as $1/r^3$. Furthermore, in some configurations, the Förster defect to the intermediate pair state approaches zero and the interactions scale as $1/r^3$, already for larger Rydberg atom separations. This configuration is called a Förster resonance [90]. These Förster resonances can also be tuned and realized using an external field [91]. However, as mentioned before, working at short distances or at small Förster defects significantly populates pair states outside a desired two-level system. Therefore, we avoid such a situation for the experiments presented in this thesis

2.1.3 Higher-order multipole terms

In the previous sections, we derived the interactions between Rydberg atoms based on the leading-order in the multipole expansion: the dipole-dipole interactions. To justify this treatment, we estimate the contribution of the next-order term of the multipole expansion, which is the quadrupole-quadrupole interaction.

The quadrupole-quadrupole interaction Hamiltonian scales as $\hat{H}_{\mathrm{QQI}} \propto \frac{e^2 \langle \hat{r}^2 \rangle^2}{r^5}$ [92]. Comparing this to the scaling behaviors of dipole-dipole interactions ($\hat{H}_{\mathrm{DDI}} \propto \frac{e^2 \langle \hat{r} \rangle^2}{r^3}$) and van der Waals interactions ($\hat{H}_{\mathrm{vdW}} \propto \frac{e^4 \langle \hat{r} \rangle^4}{\Delta_F \, r^6}$) as seen in Eq. 2.3 and 2.15, respectively, we can identify certain distances where $\hat{H}_{\mathrm{QQI}}$ dominates over both $\hat{H}_{\mathrm{DDI}}$ and $\hat{H}_{\mathrm{vdW}}$. For $\hat{H}_{\mathrm{DDI}}$, this occurs at a distance r_{DDI} below which $\hat{H}_{\mathrm{QQI}}$ dominates. This is the case for

$$\frac{e^2 \left\langle \hat{r}^2 \right\rangle^2}{r_{\mathrm{DDI}}^5} = \frac{e^2 \left\langle \hat{r} \right\rangle^2}{r_{\mathrm{DDI}}^3} \quad . \tag{2.17}$$

Here, the matrix elements are roughly equal, and $\langle \hat{r}^2 \rangle \approx \langle \hat{r} \rangle^2$. For the states considered in this thesis, quadrupole-quadrupole interactions typically dominate at distances $r_{\mathrm{DDI}} < 300$ nm, which is more than an order of magnitude smaller than the minimum distance imposed by the blockade radius in our setting. Thus, quadrupole-quadrupole interactions are negligible.

In the case of $\hat{H}_{\mathrm{vdW}}$, we expect a distance r_{vdW} above which $\hat{H}_{\mathrm{QQI}}$ dominates. This is the case for

$$\frac{e^2 \left\langle \hat{r}^2 \right\rangle^2}{r_{\mathrm{vdW}}^5} = \frac{e^4 \left\langle \hat{r} \right\rangle^4}{\Delta_F \, r_{\mathrm{vdW}}^6} \quad . \tag{2.18}$$

Therefore, $\hat{H}_{\text{QQI}}$ dominates at distances $r_{\text{vdW}} > \frac{e^2}{\Delta_F} \sim 350$ μm for usual Förster defects of 1 GHz. At those distances, interactions are already negligible small, and typical distances between atoms are on the order of tenths of μm. These estimations justify the treatment of Rydberg-Rydberg interaction using the leading-order multipole expansion.

2.1.4 Mapping Rydberg interactions to quantum spin models

In the previous two sections, we have introduced how the interactions between two Rydberg atoms can be described by a dipole-dipole and van der Waals Hamiltonian. By applying a properly selected magnetic field, we lift the degeneracy of the Zeeman sub-states and isolate an effective two-level system spanned by two Rydberg states: $|r_1\rangle = |nL_J, m_j\rangle$ and $|r_2\rangle = |n'L'_{J'}, m'_j\rangle$ within the Rydberg manifold. The Hamiltonian of this system has been expressed in the pair state basis: $\{|r_1r_1\rangle, |r_1r_2\rangle, |r_2r_1\rangle, |r_2r_2\rangle\}$.

These types of interactions can be mapped on a quantum XXZ Heisenberg spin-1/2 model with two spin states $|\downarrow\rangle$ and $|\uparrow\rangle$. The Hamiltonian is given by:

$$\hat{H}^{1,2}_{\text{XXZ}} = J^{\perp}(\hat{S}^1_x\hat{S}^2_x + \hat{S}^1_y\,\hat{S}^2_y) + J^{\parallel}\hat{S}^1_z\hat{S}^2_z + h_z(\hat{S}^1_z + \hat{S}^2_z) + V \quad , \tag{2.19}$$

with $\hat{S}^i_\alpha (\alpha \in x, y, z)$ are the spin-1/2 operator of spin i. $J^{\perp,\parallel}$ is the interaction energy between spin 1 and 2 and h_z a longitudinal field. The two terms, $J^{\perp}_{ij}$ and $J^{\parallel}_{ij}$ represent exchange and Ising interactions, respectively. Depending on their ratio, Heisenberg spin models exhibit distinct dynamics and have various properties. In a many-body system, the Ising case, where $J^{\perp} = 0$, features additional symmetries under local spin rotations $\hat{S}^i_z$ that commute with the Hamiltonian, making the Ising model integrable. However, for $J^{\perp} \neq 0$, $\hat{S}^i_z$ are no longer conserved and the Hamiltonian is non-integrable.

We now express the Hamiltonian in the pair state basis $\{|\downarrow\downarrow\rangle, |\downarrow\uparrow\rangle, |\uparrow\downarrow\rangle, |\uparrow\uparrow\rangle\}$:

$$\hat{H}^{1,2}_{\mathrm{XXZ}} = \begin{pmatrix} \frac{J^{\parallel}}{4} + h_z + V & 0 & 0 & 0 \\ 0 & -\frac{J^{\parallel}}{4} + V & \frac{J^{\perp}}{2} & 0 \\ 0 & \frac{J^{\perp}}{2} & -\frac{J^{\parallel}}{4} + V & 0 \\ 0 & 0 & 0 & \frac{J^{\parallel}}{4} - h_z + V \end{pmatrix} . \tag{2.20}$$

The Hamiltonian has exactly the same form as dipole-dipole and van der Waals interaction between two Rydberg atoms. We identify how the different terms map on the Rydberg properties by comparing the XXZ Hamiltonian in Eq. 2.20 with the dipole-dipole Hamiltonian in Eq. 2.13 and the van der Waals Hamiltonian in Eq. 2.16. By identifying the Rydberg state as the spin-1/2 degrees of freedom, $|r_1\rangle = |\downarrow\rangle$ and $|r_2\rangle = |\uparrow\rangle$, we obtain

$$\begin{aligned} J^{\parallel} &= E_{\downarrow\downarrow} + E_{\uparrow\uparrow} - 2E_{\downarrow\uparrow} \\ J^{\perp} &= 2 \cdot J \\ h_z &= \frac{E_{\uparrow\uparrow} - E_{\downarrow\downarrow}}{2} \\ V &= \frac{E_{\downarrow\downarrow} + E_{\uparrow\uparrow} + 2E_{\downarrow\uparrow}}{4} \end{aligned} \tag{2.21}$$

XX model Considering two Rydberg states with opposite parity, such as $|nS\rangle$ and $|nP\rangle$, the interactions are described by the dipole-dipole Hamiltonian, and we identified the exchange term as:

$$J^{\perp} = \frac{C_3^{\perp}(1 - 3\cos^2\theta)}{r^3} . \tag{2.22}$$

Furthermore, energy shifts are dipole forbidden, resulting in a vanishing Ising term $J^{\parallel} = 0$. Dynamics under these so-called XX Hamiltonians have been extensively studied under various conditions and geometrical arrangements [45–48, 71, 93, 94], and they will also play a major role in experiments presented in this manuscript.

XXZ model For states with the same parity, such as $|nS\rangle$ and $|n'S\rangle$, direct dipole interactions are forbidden and the leading-order is of the second order. As derived previously, these van der Waals interactions induce exchange and Ising terms of the form:

$$J^{\perp,\parallel} = C_6^{\perp,\parallel}/r_{ij}^6 \quad . \tag{2.23}$$

Hamiltonians with exchange and Ising terms are referred to as XXZ Heisenberg models. By carefully selecting the spin states, one suppresses either exchange or Ising and tune the spin model of interest, which has been employed to study relaxation dynamics in these systems [50].

Besides the above-mentioned spin models within the Rydberg manifold, Rydberg atoms coupled by van der Waals interactions are also capable of implementing Ising model by encoding the spin in a ground and a Rydberg state. While this approach is not employed in the present thesis, it has generally enabled, for example, the investigation of exotic phases and phase transitions [54, 55], and spin liquids [56].

2.1.5 Tuning Heisenberg Hamiltonians with the principal quantum number

In general, there are many parameters that shape the character of atomic interactions and, consequently, the implemented Heisenberg spin model. These parameters include electric and magnetic fields, as well as the spatial orientation of the atoms. Throughout this thesis, we will subsequently introduce how these parameters are used to engineer a desired Hamiltonian.

In this section, we introduce how the selected principal quantum number n affects the form of the Hamiltonian. An important aspect comes from the scaling of different Rydberg properties with n, which is summarized in Appendix A. The dipole-dipole interactions are expected to scale as n^4. Therefore, Rydberg atoms interact more strongly for larger principal quantum numbers. Despite the enhanced interaction strength, this system always maps onto an XX model with exchange interactions. Later in Chap. 4, we will introduce how static electric fields and properly selected Zeeman sub-states lead to richer dipolar interacting spin models.

The situation is different for van der Waals interactions. Typically, these interactions exhibit a scaling behavior of n^{11}, which becomes evident when considering the n^4 scaling of dipolar interactions along with the n^{-3} scaling of the Förster defect. However, the situation becomes more complicated due to the possibility of the Förster defect attaining a value of zero, which can lead to Förster resonances inducing direct dipolar exchange processes instead of pure second-order van der Waals interactions [78, 95].

Fig. 2.3 a) display the exchange interaction $J^{\perp}$, the Ising interaction $J^{\parallel}$, and the onside field h_z as a function of the principal quantum number for a spin encoding $|{\downarrow}\rangle = |nS\rangle$ and $|{\uparrow}\rangle = |(n+1)S\rangle$. Exchange and Ising interactions have roughly the same strength, while the onside field h_z is negligibly small. The lower panel shows the ratio between $J^{\parallel}/J^{\perp}$, denoted as anisotropy, ranging from ~ -2 to 0 in the selected range. This is due to the rather small Förster defect of the intermediate $|nP\rangle$ pair states, which mainly drives the exchange process (see Fig. 2.2). Around $n = 37$, the intermediate $|nP\rangle$ pair states become resonant, leading to divergent interactions and a breakdown of the applied perturbation theory. In this regime, the system cannot be considered as isolated spin-1/2 system. Furthermore, we observe that the interactions change their sign around this Förster resonance.

The freedom to select the specific Rydberg state combination allows encoding the spin in two states where the principal quantum number differs by more than one, such as $|{\downarrow}\rangle = |nS\rangle$ and $|{\uparrow}\rangle = |(n+3)S\rangle$ Rydberg states. The scaling of the interactions with n is depicted in Fig. 2.3 b). In this situation, the Ising interaction term $J^{\parallel}$ is orders of magnitude larger than the exchange interaction $J^{\perp}$ term, as well as the onside field h_z. This difference can be understood by considering that the intermediate $|(n+1)P\rangle$ manifold contributes most to the exchange interaction process. However, these states exhibit Förster defects that are an order of magnitude larger compared to the $|{\downarrow}\rangle = |nS\rangle$ and $|{\uparrow}\rangle = |(n+1)S\rangle$ spin-1/2 encoding, resulting in the suppression of exchange processes. As illustrated in the lower panel of Fig. 2.3 b), $J^{\parallel}/J^{\perp}$ takes a value between ~ -300 and -1000 in the selected range. Therefore,

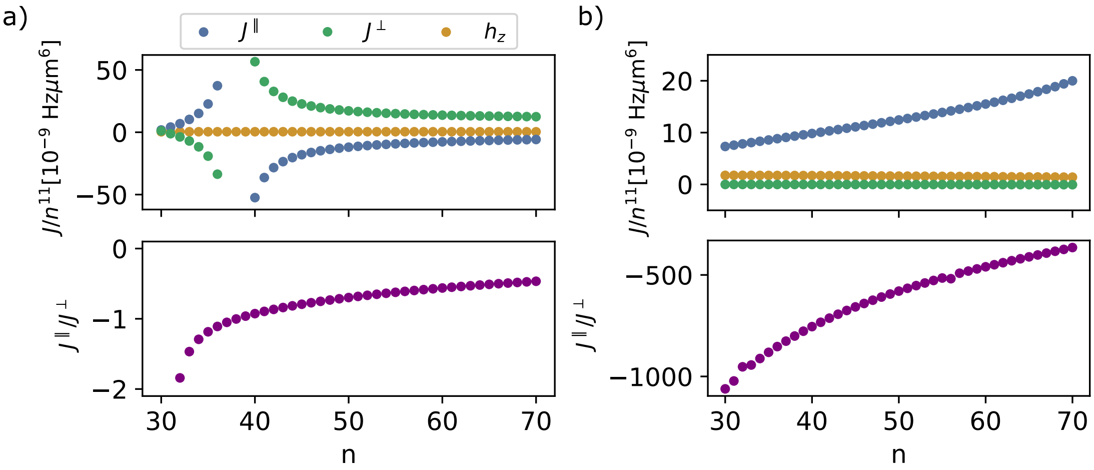

Figure 2.3: Scaling of XXZ interactions with the principal quantum number. a) Upper panel: $J^{\|}$,$J^{\perp}$ and h_z as a function of the principal quantum number for state combinations $|{\downarrow}\rangle = |nS\rangle$ and $|{\uparrow}\rangle = |(n+1)S\rangle$. Lower panel: Anisotropy $J^{\|}/J^{\perp}$ for the given states as a function of the principal quantum number. **b)** Same as a) but for state combinations $|{\downarrow}\rangle = |nS\rangle$ and $|{\uparrow}\rangle = |(n+3)S\rangle$.

this scenario can be approximated by an Ising model. In general, these types of spin models can also be implemented with $|P\rangle$ and $|D\rangle$ state combinations, leading to even richer spin models with possible angle dependence on the $C_6^{\perp,\|}$ interaction coefficients.

2.2 Observation of universal relaxation behavior for tunable spin models

In this section of the chapter, we apply the previously discussed freedom of implementing tunable Heisenberg spin-1/2 systems within the Rydberg manifold to study the relaxation behavior of different Hamiltonians. Understanding how microscopic details, such as Hamiltonian parameters or possible disorders, affect the dynamics of quantum many-body systems is an active field of research in modern physics and has been a focus of our experiments over the past years. In the following paragraph, we will explain the specific problem being addressed and how it relates to previous work performed within our group.

Motivation In general settings, the dynamics of isolated quantum systems far from equilibrium following a sudden change (referred to as a quench) exhibit diverse emergent phenomena. These phenomena include dynamical phase transitions [96, 97], quantum many-body scars [52, 77, 98] and many-body localization [99–103]. The behavior of these systems following a quench is heavily influenced by the nature of their interactions and the distribution of interaction strengths among the constituent particles [104]. A remarkable exception exists in systems with (metastable) prethermal phases, where relaxation dynamics exhibit universal character, decoupling from the specifics of the microscopic configuration [9, 105–109]. When exploring the impact of disorder on the dynamics of quantum many-body systems, a notable aspect is the potential for non-ergodic behavior [110]. This phenomenon is evident in scenarios like spin glasses, where relaxation becomes exceptionally slow [111], or in systems with many-body localization, causing dynamics to freeze entirely [112].

Our experiment naturally implements a quantum spin system with spatial disorder [50]. Previous investigations on our experimental setup have revealed interesting features, such as disorder-induced anomalously slow relaxation behavior of the system's magnetization following sub-exponential dynamics [78]. Interestingly, despite the non-integrability of the system and its many-body character, the sub-exponential dynamics follow a simple function: the stretched exponential law $e^{-(t/\tau)^{\beta}}$, where $1/\tau$ is the decay rate. Notably, the specific stretching exponent β characterizing this relaxation was found to be relatively independent of the details of the disorder distribution, up to a certain degree. Similar relaxation behavior has been found in other systems [113–116]. In summary, a wide range of classical and quantum systems, in the strong disorder regime, exhibit sub-exponential dynamics following the same functional pattern: the stretched exponential law.

Those observations raise the following question:

What is the origin of this shared behavior and how sensitive is it to modifications in the Hamiltonian's interaction parameters?

Previous work allowed us to obtain an analytic expression for stretched exponential relaxation in the quantum Ising model [117]. The availability of an analytic solution is due to the model's integrability, owing to its extensive number of conserved quantities. However, for non-integrable models, no analytic solutions exist. Numerically addressing this question is challenging due to the exponential expansion of the Hilbert space with system size in quantum many-body systems. To tackle this issue, we performed semiclassical simulations that disregard quantum effects beyond initial quantum fluctuations. These simulations indicated that non-integrable Heisenberg XYZ Hamiltonians exhibit out-of-equilibrium dynamics following a stretched exponential law, similar to the Ising model, independent of their symmetry [118].

In this part of the chapter, we address this question through analog quantum simulations using our Rydberg atom platform [1]. The platform is ideally suited for studying unitary dynamics because the time scales of the interacting dynamics vastly exceed those of the typical decoherence mechanisms. We experimentally implement Heisenberg XX, XXZ, and Ising models by carefully selecting states within

---

[1] To enhance the reader's understanding, our focus in this part is placed on the experimental results. A comprehensive introduction to the experimental setup, system preparation, readout, and strategies for controlling Rydberg spin is provided in Appendix B.

the Rydberg manifold and measure their magnetization relaxation dynamics from an initially fully magnetized state. Sec. 2.2.1 briefly outlines the experimental parameters used to implement the desired spin model and the relevant frequencies in the system. The measured relaxation behavior of the different Heisenberg models is presented in Sec. 2.2.2. Sec. 2.2.3 demonstrates the collapse of the various relaxation curves through rescaling time. We further analyze the observations by means of a simplified pair model in Sec. 2.2.4.

2.2.1 Experimental implementation of tunable quantum spin models

In Sec. 2.1, we introduced how interacting Rydberg atoms realize Heisenberg spin models. To recap, the Hamiltonian of interest, in its most general form, reads:

$$\hat{H}_{\mathrm{XXZ}} = \sum_{i<j} \left(J_{ij}^{\perp} (\hat{S}_x^i \hat{S}_x^j + \hat{S}_y^i \; \hat{S}_y^j) + J_{ij}^{\parallel} \hat{S}_z^i \hat{S}_z^j \right) \quad , \tag{2.24}$$

with the interaction coefficients given by $J_{ij}^{\parallel}$ and $J_{ij}^{\perp}$ given by Eq. 2.21. By encoding the spin into two Rydberg states $|nS\rangle$ and $|n'P\rangle$, we naturally implement the Heisenberg XX model as introduced in Sec. 2.1.4. In contrast, when encoding the spin in Rydberg states $|nS\rangle$ and $|n'S\rangle$, the second-order van der Waals interactions $\hat{H}_{\mathrm{vdW}}$ map to a Heisenberg XXZ model.

To explore the relaxation of the magnetization under various Hamiltonian, we exploit the dependence of the interactions on the principal quantum number n and select specific state combinations that map to XX, XXZ, and Ising Hamiltonian. In the following, we provide a brief introduction to how these state combinations are experimentally implemented and discuss the relevant frequencies in the system.

The XX Hamiltonian

Rydberg spin systems encoded in $|nS\rangle$ and $|n'P\rangle$ states realize the XX Hamiltonian with the exchange coefficient given by $J_{ij}^{\perp} = \frac{C_3^{\perp}(1-3\cos^2\theta_{\mathrm{ij}})}{r_{ij}^3}$ (see Fig. 2.4 a)). In this system, each pair state cannot be coupled to itself, resulting in a vanishing Ising term $J^{\parallel}_{ij} = 0$.

To experimentally realize this model, we have chosen the spin states $|{\downarrow}\rangle = |61S_{1/2}, m_j = 1/2\rangle$ and $|{\uparrow}\rangle = |61P_{3/2}, m_j = 1/2\rangle$. The transition frequency between these two states is $\nu/2\pi = 16$ GHz. To manipulate and read out the spin states in this two-level subsystem, we couple $|{\downarrow}\rangle \leftrightarrow |{\uparrow}\rangle$ with a resonant microwave field, effectively introducing an external field. Details on this driving can be found in Appendix B. The interaction coefficient for this spin system is given by $C_3^{\perp}/2\pi = 3.14$ GHzμm^3.

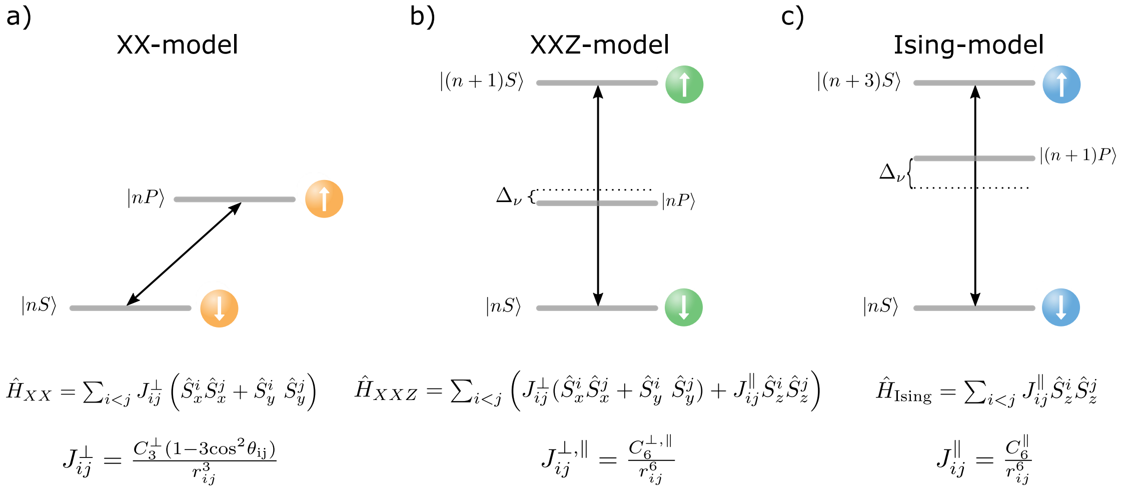

Figure 2.4: Illustration of Heisenberg spin models in the Rydberg manifold. a) Spin systems represented by Rydberg $|nS\rangle$ and $|nP\rangle$ states map onto an XX model with interaction that fall off as $1/r^3$. For Rydberg state combinations $|nS\rangle$ and $|(n+1)S\rangle$, the system maps onto an XXZ model (**b**), while Rydberg states $|nS\rangle$ and $|(n+3)S\rangle$ map onto an Ising Hamiltonian (**c**). For the latter two, the interactions are of van der Waals nature, falling off as $1/r^6$.

The XXZ Hamiltonian

To implement Heisenberg XXZ models, we encode the spin in two Rydberg states $|nS\rangle$ and $|(n+1)S\rangle$, whose principal quantum numbers differ by one, as illustrated in Fig. 2.4 b). In this configuration, the second-order interaction is described by the van der Waals interaction Hamiltonian, $\hat{H}_{\mathrm{vdW}}$, and the scaling of $J_{ij}^{\|} = C_6^{\|}/r_{ij}^6$ and $J_{ij}^{\perp} = C_6^{\perp}/r_{ij}^6$ is illustrated in Fig. 2.3 a). We obtain a significant exchange term because the Förster defect to the intermediate $\sim |nP, nP\rangle$ pair states is small.

Our experimental implementation of an XXZ Hamiltonian selects the spin states $|\downarrow\rangle = |61S_{1/2}, m_j = 1/2\rangle$ and $|\uparrow\rangle = |62S_{1/2}, m_j = 1/2\rangle$ in the Rydberg manifold. The Förster defects with the intermediate $|61P, 61P\rangle$ pair states are on the order of $\Delta_F \sim 300$ MHz. In the case of $n = 61$, both the Ising and exchange interactions terms are similar, resulting in an anisotropy given by $J^{\|}/J^{\perp} = -0.7$. With $\nu/2\pi = 32$ GHz, the transition frequency is approximately twice the frequency of the previous implementation of the XX model. The microwave manipulations in this spin system require two photons, as the transition is dipole forbidden. We drive the system with two identical microwave photons of frequency $\omega/2\pi = 16$ GHz, detuned by $\Delta_\nu/2\pi \sim 150$ MHz from the intermediate state $|nP\rangle$ state.

The Ising Hamiltonian

So far, experiments with cold Rydberg atoms have only implemented XX and XXZ Heisenberg model within the Rydberg manifold [45, 47, 48, 50, 71]. Ising models have been implemented and studied using ground-to-Rydberg state combinations [52, 55, 77]. As discussed in Sec. 2.1.5, by carefully selecting the principal quantum number, the exchange term in the XXZ Heisenberg model can be drastically suppressed, enabling the implementation of an effective Ising model within the Rydberg manifold. To achieve this, we select Rydberg states that differ by a factor of three in principal quantum number: $|nS\rangle$ and $|(n+3)S\rangle$. The exchange term is mainly driven by the intermediate $|(n+1)P\rangle$ states, which possess large Förster defects Δ_ν, and therefore, exchange interactions are suppressed by $1/\Delta_\nu$, according to Eq. 2.15 (see Fig. 2.4 c)).

To experimentally realize the Ising model, we select $|\downarrow\rangle = |61S_{1/2}, m_j = 1/2\rangle$ and $|\uparrow\rangle = |64S_{1/2}, m_j = 1/2\rangle$ as the spin states. Förster defects with the intermediate

$|62P, 62P\rangle$ pair states are on the order of $\Delta_F \sim 3000$ MHz, which is much larger than for the XXZ model implementation and suppresses the exchange term. In this case of $n = 61$, the exchange interaction term is orders of magnitude smaller than the Ising term, resulting in an anisotropy given by $J^{\parallel}/J^{\perp} = -400$ (see Fig. 2.3 b)). The transition frequency is $\nu/2\pi = 94$ GHz, and the two spin states are again coupled with two microwave photons.

We note that in our implementation of the different Heisenberg models, the $|{\downarrow}\rangle$ spin state is always represented by the $|61S_{1/2}, m_j = 1/2\rangle$ Rydberg state. The desired spin model is then simply realized by coupling to $|{\uparrow}\rangle = |61P_{3/2}, m_j = 1/2\rangle$ (XX model), $|{\uparrow}\rangle = |62S_{1/2}, m_j = 1/2\rangle$ (XXZ model), or $|{\uparrow}\rangle = |64S_{1/2}, m_j = 1/2\rangle$ with a microwave field.

2.2.2 Relaxation dynamics for different spin models

In this section, we explore the magnetization dynamics under the previously introduced XX, XXZ, and Ising Hamiltonian. The experimental setup and tools are elaborated in Appendix B. All experiments start with the excitation of the $|{\downarrow}\rangle = |61S_{1/2}, m_j = 1/2\rangle$ Rydberg state. The three different spin Hamiltonians are implemented by simply changing the microwave frequency and, therefore the addressed $|{\uparrow}\rangle$ Rydberg state. For all realizations, we fix the size of the ground state cloud (waists: $\sigma_x \approx 64\mu$m, $\sigma_{y,z} \approx 45\mu$m) and the size of the blue and red excitation lasers[2] (waists: $\sigma_{x,y}^{blue} \approx 55\mu$m, $\sigma_{x,y}^{red} \approx 1.5$ mm), and therefore, the geometrical setting. The excitation process in our cold gas results in a three-dimensional cloud of approximately N $\approx 80-250$ randomly distributed Rydberg atoms. Furthermore, the Rydberg blockade mechanism (see Appendix A) imposes a minimal distance of $r_b \approx 10$ μm between the spins. To study the magnetization relaxation behavior, we implement a Ramsey protocol as sketched in Fig. 2.5 a). We use our microwave drive to apply a $\pi/2$ pulse. After this initialization, the system is polarized along the x-direction in a Bloch sphere picture, and the state reads $|{\rightarrow}\rangle^{\otimes \mathrm{N}} = 1/\sqrt{2}(|{\uparrow}\rangle + |{\downarrow}\rangle)^{\otimes \mathrm{N}}$.

---

[2] Used for the two-photon excitation of Rydberg atoms described in Appendix B.

After an evolution time of up to 30 μs, we use a second $\pi/2$ pulse, combined with optical de-excitation and field ionization, to tomographically read out the x magnetization $\langle \hat{S}_x \rangle$ (see Appendix B).

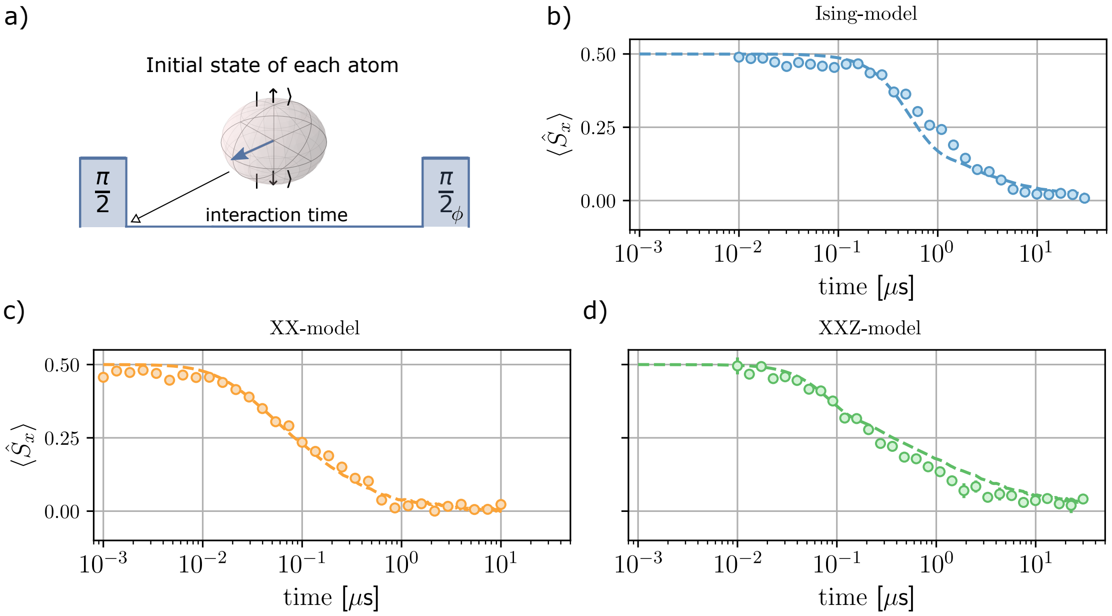

Figure 2.5: Magnetization relaxation dynamics under three distinct Hamiltonian. **a)** Sketch of the experimental Ramsey protocol to probe far-from-equilibrium dynamics. Magnetization dynamics as a function of time for the Ising model (**b)**), the XX-model (**c)**) and the XXZ-model (**d)**). The median interaction strength is $2\pi \cdot J^{\|}_{\text{median}} = 2.3$ MHz (Ising-model), $2\pi \cdot J^{\perp}_{\text{median}} = 21$ MHz (XX-model) and $2\pi \cdot J^{\perp}_{\text{median}} = 4.6$ MHz (XXZ-model with $J^{\|}/J^{\perp} = -0.7$). Dashed lines are DTWA simulations. Subfigures (b) - d)) and caption taken and adapted from [119].

The resulting magnetization relaxation dynamics are shown in Fig. 2.5 b) - d). For all spin models, we observe an initial plateau magnetization of $\langle \hat{S}_x \rangle = 0.5$ at early times. This is attributed to the Rydberg blockade, which enforces a minimal distance and thus a maximum interaction strength in the system. After the initial plateau, the magnetization starts to relax, with a common feature being relaxation towards zero magnetization at long times. For each model, the timescales of the relaxation are different, determined by the respective interaction strengths. The relaxation process takes more than an order of magnitude in time for all spin models.

To compare the relaxation curves to numerical predictions, we need the positions of the Rydberg spins. We use a hard-sphere model where each Rydberg excitation is described by a superatom [120] with a given blockade radius and effective Rabi frequency [50]. The time-evolution of the experiment is simulated using the Discrete Truncated Wigner Approximation (DTWA) [121] and shown by the dashed lines in Fig. 2.5 b) - d). The minor difference observed between simulations and experiments can primarily be attributed to inaccuracies in the atom distribution derived from the simplified excitation model.

In summary, we employ Rydberg atoms to implement three different quantum spin models with spatial disorder and measure the relaxation behavior in a single experimental setting by varying the microwave frequency to address different states. In the next section, we continue with a closer comparison of the dynamics.

2.2.3 Observation of a scaling behavior

The magnetization relaxation dynamics measured in Fig. 2.5 are driven by three distinct Hamiltonian and exhibit different timescales. Despite these differences, the dynamics look similar in the log-linear plot.

Even more remarkably, by rescaling the time-axis, we find a collapse of the three respective curves which is within their experimental error bars, as shown in Fig. 2.6. The rescaling factor corresponds to the typical timescale of each system

$$|J^{\perp}_{\text{median}} - J^{\parallel}_{\text{median}}| \quad . \tag{2.25}$$

Here, $J^{\perp,\parallel}_{\text{median}} = \text{median}_j \max_i |J^{\perp,\parallel}_{ij}|$ is the median of the nearest neighbor interaction strengths. The explicit motivation for selecting this rescaling is discussed in the following section. It arises from the typical oscillation frequency between a pair of spins under an XXZ Hamiltonian. Therefore, irrespective of the specific nature of the Hamiltonian involved in the dynamics, the scaling behavior exhibits universal relaxation. The collapse of the curves allows us to deduce the functional structure

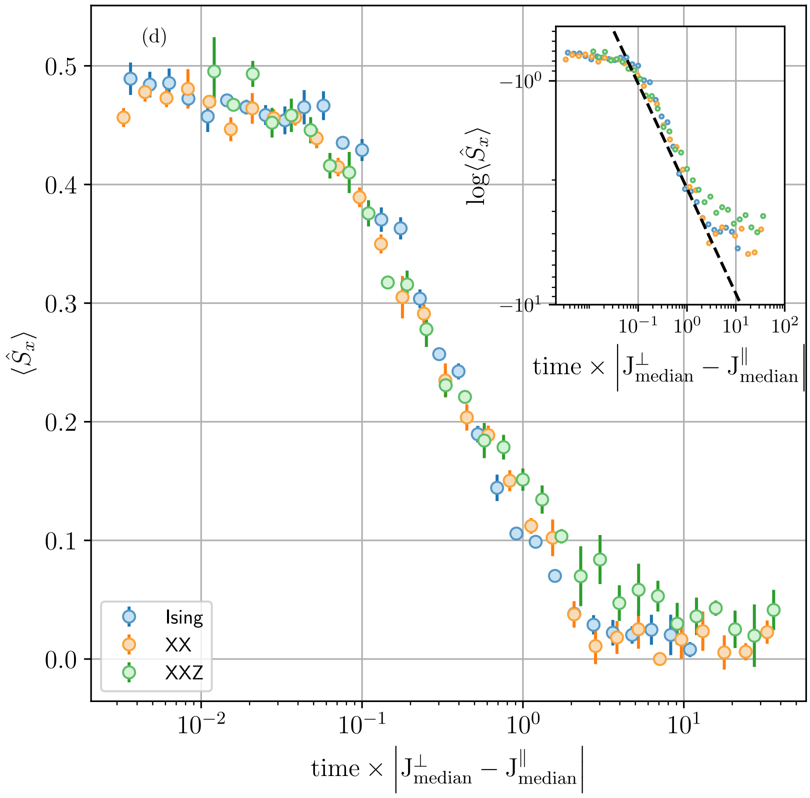

Figure 2.6: Scaling behavior. Magnetization dynamics as a function of the time, rescaled by the typical interaction strength $|J^{\perp}_{\text{median}} - J^{||}_{\text{median}}|$. The inset display the same data on a double logarithmic scale. The dashed line is guide for the eye with slope $m = 0.5$. Figure and caption taken and adapted from [119].

governing the relaxation dynamics in the non-integrable models. In the case of the Ising model, it is known that the relaxation follows a stretched exponential law $e^{-(t/\tau)^{\beta}}$ [117] with stretching exponent β and timescale τ. The logarithm of the stretched exponential law is a power-law. When plotted on a double logarithmic scale, this power-law becomes a linear function (dashed line in the inset of Fig. 2.6). In this representation, the rescaled experimental data also exhibits a linear behavior. This confirms the hypothesis that the stretched exponential law provides a unifying description of the relaxation for both the integrable quantum Ising model and the non-integrable XX and XXZ Hamiltonians in the strongly disordered regime. We note that the dynamics are only universal concerning the microscopic details of the system, such as the value of $J^{\|}/J^{\perp}$, whereas the macroscopic geometry and dimension of the cloud may lead to different dynamics [119].

2.2.4 Effective pair model description

To understand the origin of the apparent universality observed in the previous section, our aim is to construct a simplified model that accounts for the most relevant time scales of the system. To identify these time scales, we adopt an approach in the spirit of the strong disorder renormalization group (SDRG), where the strongest coupling is iteratively integrated out [122–125]. This approach is motivated by the distribution of interaction strength and therefore timescales in our spatially disordered spin system.

In our implementation, the strongest coupling occurs between two nearby spins, defining a pair. Afterward, the coupling between this pair and the rest of the system is treated perturbatively. To zeroth order, this pair of spins decouples from the system and evolves independently. This process of removing the most dominant coupling can be iteratively applied throughout the remaining part of the system. Considering our initial state along the x-direction, each individual pair coherently oscillates between the fully polarized state in plus and minus x-direction (see Fig. 2.7 a) left). The resulting magnetization oscillation, shown on the right, is independent of the specific XXZ Hamiltonian. The only difference is the frequency of this oscillation, which is determined by $|J_{ij}^{\perp} - J_{ij}^{\|}|$ and depends on the Ising and exchange interaction strengths. For two single spins, this oscillation is directly observed in Chap. 3. Therefore, this independence is at the origin of the observed universality of the relaxation dynamics.

To compare the zeroth-order approximation of independent pairs to the experimental setting, we compute the magnetization of each spin under the assumption that they only interact with one neighbor. The global magnetization is then the average over all of these pairs, which is explicitly written like:

$$\langle \hat{S}_x^{\text{indep. pairs}} \rangle (t) = \frac{1}{N} \sum_{\langle i,j \rangle} \cos(\frac{1}{2}(J_{ij}^{\perp} - J_{ij}^{\|})t). \tag{2.26}$$

Here, $\langle i, j \rangle$ denotes the summation over paired spins i and j. The results are shown as dashed-dotted lines in Fig. 2.7 b - d). Given the simplicity of this model, the agreement with the experimental data is remarkable for all three Hamiltonians. However, especially when applied to the Ising and XXZ models, this framework tends to underestimate the timescale of the dynamics. We can understand this behavior because the pair couplings obtained through iterative elimination generally turn out to be smaller on average than the nearest neighbor couplings.

The next order in this perturbative treatment includes effective Ising interactions between spin pairs and has been derived by Adrian Braemer [126]. The effective Hamiltonian of this process reads

$$\begin{aligned} \hat{H}_{eff} \approx & \sum_{\langle i,j \rangle} \left(J_{ij}^{\perp} (\hat{S}_x^i \hat{S}_x^j + \hat{S}_y^i \hat{S}_y^j) + J_{ij}^{\|} \hat{S}_z^i \hat{S}_z^j \right) . \\ & + \sum_{\langle i,j \rangle, \langle k,l \rangle} J_{ijkl}^{eff} \hat{S}_z^{(i)(j)} \hat{S}_z^{(k)(l)} \end{aligned} \tag{2.27}$$

$$J_{ijkl}^{eff} = \frac{J_{ik}^{\|} + J_{il}^{\|} + J_{jk}^{\|} + J_{jl}^{\|}}{2} \tag{2.28}$$

where $\langle i, j \rangle$ denotes the summation over paired spins i and j and $2\hat{S}_z^{(i)(j)} = \hat{S}_z^{(i)} + \hat{S}_z^{(j)}$. The analytical solution for the evolution of the magnetization in this integrable effective model is given by:

$$\langle \hat{S}_x^{\text{interact. pairs}} \rangle (t) = \frac{1}{N} \sum_{\langle i,j \rangle} \cos(\frac{1}{2}(J_{ij}^{\perp} - J_{ij}^{\|})t) \prod_{\langle k,l \rangle} \cos^2(\frac{1}{4} J_{ijkl}^{eff} t) \quad . \tag{2.29}$$

This effective Ising model of pairs captures the overall demagnetization dynamics for all observed times, yielding very similar results compared to dTWA, as can be seen in Fig. 2.7. From the analytical form of the time evolution, Eq. 2.29, we find that many different oscillation frequencies contribute to each spin's magnetization dynamics. However, most of these frequencies are very small and do not significantly contribute to the early-time dynamics. Consequently, a rational approach to achieve

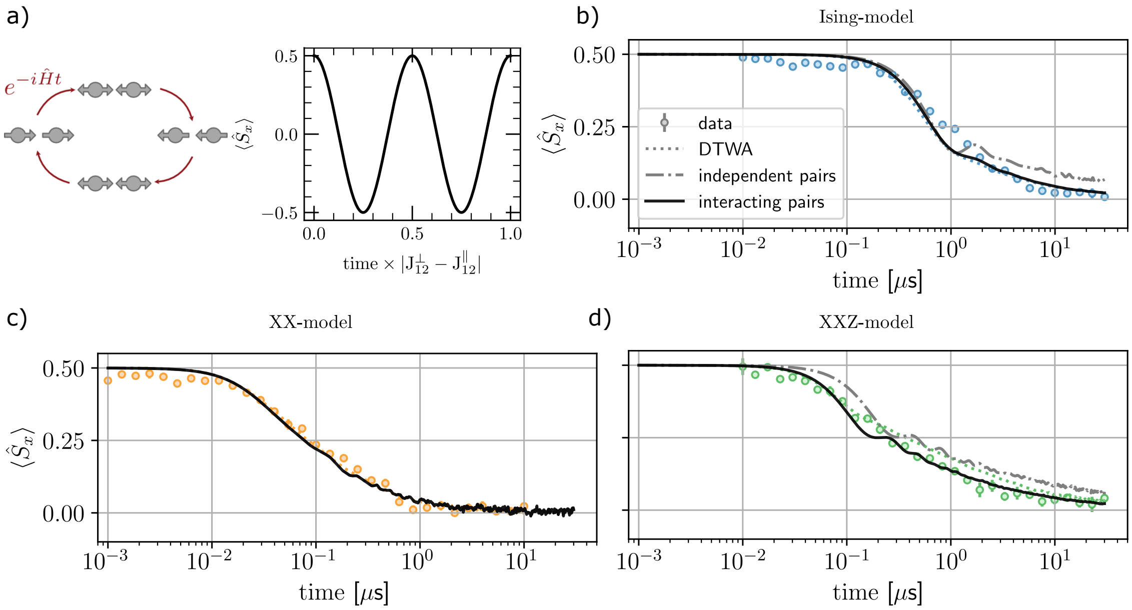

Figure 2.7: Effective pair model. a) Illustration of the oscillations of a single pair under XXZ Hamiltonian. Left: A fully polarized state, $|{\rightarrow}{\rightarrow}\rangle$ (left), evolves via the maximally entangled Bell state $1/\sqrt{2}\,(|{\rightarrow}{\rightarrow}\rangle + |{\leftarrow}{\leftarrow}\rangle)$ (top) to the state $|{\leftarrow}{\leftarrow}\rangle$ (right). Then, it returns to the origin via the other Bell state $1/\sqrt{2}\,(|{\rightarrow}{\rightarrow}\rangle - |{\leftarrow}{\leftarrow}\rangle)$ (bottom). Right: Oscillation of the magnetization for a single pair. **b)** - **d)** Comparison of the relaxation dynamics obtained by the pair approximation with/without effective Ising terms (solid black line/grey dash-dotted line) and with dTWA (dotted line) and the experimental data of Fig. 2.5 for Ising b), XX c) and XXZ model d). Figure and caption taken and adapted from [119].

a collapsed representation of the dynamics involves considering solely the fastest frequency for each spin. Given the highly disordered nature of our system, this dominant coupling will essentially always correspond to the closest neighboring spin. This accounts for the rescaling of experimental data with $\text{median}_i \max_j |J^{\perp}_{ij} - J^{\parallel}_{ij}|$.

The above scenario resembles a case of prethermalization, where a non-integrable many-body system can be effectively approximated by an integrable Hamiltonian for an extended duration before eventually reaching thermal equilibrium under the influence of the complete Hamiltonian. In our case, the integrable aspect is characterized by the pair Hamiltonian, which continues to govern the relaxation process for an extended period, even up to the point when the system becomes demagnetized. Our group, together with the theory collaborators Adrian Braemer and Martin Gärttner, is currently working on gaining a deeper understanding of this phenomenon and exploring the limitations of the pair model. However, it is important to note that this topic falls beyond the scope of the current thesis. First steps to investigate the applicability of the pair model were performed by Adrian Braemer and discussed in [119].

2.3 Summary and discussion

Summary

In this chapter, we have explored how Rydberg atoms model quantum Heisenberg spin systems in an analog fashion. We have introduced the principal quantum number as a parameter to shape the interaction Hamiltonian, enabling the experimental implementation of diverse Heisenberg models through this approach.

Part 1 In the first section, we elaborated on how interacting neutral atoms in two Rydberg states can be represented as a Heisenberg spin system. We started by considering two atoms placed at a distance such that the electronic clouds do not overlap. This justifies the application of a multipole expansion, with the first non-vanishing order being dipole-dipole interactions. In order to construct Heisenberg spin-1/2 models, it is essential to have a two-level system within the Rydberg manifold. The two-level system contains two Rydberg states that can be mapped to the two spin states, $|\downarrow\rangle$ and $|\uparrow\rangle$. We presented how a magnetic field isolates two Rydberg states and how dipole-dipole interactions effectively implement an XX model in this regime. Additionally, we considered two Rydberg states that are not coupled by direct dipole-dipole interactions. In this regime, second-order van der Waals interactions naturally establish XXZ models under specific circumstances, where pair states within the two-level system are energetically isolated. Finally, we introduced the principal quantum number as a parameter to shape the spin Hamiltonian and tune exchange and Ising interaction parameter.

Part 2 In the second section, we utilized the introduced tunability of the spin model to address unresolved problems that had arisen from earlier investigations on disordered spin systems conducted by our group. By implementing XX, XXZ, and Ising Hamiltonian, we explored how magnetization relaxation dynamics depend on these distinct types of Hamiltonian. Depending on the Hamiltonian used, the experimentally observed relaxation dynamics occurred on various timescales, which are well-described by a stretched exponential function. Despite the distinct nature of the three Hamiltonians, all relaxation curves collapsed when we rescale time using the typical timescale of the system. As rescaling factor, we selected the difference between the exchange and Ising term, motivated by the oscillation frequency of a pair of spins. We further motivated this choice by comparing the experimental data to an effective pair model, which accounts for the most relevant time scales in the system. At lowest order, this model leads to the formation of a non-interacting spin pair that reasonably describe the observed relaxation curves. When considering the first order, which includes interacting pairs, it matches both the experimental data and dTWA simulations for all times.

Discussion

The studies presented in this chapter demonstrate the capability of Rydberg-atom quantum simulators to synthesize a variety of many-body Hamiltonians on a single experimental setting. While XX and XXZ Heisenberg models have been previously realized through appropriate choices of Rydberg states, the realization of a pure Ising model within the Rydberg manifold has not been demonstrated before to our knowledge. Our implementation does not require any fine-tuning. It relies solely on altering microwave frequencies to address different Rydberg states for the spin encoding. In addition to the tunability of the interaction parameters, the interaction strength exhibits different scalings $\sim 1/r^3$ and $\sim 1/r^6$. This enables investigations on how different exponents α of the power-law interactions affect the dynamics in d dimensional systems.

Given its simplicity, the effective pair model reproduces the experimental relaxation curves remarkably well, suggesting that the emergence of spin pairs constitutes a unifying feature of disordered quantum spin systems. Therefore, further testing the validity of the pair model is subject to further studies. As our analysis is based on an investigation of the magnetization dynamics, future approaches would include measuring pair correlation functions. This requires access to local observable, a capability currently not available at our setup but in planning. Interestingly, recent studies in an disordered ultracold molecule experiment have measured correlations that align with a pair-based description [33]. Additionally, transport measurements including the melting of a domain wall state, as will be discussed in Chap. 3, could provide further information about the validity of the pair model. For excitations that are localized in spin pairs, the melting of such a domain wall state is expected to be suppressed. Furthermore, as the magnetization relaxation dynamics can be fully described by the effectively integrable pair model for times when the magnetization is already zero, it will be interesting to explore the question of a possible prethermal description [9, 105–109].

CHAPTER 3

Floquet Hamiltonian Engineering of isolated quantum spin systems

Parts of this chapter, are based on the following publication, from which parts of the text have been taken verbatim:

Floquet Hamiltonian Engineering of an Isolated Many-Body Spin System
S. Geier*, N. Thaicharoen*, C. Hainaut*, T. Franz, A. Salzinger, A. Tebben, D. Grimshandl, G. Zürn, M. Weidemüller
Science 374, 1149 (2021)

Parts of this chapter, are based on the following publication, from which parts of the text have been taken verbatim:

Microwave-engineering of programmable XXZ Hamiltonians in arrays of Rydberg atoms [a]

P. Scholl*, H.J. Williams*, G. Bornet*, F. Wallner, D. Barredo, T. Lahaye, A. Browaeys, L. Henriet, A. Signoles, C. Hainaut, T. Franz, S. Geier, A. Tebben, A. Salzinger, G. Zürn, M. Weidemüller

Phys. Rev. X Quantum 3, 020303 (2022)

---

[a] Parts of the this publication also appear in the dissertation of Pascal Scholl [127]. Pascal Scholl focuses on the aspect of the experimental implementation in the optical tweezer setup and provides a detailed discussion on the 1D domain-wall measurements. This chapter explicitly discusses the aspect of how to understand the effect of multi-pulse sequences on a spin system from few to many particles, contrasting the implementation in this ordered tweezer array scenario with the disordered atom gas scenario of the first publication [71].

Controlling the dynamics of strongly interacting closed many-body systems plays a crucial role in quantum science and technology applications, including the utilization of synthetic systems for the quantum simulation of complex many-body physics. As described in the previous chapter, experimental platforms based on Rydberg atoms can implement Heisenberg quantum spin models by encoding the spin-1/2 degree of freedom into two Rydberg states. In this approach, interaction parameters of the implemented Hamiltonian, arising from the natural Rydberg-Rydberg interactions between the atoms, are tunable by carefully selecting the principal quantum number.

Over the past decades, many experimental platforms, including trapped ions [28, 29, 67], neutral atoms [62–64], and cold molecules [32, 33, 65, 66], have demonstrated similar abilities to naturally implement prototypical many-body Hamiltonian in an analog fashion. Most notably, all these platforms have the ability to tune certain parameters of the implemented Hamiltonian, enabling the exploration of different regimes. However, in the pursuit of realizing fully programmable quantum simulators, the goal is to expand their capabilities to simulate arbitrary Hamiltonians, where additional parameters can be modified at will.

In this spirit, using time-periodic driving, a naturally given many-body Hamiltonian of a closed quantum system can be transformed into an effective target Hamiltonian that exhibits vastly different dynamics [128–130]. This so-called Floquet Hamiltonian Engineering was introduced in the context of nuclear magnetic resonance (NMR) and has become a powerful tool in quantum physics, enabling the exploration of dynamical phase transitions [131], Floquet Prethermalization [105, 106], unconventional phases of matter [132–135] and topological configurations [136–140].

The application of such Floquet engineering approaches, as introduced in works like [141, 142], to quantum systems that are well isolated from the environment and have the ability to control atoms on a single atom level, facilitates the quantum engineering of many-body spin systems. As discussed in Chap. 2 and in many other works [43, 50, 55–57, 70, 71], Rydberg atoms are well decoupled from the environment, enabling the exploration unitary quantum dynamics in various settings.

In this chapter, we develop methods to realize tunable quantum spin models through the application of Floquet Hamiltonian Engineering in Rydberg-atom experiments. We demonstrate the ability to implement new classes of XYZ models that go beyond those naturally realized by simply encoding the spin into two Rydberg states. This ability is combined with the single-atom control provided by an optical tweezer setup, demonstrating control over both the spatial positions of the atoms and the implemented model.

The Chapter is organized as follows:

- **Section 3.1:** This section introduces the general concept of Floquet Hamiltonian Engineering and the mathematical framework. Furthermore, we discuss how a periodic drive consisting of four global microwave pulses, realizes arbitrary XYZ Heisenberg Hamiltonians.

- **Section 3.2:** Here, we present experiments that demonstrate the experimental realization of Floquet Hamiltonian Engineering in a system consisting of a few atoms. By adjusting the delay between global microwave pulses, we directly observe the engineering of coherent oscillations for two particles. Furthermore, we study the freezing of magnetization relaxation dynamics in an ordered 2D configuration with 32 atoms.

- **Section 3.3:** In this section, we change the setting and investigate Floquet Hamiltonian Engineering in a 3D spatial disordered gas of Rydberg atoms. We perform similar experiments as those presented in the previous section and demonstrate the freezing of many-body relaxation dynamics. Furthermore, we characterize the current limitations of our engineering approach.
- **Section 3.4:** In the last section, we demonstrate the usage of Floquet Hamiltonian Engineering for quantum simulation experiments by consecutively reducing the symmetry of the XYZ Hamiltonian and exploring its effects on conservation laws. In addition, we demonstrate that engineered 1D chains can distinguish various regimes of spin transport in a domain-wall state.

3.1 Floquet engineering on quantum many-body systems of Rydberg atoms

This section introduces the conceptual and mathematical framework necessary to understand how a periodically driven system realizes new types of Hamiltonians with tunable parameters. Additionally, we introduce the specific multi-pulse sequence used to engineer the interactions.

3.1.1 Introduction to the general concept

To realize new types of Hamiltonians, we employ an idea dating back to 1883. Floquet's theorem [128] allows us to describe the stroboscopic dynamics of periodically driven quantum systems using an effective time-independent Hamiltonian. The parameters of this so-called Floquet Hamiltonian can be engineered by controlling the properties of the drive [129, 130].

Originally, this technique was used to dynamically decouple spins in nuclear magnetic resonance systems from certain terms in the Hamiltonian by effectively canceling them. A paradigmatic example of Floquet Hamiltonian Engineering involves a series of spin echo sequences [143, 144] applied to a system of spins embedded in an inhomogeneous environment, as encountered, for example, in nuclear magnetic resonance. The pulse sequence inverts the spins multiple times so that they finally return to their initial states, appearing to be effectively decoupled from the environment. In a Hamiltonian description, this corresponds to the emergence of a vanishing Hamiltonian, that is, the effective time-independent Hamiltonian over the spin echo sequence becomes zero. Although this type of sequence is suitable to decouple the dynamics of single spins, more sophisticated sequences have been used to decouple two-body interactions [145]. Employing these sequences allows for the elimination of interaction-induced line broadening in spectroscopy, facilitating the detection of minor shifts in transition lines caused by other chemical components within the sample.

Since those early applications, the field has rapidly developed, and periodic driving is now employed to not only cancel certain terms in a Hamiltonian but also to actively shape them in a desired way in various experimental platforms. This has, for example, been employed to investigate localization of mixed quantum states [146], dynamical phase transitions [131], Floquet Prethermalization [105, 106], unconventional phases of matter [132–135] and topological configurations [136–140].

The general procedure is illustrated in Fig. 3.1. A system with dynamics described some naturally given Hamiltonian $\hat{H}_{\text{Nat}}$ is exposed to a periodic drive $\hat{H}_{\text{drive}}(t)$, such that the system's evolution is governed by the Hamiltonian $\hat{H}(t) = \hat{H}_{\text{Nat}} + \hat{H}_{\text{drive}}(t)$. In general, $\hat{H}_{\text{Nat}}$ may contain multiple components, such as single-particle terms, two-body, or even few-body interaction terms. In our implementation, we consider quantum spin-1/2 models as described in the previous chapter. The drive is applied with an external field coupling the two spin states, and the system exhibits the property that $\hat{H}(t) = \hat{H}(t + T)$, with T being the period of the drive. In this scenario, the system's evolution over one driving period can be approximated by a new time-independent so-called Floquet Hamiltonian $\hat{H}_{\text{Floq}}$. The mathematical framework used to obtain an explicit expression for the Floquet Hamiltonian $\hat{H}_{\text{Floq}}$ will be introduced in the next section. We want to emphasize that the Floquet Hamiltonian provides an effective description of the system, allowing for the introduction of new interaction terms into the system by carefully selecting the applied drive. These interactions can sometimes be of a mathematical nature and may not even occur in natural systems.

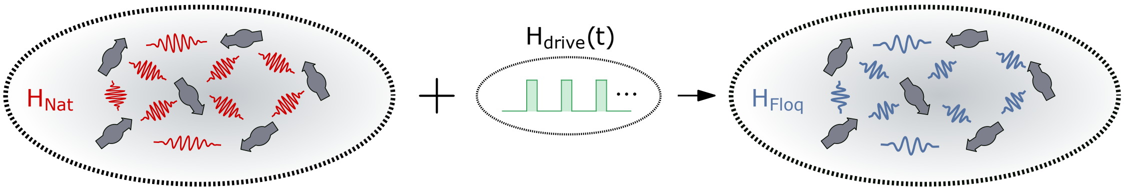

Figure 3.1: Concept of Floquet engineering. A system that naturally interacts with $\hat{H}_{\text{Nat}}$ (illustrated by the red connection lines between the spins) is exposed to a periodically applied drive that follows $\hat{H}_{\text{drive}}(t)$. Over one driving periodic, the system can be described by an effective time-independent Floquet Hamiltonian with tunable interactions, as illustrated by the blue connections line between the spins. Figure and caption taken and adapted from [71].

3.1.2 Average Hamiltonian Theory[1]

In order to obtain an expression for the time-independent target Floquet Hamiltonian, we employ the framework of Average Hamiltonian Theory (AHT) [147]. AHT is a powerful tool in quantum physics that provides a systemic approach to simplify and understand the dynamics of quantum systems under the influence of time-dependent driving. It is particularly valuable for periodically applied drives and helps to analyze and design multi-pulse sequences. In the subsequent paragraph, we will introduce this procedure and explain how to approximate the time-evolution

---

[1] Partially taken from [71] (Supplemental Material) and adapted for better readability

operator.

The dynamics of the density matrix for driven spin systems are described by the equation $\dot{\rho} = -i[\hat{H}(t), \rho]$. To analyze these dynamics in the interaction picture, we introduce the evolution operator $\hat{U}_{\text{drive}}(t) = \mathcal{T}\mathrm{exp}[-\mathrm{i}\int_0^{\mathrm{t}} \hat{\mathrm{H}}_{\mathrm{drive}}(\mathrm{t}')\mathrm{dt}']$, where $\mathcal{T}$ is the time ordering operator. This operator transforms the system into a rotated frame, characterized by the transformed density matrix $\tilde{\rho} = \hat{U}^{\dagger}_{\text{drive}}(t)\rho\hat{U}_{\text{drive}}(t)$, and the corresponding rotated-frame Hamiltonian $\tilde{\mathcal{H}}(t) = \hat{U}^{\dagger}_{\text{drive}}(t)\hat{H}_{\text{Nat}}\hat{U}_{\text{drive}}(t)$. In the case of periodically applied pulse sequences, the evolution operator $\hat{U}_{\text{drive}}(t)$ and, consequently, $\tilde{\hat{H}}(t)$ exhibit periodic behavior with a time period of t_c. To ensure that the system's dynamics in both frames (ρ and $\tilde{\rho}$) are identical during stroboscopic observations at integer multiples of the cycle time $t = nt_c$, we choose the evolution operator over one cycle to be the identity, i.e., $\hat{U}_{\text{drive}}(t_c) = 1$. Applying the Average Hamiltonian Theory, the system's evolution operator over a single cycle can be expressed as $\hat{U}(t_c) = \exp\left[-i\hat{H}_{\text{Floq}}t_c\right]$, where $\hat{H}_{\text{Floq}}$ represents the Floquet Hamiltonian (also known as Average Hamiltonian), and therefore, the systems seems to evolve under a time-independent Hamiltonian. To obtain $\hat{H}_{\text{Floq}}$, we employ a series expansion known as the Magnus expansion [148]. This expansion is represented as $\hat{H}_{\text{Floq}} = \hat{H}^{(0)} + \hat{H}^{(1)} + \ldots$, where $\hat{H}^{(n)}$ characterizes the Floquet Hamiltonian of the nth order. The first two orders are given by:

$$\begin{aligned} \hat{H}^{(0)} &= \frac{1}{t_c}\int_0^{t_c} \tilde{\hat{H}}(t')dt' \\ \hat{H}^{(1)} &= \frac{-i}{2t_c}\int_0^{t_c} dt' \int_0^{t'} dt[\tilde{\hat{H}}(t'), \tilde{\hat{H}}(t)]. \end{aligned} \tag{3.1}$$

The accuracy of the Floquet Hamiltonian depends on the chosen truncation order during the expansion. The elegance of this method arises from the inherent Hermitian nature of the Hamiltonian at every truncation level, providing a deeper understanding of the fundamental dynamics. For cycling times t_c that are significantly faster than the typical time scales of the system's Hamiltonian $\hat{H}_{\text{Nat}}$ (given by the interactions), the zeroth-order provides a reliable approximation for $\hat{H}_{\text{Floq}}$.

In other words, for any time t during the cycling interval $[0, t_c]$:

$$||\hat{H}(t)|| \cdot t_c \ll 1 \quad , \tag{3.2}$$

where $|| \cdot ||$ denotes the matrix norm. Additionally, in the case of a symmetric pulse sequence, all odd orders of the expansion (including $\hat{H}^{(1)}$) become zero (this is also the case for the pulse sequence introduced in the next section), and therefore, we focus on the zeroth-order contribution of the Floquet Hamiltonian.

3.1.3 Implementing Floquet engineering with Rydberg atoms

We now proceed with establishing the setting for the experiments presented in this chapter. Specifically, we will deduce the effective Floquet Hamiltonian for a Rydberg spin system subjected to periodic driving via a chosen multi-pulse sequence.

The system under consideration consists of quantum spin systems, represented by Rydberg: $|\downarrow\rangle = |nS\rangle$ and $|\uparrow\rangle = |nP\rangle$ states, as introduced in the previous chapter 2. This configuration allows us to realize a Heisenberg XX Hamiltonian, given by:

$$\hat{H}_{\mathrm{XX}} = \sum_{i,j} J_{ij} \left(\hat{S}_x^i \hat{S}_x^j + \hat{S}_y^i \hat{S}_y^j \right) \quad . \tag{3.3}$$

Here, $\hat{S}_\alpha^i$ ($\alpha \in x, y, z$) are spin-1/2 operators and $J_{ij} = 2\,C_3(\theta_{ij})/r_{ij}^3$ the interaction parameter, with the angle-dependent dipolar coupling parameter $2\,C_3(\theta_{ij})$ and r_{ij} the spatial separation between atom i and j. This Hamiltonian represents the natural interactions $\hat{H}_{\mathrm{Nat}} = \hat{H}_{\mathrm{XX}}$.

Furthermore, the drive is implemented using a microwave field that couples the two $|nS\rangle$ and $|nP\rangle$ spin states. We realize this by utilizing arbitrary waveform generation in combination with controlled radiation patterns and polarization, allowing us to apply any desired drive to the system. The microwave setup used in our experiment has been implemented during my master's studies and is summarized in my master thesis [149]. In addition, Appendix B provides an overview of the most important aspects and minor modifications implemented during the time of my PhD. The Hamiltonian describing the microwave drive between the $|\downarrow\rangle$ and $|\uparrow\rangle$

states reads:

$$\hat{H}_{\text{drive}}(t) = \sum_i \Omega(t) \left[\cos\phi(t)\hat{S}_x^i + \sin\phi(t)\hat{S}_y^i\right] \quad , \tag{3.4}$$

with $\Omega(t)$ the time-dependent Rabi frequency and $\phi(t)$ the phase. As illustrated in Fig. 3.2 a), we utilize $\hat{H}_{\text{drive}}(t)$ to apply the drive, which is composed of a periodic sequence of four global $\pi/2$ pulses, each realizing distinct spin operators $(\hat{S}_x, -\hat{S}_y, \hat{S}_y, -\hat{S}_x)$. The pulses are separated by delay times $\tau_1 = \tau(1 - 2v + 2w)$, $\tau_2 = \tau(1 + 2u - 2w)$ and $2\tau_3 = 2\tau(1 - 2u + 2v)$, where u, v, w are dimensionless parameters. Importantly, these parameters do not change the total cycling time t_c. Therefore, the exact system's evolution follows the Hamiltonian:

$$\hat{H}(t) = \hat{H}_{\text{XX}} + \hat{H}_{\text{drive}}(t) \quad . \tag{3.5}$$

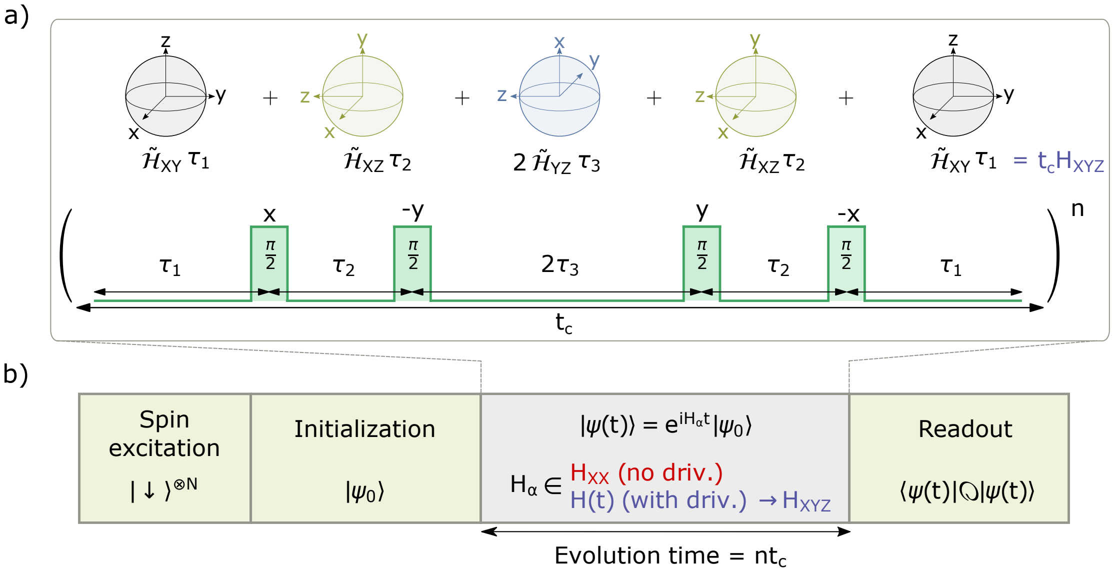

Figure 3.2: Experimental protocol and driving sequence. **a)** The periodic drive consists of n repetitions of four $\pi/2$ pulses in different directions (x, -y, y, -x) with adjustable delay time. The spheres indicate the spin-frame transformations, resulting in piece-wise constant rotated-frame Hamiltonians $\tilde{\mathcal{H}}_{\alpha\beta} = \sum_{i,j} J_{ij}/\hbar \left(\tilde{S}_\alpha^i \tilde{S}_\alpha^j + \tilde{S}_\beta^i \tilde{S}_\beta^j\right)$ below. **b)** Experimental protocol for measuring the system's magnetization. Figure and caption taken and adapted from [71].

This is the exact setting introduced in the previous section, and therefore, the associated Floquet Hamiltonian can be obtained by AHT. The effect of the ith pulse can be understood as a rotation of the spin frame. After the pulse, the system's evolution is governed by a rotated-frame Hamiltonian $\tilde{\mathcal{H}}$, which acts for a duration of τ_i, as illustrated in Fig. 3.2 a). Our implementation includes discrete microwave pulses with delay times in between, and the integral in the zeroth-order Floquet Hamiltonian of Eq. 3.1 reduces to a sum. Therefore, over one period t_c of the drive, the resulting zeroth-order Floquet Hamiltonian is the average of the rotated-frame Hamiltonians, weighted by the respective delay times: $\hat{H}_{\text{Floq}} = \frac{1}{t_c}\sum_{i=1}^{5}\tilde{\mathcal{H}}_i\tau_i$. We note that an explicit calculation of the Floquet Hamiltonian is included at the end of this section. This calculation especially provides intuition on the effect of the $\pi/2$ pulses on the Hamiltonian. The zeroth-order Floquet Hamiltonian originating from this drive can be expressed as:

$$\hat{H}_{\text{XYZ}} = \sum_{i,j} J_{ij}^{x}\hat{S}_x^i\hat{S}_x^j + J_{ij}^{y}\hat{S}_y^i\hat{S}_y^j + J_{ij}^{z}\hat{S}_z^i\hat{S}_z^j \quad , \tag{3.6}$$

with

$$J_{ij}^{x} = \frac{2J_{ij}}{3}\delta_x \tag{3.7}$$

$$J_{ij}^{y} = \frac{2J_{ij}}{3}\delta_y \tag{3.8}$$

$$J_{ij}^{z} = \frac{2J_{ij}}{3}\delta_z \tag{3.9}$$

The parameters $\delta_x = 1 - v + u$, $\delta_y = 1 + w - u$, and $\delta_z = 1 - w + v$ can be easily controlled by adjusting the time separation between the pulses. Therefore, the natural XX interactions of the Rydberg system have been transformed into an effective XYZ form, which is tunable without changing the experimental setup.

The effective description using the zeroth-order Floquet Hamiltonian is valid as long the drive, characterized by the cycling time t_c, is much faster than the typical energy scales of the system, which, in our case, are determined by the interaction strengths J_{ij}. According to AHT, this condition can be expressed as:

$$J_{ij} \cdot t_c \ll 2\pi \quad . \tag{3.10}$$

Fig. 3.2 b) illustrates the experimental protocol employed in this chapter. Following the Rydberg excitation, the atoms are prepared in the desired spin configurations. The subsequent system's evolution can be described by either the natural XX Hamiltonian or the specifically engineered XYZ Hamiltonian. After the evolution, we proceed to measure an observable $\mathcal{O}$.

We note that while we introduced this driving technique in the context of Rydberg atoms, the protocol is applicable to any two-level system that has the capability of applying $\pi/2$ pulses.

Explicit derivation of the Floquet XYZ Hamiltonian[2]

In the following paragraph, we conduct a thorough analysis of our pulse sequence, providing a clear understanding of the process behind constructing the Floquet Hamiltonian. With this understanding, one can gain valuable insights into the impact of the $\pi/2$ pulses, which, in turn, aids in the development of customized engineering sequences. As previously described, our pulse sequence includes four $\pi/2$ pulses with different phases ϕ $(0, 3\pi/2, \pi/2, \pi)$, corresponding to rotations around different axes $(\hat{S}_x, -\hat{S}_y, \hat{S}_y, -\hat{S}_x)$, and respective delay times τ_1, τ_2 and $2\tau_3$. The zeroth-order Floquet Hamiltonian is the average of the rotated-frame Hamiltonians, weighted by the respective delay times: $\hat{H}_{\text{Floq}} = \frac{1}{t_c} \sum_{i=1}^{5} \tilde{\mathcal{H}}_i \tau_i$.

For simplicity, we now consider a specific scenario involving two spins interacting with an XX Hamiltonian, given by $\hat{H}_{\text{XX}} = J\left(\hat{S}_x^1 \hat{S}_x^2 + \hat{S}_y^1 \hat{S}_y^2\right)$. Before the first $\pi/2$ pulse, when both the rotated-frame and lab-frame coincide, we obtain a component $\tilde{\hat{H}}_1 \tau_1/t_c = J(\tilde{\hat{S}}_x^1 \tilde{\hat{S}}_x^2 + \tilde{\hat{S}}_y^1 \tilde{\hat{S}}_y^2)\tau_1/t_c$. The first $\pi/2$ pulse, applied in x-direction, transforms the spin frame (as depicted by the spheres in Fig. 3.2 a)), rotating $\hat{S}_y \rightarrow U_{\pi/2_x}^{\dagger} \hat{S}_y U_{\pi/2_x} = \tilde{\hat{S}}_z$, while leaving $\hat{S}_x$ unaffected. Consequently, we acquire a second component $\tilde{\hat{H}}_2 \tau_2/t_c = J(\tilde{\hat{S}}_x^1 \tilde{\hat{S}}_x^2 + \tilde{\hat{S}}_z^1 \tilde{\hat{S}}_z^2)\tau_2/t_c$ during the second evolution interval τ_2. Repetition of this transformation throughout the sequence enables us to compute the contributions summarized in Table 3.1, yielding the Floquet Hamilto-

---

[2] Taken from [71] and slightly adapted for better readability.

nian for two-particle systems:

$$\hat{H}_{\text{Floq}} = \frac{1}{2(\tau_1+\tau_2+\tau_3)} J \left[2(\tau_1+\tau_2)\tilde{\hat{S}}^1_x\tilde{\hat{S}}^2_x + 2(\tau_1+\tau_3)\tilde{\hat{S}}^1_y\tilde{\hat{S}}^2_y + 2(\tau_2+\tau_3)\tilde{\hat{S}}^1_z\tilde{\hat{S}}^2_z \right]. \tag{3.11}$$

$\hat{H}_{\text{XX}}/J$	τ_1	$\pi/2_x$	τ_2	$\pi/2_{-y}$	$2\tau_3$	$\pi/2_y$	τ_2	$\pi/2_x$	τ_1
$\hat{S}^1_x\hat{S}^2_x$	$\tilde{\hat{S}}^1_x\tilde{\hat{S}}^2_x$	$\rightarrow$	$\tilde{\hat{S}}^1_x\tilde{\hat{S}}^2_x$	$\rightarrow$	$\tilde{\hat{S}}^1_y\tilde{\hat{S}}^2_y$	$\rightarrow$	$\tilde{\hat{S}}^1_x\tilde{\hat{S}}^2_x$	$\rightarrow$	$\tilde{\hat{S}}^1_x\tilde{\hat{S}}^2_x$
$+$									
$\hat{S}^1_y\hat{S}^2_y$	$\tilde{\hat{S}}^1_y\tilde{\hat{S}}^2_y$	$\rightarrow$	$\tilde{\hat{S}}^1_z\tilde{\hat{S}}^2_z$	$\rightarrow$	$\tilde{\hat{S}}^1_z\tilde{\hat{S}}^2_z$	$\rightarrow$	$\tilde{\hat{S}}^1_z\tilde{\hat{S}}^2_z$	$\rightarrow$	$\tilde{\hat{S}}^1_y\tilde{\hat{S}}^2_y$

Table 3.1: Effect of the $\pi/2$ pulses on a two-particle Hamiltonian. The first column displays the natural XX Hamiltonian with its two components. The following columns (two lower lines) display how these components get rotated under the spin frame transformation by the four $\pi/2$ pulses.

As the Floquet Hamiltonian only captures the stroboscopic dynamics of the system after each period of the drive, where the lab- and the rotated-frame are the same, we can omit the $\tilde{\cdot}$ symbol.

The above calculation can directly be extended to more particles, and therefore, the original XX Hamiltonian of our Rydberg system gets transformed into a Floquet Hamiltonian given by:

$$\hat{H}_{\text{Floq}} = \frac{1}{2(\tau_1+\tau_2+\tau_3)} \sum_{i,j} J_{ij} \left[2(\tau_1+\tau_2)\hat{S}^i_x\hat{S}^j_x + 2(\tau_1+\tau_3)\hat{S}^i_y\hat{S}^j_y + 2(\tau_2+\tau_3)\hat{S}^i_z\hat{S}^j_z \right]. \tag{3.12}$$

Our choice of $\tau_1 = \tau(1-2v+2w)$, $\tau_2 = \tau(1+2u-2w)$, and $\tau_3 = \tau(1-2u+2v)$ allows us to tune u, v and w without changing the cycling time $t_c = 2\cdot(\tau_1+\tau_2+\tau_3) = 6\tau$. Furthermore, this results in the XYZ Hamiltonian (Eq. 3.6) from above.

3.2 Floquet Hamiltonian Engineering in an array of a few atoms

The proposed protocol offers the capability to manipulate the interaction Hamiltonian of a many-body quantum spin system, introducing new terms that were originally not present. In the subsequent sections of this chapter, we explore the experimental implementation of this engineering protocol. The first step involves validating the engineering process, ensuring the faithful implementation of the target Hamiltonian, and assessing its performance. To achieve this, we employ various methods to confirm that the system indeed follows the dynamics expected from the Floquet Hamiltonian, and subsequently introduce them. As discussed previously, periodically driven systems can be effectively characterized using the concept of an effective Floquet Hamiltonian. Therefore, the manipulation of the system becomes directly observable through the coherent interactions among the constituent atoms.

We start our investigations in systems consisting of a few atoms, allowing us to directly witness these coherent dynamics. To establish an initial benchmark for the protocol, we commence by demonstrating its application for the iconic scenario involving two atoms. Subsequently, we extend our exploration to a larger ensemble with 32 atoms, as we investigate the influence of the engineering process on the dynamics within a 2D array of Rydberg atoms.

The work outlined in this section represents a collaborative effort between our team at Heidelberg and Prof. Antoine Browaeys' group at the Institut d'Optique in Palaiseau, France. The experiments were conducted by Prof. Browaeys' team using their experimental platform consisting of atoms trapped in optical tweezers. The conceptual ideas for the experiments involved extensive discussion with our team at Heidelberg, as well as the discussion of the results. Many of these ideas are motivated by our previous work on Floquet engineering, which will be discussed in the next section. We also performed additional analysis related to the engineering protocol, which is not covered in the primary reference for this section [48].

A comprehensive overview of the experimental setup at the group of Antoine Browaeys can be found in [127]. Their approach is based on tightly focusing laser beams to a size on the order of a micrometer. These so-called optical tweezers have the capability to capture individual atoms and arrange them in diverse spatial patterns. The concept of tweezer arrays, originally pioneered by Philippe Grangier [150], has evolved into one of the most powerful platforms for conducting quantum simulations and computations today [43, 55, 75–77]. To understand the experiments presented in this chapter, we briefly introduce the most relevant aspects of the experimental procedure: Initially, the atoms are loaded into optical tweezers and brought to their ground state. Subsequently, the optical tweezer traps are turned off, and a stimulated Raman adiabatic passage (STIRAP) is employed to prepare the Rydberg state $|nS\rangle = |{\downarrow}\rangle$. A magnetic field is utilized to split the Zeeman states, while a microwave field couples to an $|nP\rangle = |{\uparrow}\rangle$ state, realizing an XX model. The ability to locally address selected atoms with a strong 1013 nm laser allows for locally shifting their resonance such that they are not resonant with the global microwave field anymore. This procedure allows for the initialization of chosen product spin states. The readout is performed state-selectively by transferring the $|{\downarrow}\rangle$ atoms back to the ground state, where they are recaptured and optically detected through fluorescence imaging. To compare the experiments to numerical simulations, state-preparation-and-measurement (SPAM) errors are included. A detailed analysis of the different error sources in the experiment can be found in the dissertation of Pascal Scholl [127].

This section focuses on the engineering of an XXZ Hamiltonian. For convenience, we explicitly rewrite the previously derived XYZ Hamiltonian of Eq. 3.6 by choosing $J^x_{ij} = J^y_{ij} \neq J^z_{ij}$:

$$\hat{H}_{\text{XXZ}} = \sum_{i,j} J^x_{ij} \left(\hat{S}^i_x \hat{S}^j_x + \hat{S}^i_y \hat{S}^j_y \right) + J^z_{ij} \hat{S}^i_z \hat{S}^j_z \quad , \tag{3.13}$$

The anisotropy is given by $J^z_{ij}/J^x_{ij} = \delta_z/\delta_x$. The nearest-neighbor interaction energies of the Floquet XXZ Hamiltonian, J_x and J_z, are related to nearest-neighbor interaction energy J of the natural XX Hamiltonian as follows: $J_x(\delta_z/\delta_x) = \frac{2J}{2+\delta_z/\delta_x}$

and $J_z(\delta_z/\delta_x) = \frac{2J\delta_z/\delta_x}{2+\delta_z/\delta_x}$.

3.2.1 Tuning coherent oscillations between two atoms

Floquet Hamiltonian Engineering is shaping the underlying interaction Hamiltonian of quantum spin systems. To benchmark the engineering of the tunable XXZ Hamiltonian, we first explore the iconic case of two atoms. The spin-1/2 system is represented by the $|\downarrow\rangle = |90S_{1/2}, m_j = 1/2\rangle$ and $|\uparrow\rangle = |90P_{3/2}, m_j = 3/2\rangle$ Rydberg states. We drive the system with a Rabi frequency of $\Omega/2\pi = 7.2$ MHz, and the atoms are separated by 30 μm, resulting in an interaction strength of $J/2\pi =$ 930 kHz within the natural XX Hamiltonian.

In the case of two spins, the eigenstates and corresponding energies of $\hat{H}_{\mathrm{XXZ}}$ can be explicitly determined and are presented in the following table:

Eigenstates of $\hat{H}_{\mathrm{XXZ}}$	Energy
$\|\downarrow\downarrow\rangle$	J_z
$\|\uparrow\uparrow\rangle$	J_z
$\|+\rangle = (\|\uparrow\downarrow\rangle + \|\downarrow\uparrow\rangle)/\sqrt{2}$	$-J_z + 2J_x$
$\|-\rangle = (\|\uparrow\downarrow\rangle - \|\downarrow\uparrow\rangle)/\sqrt{2}$	$-J_z - 2J_x$

Table 3.2: Eigenstates and energies of a two atoms interacting under an XXZ Hamiltonian.

Static implementation: Generally, the engineering sequence can be applied over the full evolution time (static) or over a selected time window (dynamically). We investigate the static implementation by preparing the atoms in the equatorial plane of a Bloch sphere representation by applying a $\pi/2$ pulse. The resulting state reads $|{\rightarrow}{\rightarrow}\rangle_y = 1/2\left(|\uparrow\uparrow\rangle - |\downarrow\downarrow\rangle + i\sqrt{2}\,|+\rangle\right)$ (illustrated by the Bloch spheres in Fig. 3.3 a)). Taking into account the relevant eigenstates, the time evolution under an XXZ Hamiltonian is governed by:

$$|{\rightarrow}{\rightarrow}\rangle_y(t) = 1/2(|{\uparrow\uparrow}\rangle - |{\downarrow\downarrow}\rangle + e^{-i(2J_x - 2J_z)t} \cdot i\sqrt{2}\,|+\rangle) \quad . \tag{3.14}$$

The total magnetization of this state is predicted to undergo oscillations, transitioning from the $+y$ to the $-y$-direction, with frequency $2|J_x - J_z|$. In the experiment, we apply the engineering sequence with a single cycle ($n = 1$) for different cycle durations t_c, aiming to realize XXZ Hamiltonians with anisotropy ratios of $\delta_z/\delta_x = 1.33$ and $\delta_z/\delta_x = 1.8$. Fig. 3.3 a) displays the system's total magnetization, where we directly observe the coherent magnetization oscillations. Notably, the red data points, corresponding to an anisotropy of $\delta_z/\delta_x = 1.33$, exhibit slower oscillations compared to the green data points, which represent $\delta_z/\delta_x = 1.8$. This is expected since the strengths of exchange and Ising interactions are more balanced for $\delta_z/\delta_x = 1.33$, as indicated by Eq. 3.14.

Dynamical implementation: Two-atom oscillations can also be dynamically engineered for more general initial states. To demonstrate this in the case of two atoms, the ability of locally addressing the spins is used to initialize them in the $|{\uparrow\downarrow}\rangle$ state (illustrated by the Bloch spheres in Fig. 3.3 b)). We subsequently allow the system to undergo natural evolution governed by the XX Hamiltonian for a duration of 0.8 μs and measure the probability $P_{\uparrow\downarrow}$ associated with finding the atoms in the $|{\uparrow\downarrow}\rangle$ state. As anticipated based on the XX Hamiltonian, the two atoms exhibit oscillations between the states $|{\uparrow\downarrow}\rangle$ and $|{\downarrow\uparrow}\rangle$, with a frequency of $2J$ (see Fig. 3.3 b)). Following the 0.8 μs of natural evolution, the pulse sequence is activated for a duration of 0.9 μs with an XXX Hamiltonian ($J_x = J_z$ in Eq. 3.13) as the target. The signature is a reduction of the oscillation frequency by a factor 0.65(2), which is in agreement with the expected factor of 2/3. After switching off the drive, the atoms continue with the $2J$ oscillation. Remarkably, the engineering of the system does not cause any significant decoherence beyond what occurs naturally during free evolution. Exact simulations[3] of $\hat{H}_{\text{XXZ}}$ are shown as a green line in Fig. 3.3 include preparation and

---

[3] These simulations were performed by the team of A. Browaeys

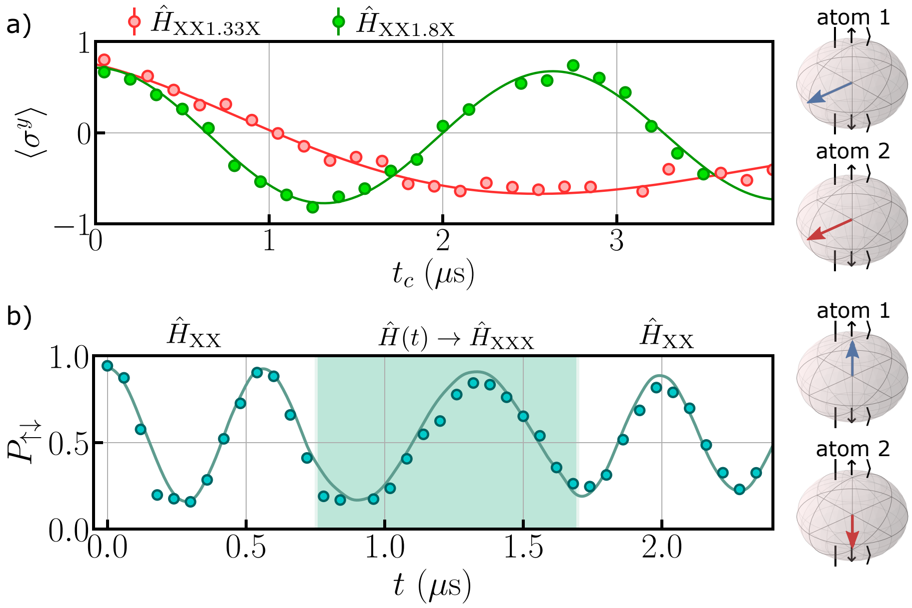

Figure 3.3: Floquet Hamiltonian Engineering with two atoms. a) Evolution of the y magnetization as a function of t_c for drives targeting XXZ Hamiltonian with anisotropy $\delta_z/\delta_x = 1.33$ (red points) and 1.8 (green points). The initial state is $|{\rightarrow\rightarrow}\rangle_y$, and the solid line displays a sinusoidal fit. **b)** Evolution of the probability $P_{\uparrow\downarrow}$ as a function of time. During the white area under the natural $\hat{H}_{\mathrm{XX}}$ and during the green shaded area under $\hat{H}(t)$ targeting $\hat{H}_{\mathrm{XXX}}$. The solid line is a simulation using the exact Hamiltonians. The Bloch spheres illustrate the initial state for atom 1 (blue) and atom 2 (red) for the respective experiments. Figure and caption taken and adapted from [48].

detection errors as well as fluctuations in the interatomic distance [48].

In summary, the use of Floquet Hamiltonian engineering provides an efficient tool for shaping the coherent oscillation dynamics in a system consisting of two atoms.

The engineering protocol in the lab-frame

We note that the effect of the engineering sequence on two atoms can also be understood by considering the transformation of the state in the lab-frame instead of the Hamiltonian in the rotating frame. In this paragraph, we derive the effect of the four $\pi/2$ pulses on the two-atom state, which provides some intuition about how the dynamics of Hamiltonians are mimicked by periodic driving [31, 71]. We consider our two atoms prepared in $|{\rightarrow\rightarrow}\rangle = 1/2\left(|{\uparrow\uparrow}\rangle + |{\downarrow\downarrow}\rangle + \sqrt{2}\,|+\rangle\right)$. Under the natural XX interaction ($J_z = 0$), the energies in Table 3.2 are zero for $|{\uparrow\uparrow}\rangle$ and $|{\downarrow\downarrow}\rangle$ and $\pm 2J_x$ for $|\pm\rangle$. To simplify the following calculations, we furthermore define the states $|\alpha_\pm\rangle = |{\uparrow\uparrow}\rangle \pm |{\downarrow\downarrow}\rangle$ such that the initial state can be expressed as:

$$|{\rightarrow\rightarrow}\rangle = 1/2\left(|\alpha_+\rangle + \sqrt{2}\,|+\rangle\right) \quad . \tag{3.15}$$

In the following, we present the effect of the four-pulse sequence on this state.

- **During τ_1:** In the first evolution stage, $|+\rangle$ picks up a phase of $2J_x\tau_1$, while $|\alpha_+\rangle$ does not, according to the energies. After this stage, the state reads $|\psi\rangle = 1/2\left(|\alpha_+\rangle + e^{-i2J_x\tau_1}\cdot\sqrt{2}\,|+\rangle\right)$.

- **$\pi/2_x$ pulse and evolution during τ_2:** A $\pi/2$ pulse along the x-direction results in swap of the states, such that $|\alpha_+\rangle \rightarrow \sqrt{2}\,|+\rangle$ and $\sqrt{2}\,|+\rangle \rightarrow |\alpha_+\rangle$. The state before the second free evolution stage reads $|\psi\rangle = 1/2\left(\sqrt{2}\,|+\rangle + e^{-i2J_x\tau_1}\cdot|\alpha_+\rangle\right)$. Because of the swap, $|\alpha_+\rangle$ effectively acquires a phase which is not present under XX interactions. During the following free evolution time τ_2, $|+\rangle$ again accumulates a phase such that $|\psi\rangle = 1/2\left(e^{-i2J_x\tau_2}\cdot\sqrt{2}\,|+\rangle + e^{-i2J_x\tau_1}\cdot|\alpha_+\rangle\right)$ at the end of this stage.

- **$\pi/2_{-y}$ pulse and evolution during τ_3:** A $\pi/2$ pulse along the $-y$-direction does not change $|\alpha_+\rangle$ but transforms $\sqrt{2}\,|+\rangle \rightarrow |\alpha_-\rangle$. Therefore, the state reads $|\psi\rangle = 1/2\left(e^{-i2J_x\tau_2}\cdot|\alpha_-\rangle + e^{-i2J_x\tau_1}\cdot|\alpha_+\rangle\right)$, which does not accumulate a phase during τ_3.

- **$\pi/2_y$ pulse and evolution during τ_2:** Now we rotate back around the $+y$-direction and undo the transfer. Therefore, after the evolution time τ_2, the state reads $|\psi\rangle = 1/2\left(e^{-i4J_x\tau_2}\cdot\sqrt{2}\,|+\rangle + e^{-i2J_x\tau_1}\cdot|\alpha_+\rangle\right)$

- **$\pi/2_{-x}$ pulse and evolution during τ_1:** The $\pi/2$ pulse around the $-x$-direction swaps the states again back and after the final evolution time τ_2, the state at the end of the sequence reads:

$$|\psi\rangle_{\text{final sequence}} = 1/2\left(e^{-i4J_x\tau_2}\cdot|\alpha_+\rangle + e^{-i4J_x\tau_1}\cdot\sqrt{2}\,|+\rangle\right) \quad . \tag{3.16}$$

We compare this result to the evolution of the two-atom states under an XXZ Hamiltonian

$$|\psi\rangle_{\text{direct XXZ}} = 1/2\left(e^{-i(-J_z)t}\cdot|\alpha_+\rangle + e^{-i(-J_z+2J_x)t}\cdot\sqrt{2}\,|+\rangle\right) \quad . \tag{3.17}$$

Therefore, by properly choosing τ_1 and τ_2, one can imprint phases that an XXZ Hamiltonian would have imprinted. We note that the case for two spins is extremely simplified and does not directly translate into a many-body state with different eigenstates.

3.2.2 Freezing many-body dynamics in a 2D atom array

The previous paragraph demonstrated engineering for the case of two atoms. Now, we consider a scenario with an increased system size of 32 atoms arranged in a 2D spatial configuration, as illustrated in the inset of Fig. 3.4. The first question that arises is how to verify whether our drive implements the Floquet Hamiltonian of Eq. 3.13 in this many-body regime where coherent oscillations are no longer observable due to the beating of many frequencies? One of the most drastic effects is a potential freezing of dynamics, considering the strongly interacting nature of the many-body system.

To demonstrate this, in a first series of experiments we have chosen the control parameters $u = v = w$ such that the timing of the delay times is equal $\tau_1 = \tau_2 = \tau_3$. This choice is equivalent to the famous Waugh-Huber-Haeberlen (WAHUHA) sequence [145], which is used to archive dynamical decoupling and suppress spin-spin interactions in NMR by engineering a zeroth-order Floquet Hamiltonian ($\hat{H}_{\text{Floq}} = 0$). Considering our implementation in an isolated system of Rydberg spins, this sequence implies $\delta_x = \delta_y = \delta_z$ in Eq. 3.6. Therefore, this particular sequence engineers a symmetric Floquet Hamiltonian $\hat{H}_{\text{Floq}} = \hat{H}_{\text{XXX}}$. In the previous section, we implemented this Hamiltonian to demonstrate a change in the oscillation frequency of the $|\uparrow\downarrow\rangle$ state (see Fig. 3.3). Despite the change in the oscillation frequency, the

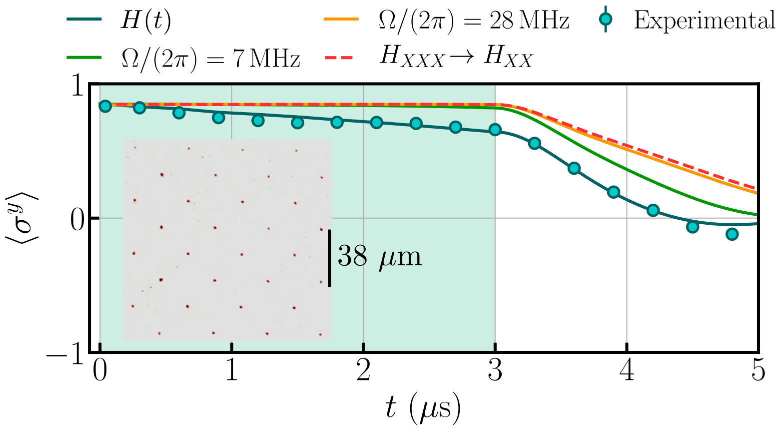

Figure 3.4: Freezing of magnetization in a 2D array. The time evolution of the y magnetization under $\hat{H}(t)$ targeting $\hat{H}_{\mathrm{XXX}}$ (shaded green area for 3 μs) and the natural $\hat{H}_{\mathrm{XX}}$ (white area) after initialization in $|\rightarrow \cdots \rightarrow\rangle_y$. Circles represent the experimental data points, while solid lines show MACE simulations that include SPAM errors: blue, $\hat{H}(t)$ with microwave imperfections; green, without microwave imperfections; orange, no microwave imperfections and an increased Rabi frequency of $\Omega/2\pi = 28$ MHz; dashed red line, exact $\hat{H}_{\mathrm{XXX}}$ followed by $\hat{H}_{\mathrm{XX}}$. Inset: Fluorescence image of the 32-atom array. The atom distance is $a = 27$ μm, resulting in a nearest-neighbor energy of $J/2\pi \approx 133$ kHz and a mean interaction energy of $J_m/2\pi \approx 720$ kHz. Figure and caption taken and adapted from [48].

XXX Hamiltonian is fundamentally different due to a $SU(2)$ symmetry under which the total magnetization constitutes a conserved quantity.

To experimentally probe this conservation law, we target the XXX Hamiltonian and measure the system's magnetization in the ordered many-body scenario of 32 atoms. The spin system for these experiments are represented by the $|\downarrow\rangle = |75S_{1/2}, m_j = 1/2\rangle$ and $|\uparrow\rangle = |75P_{3/2}, m_j = -1/2\rangle$ Rydberg state. The averaged interaction energy is defined as $J_{\mathrm{m}} = 1/N \sum_{i \neq j} J_{ij}$, with N the number of atoms. Using a $\pi/2$ pulse, the system is again initialized in the equatorial plane and the state reads $|\rightarrow\rangle_y^{\otimes N}$. The XXX Hamiltonian is engineered by subjecting the system to multiple cycles of periodic driving, each with a cycling time $t_c = 300$ ns. We observe an approximately constant magnetization for a time of 3 μs while the sequence is active, as expected for the target XXX Hamiltonian (see Fig. 3.4). After 3 μs, the driving is switched off, and the magnetization decays towards zero due to the natural XX Hamiltonian. In the next section, we explore this stalling of the dynamcis in a different regime.

Understanding experimental imperfections

To compare the dynamics of the system with simulations, we apply a moving-average cluster-expansion (MACE) method [151]. Here, we perform exact diagonalization of clusters of 12 atoms and average over all possible clusters with 32 atoms. SPAM errors and imperfect microwave rotations due to possible phase and power fluctuations are also included in the simulations (see [48, 127] for details). The blue solid line in Fig. 3.4 represents simulations without adjustable parameters, revealing good agreement with the experimental observations. However, when comparing the evolution to the pure target XXX Hamiltonian (red dashed line), small discrepancies become apparent.

We use our simulations as a tool to investigate the source of these differences. When removing the error occurring due to the imperfect microwave drive, we observe a significant increase in the stalled magnetization over the period of 3 μs (green solid line). Consequently, the primary cause of the decay is attributed to imperfections in the microwave system. Despite nearly complete conservation of magnetization, there are still small discrepancies in the natural evolution following the driving process (green solid line vs dashed red line). These discrepancies originate from interactions occurring during the finite pulse duration in the driving process, which are not considered in the AHT approach. These interactions cause the system to deviate from the precise product state expected from $\hat{H}_{\mathrm{XXX}}$ after the application of $\hat{H}_{\mathrm{driven}}$. Increasing the Rabi frequency by a factor of four compared to the experimental value leads to nearly perfect engineering in the simulations (orange line). This indicates that the condition $J_{\mathrm{m}} t_c \ll 2\pi \cdot 0.2$ already satisfies the requirement for nearly perfect engineering in the setting (see Eq. 3.10). A more detailed investigation of the performance of the engineering protocol as a function of different driving parameter is part of the following section.

3.3 Floquet Hamiltonian Engineering in a gas of atoms

In the previous section, we explored Floquet Hamiltonian Engineering in an ordered array of a few Rydberg atoms, with clear signatures that the dynamics are driven by the target Floquet Hamiltonian. In this section, we continue to investigate the engineering in a different regime: The introduced driving protocol is applied to an ultracold gas with hundreds of Rydberg atoms, representing a 3D spatially disordered many-body spin system.

The goal is to validate the engineering process, ensuring the faithful implementation of the target Hamiltonian in this many-body regime. To achieve this, we first conduct similar experiments as those described in the preceding section. As coherent oscillations are not resolved in disordered quantum systems with hundreds of atoms, we employ the magnetization freezing protocol. We focus on the implementation of the $SU(2)$ symmetric XXX Hamiltonian and provide a detailed analysis of the associated conservation law of the total magnetization. Here, we particularly analyze the performance of the engineering efficiency of our driving protocol concerning various driving parameters, including the cycling time.

In order to understand the experiments presented in this section, we briefly introduce the most relevant aspects of the experimental procedure [4] : For all measurements, the spin is encoded in the two Rydberg states $|48S_{1/2}, m_j = 1/2\rangle = |{\downarrow}\rangle$ and $|48P_{3/2}, m_j = 1/2\rangle = |{\uparrow}\rangle$. The interaction parameter in Eq. 3.3 is given by $C_3(\theta_{ij})/2\pi = (1 - 3\cos^2\theta_{ij}) \cdot 1.14\ \mathrm{GHz} \cdot \mu\mathrm{m}^3$. Due to our Rydberg excitation scheme, described in Appendix B, the positions of your few hundred Rydberg atoms in the

---

[4] To enhance the reader's understanding, our focus in this part is placed on the experimental results. A comprehensive introduction to the experimental setup, system preparation, readout, and strategies for controlling Rydberg spin is provided in Appendix B.

cloud are random, resulting in a disordered many-body system of N spins. To quantify the interaction strengths of our system, we take the mean over the sample $J_{\mathrm{m}} = 1/N \sum_i |\sum_j J_{ij}|$. Additionally, a magnetic field of 30 G is applied to induce Zeeman-level splitting, ensuring a two-level description of the system.

Before investigating the full potential of Floquet Hamiltonian Engineering in the final section of this chapter, this section focuses solely on the implementation of the $SU(2)$ symmetric XXX Hamiltonian

$$\hat{H}_{\mathrm{XXX}} = \sum_{i,j} J^x_{ij} \hat{S}^i_x \hat{S}^j_x + J^x_{ij} \hat{S}^i_y \hat{S}^j_y + J^x_{ij} \hat{S}^i_z \hat{S}^j_z \quad . \tag{3.18}$$

3.3.1 Freezing many-body dynamics in a gas of atoms

The first question that arises is how can one verify that our drive implements the Hamiltonian of Eq. 3.6 in a many-body regime where no exact numerical simulations are available? Additionally, our experimental system does not provide local resolution, making the system's magnetization the only observable. One of the most drastic effects consists of a potential freezing of this quantity, given the strong interactions in the many-body system, a phenomenon previously explored in the context of an ordered few-body system (see Sec. 3.2.2)

To experimentally probe this conservation law, we apply the protocol illustrated in Fig. 3.2 b), with a periodic drive targeting an XXX Hamiltonian. The protocol starts with exciting the atoms to the $|\downarrow\rangle^{\otimes N}$ Rydberg state. After applying a $\pi/2$ pulse, the spins are initialized in a product state denoted as $|\rightarrow\rangle_x^{\otimes N} = \frac{1}{\sqrt{2}}(|\downarrow\rangle + |\uparrow\rangle)^{\otimes N}$. This state implies that all spins are aligned along the x-direction in a Bloch sphere representation. The subsequent evolution of this state is governed by the Hamiltonian $\hat{H}(t)$, as defined in Eq. 3.5. Here, we have the flexibility to choose whether or not to apply the pulse sequence. At the end of this evolution which lasts for time t, the total magnetization is measured (see Appendix B).

We observe the system's magnetization dynamics without applying the periodic sequence. The evolution is described by $\hat{H}_{\mathrm{XX}}$ and results in a fast relaxation towards

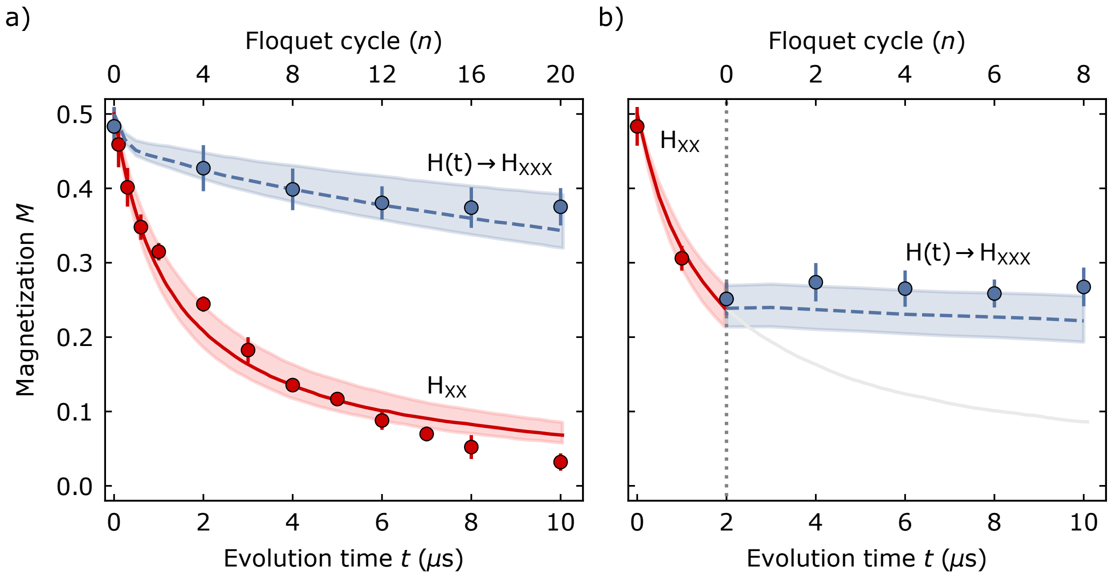

Figure 3.5: Engineering the Hamiltonian of an isolated spin system. a) Magnetization dynamics of a state polarized along the x-direction. Red points display the dynamics under the natural XX Hamiltonian and the blue points dynamics due to $\hat{H}(t)$, targeting an XXX Hamiltonian with $t_c = 500$ ns and $J_\mathrm{m}/2\pi = 0.2$ MHz. **b)** Evolution of magnetization after letting the system evolve under the natural interactions for 2 μs before switching on the drive ($t_c = 1$ μs). Lines are dTWA simulations of the respective dynamics under $\hat{H}_\mathrm{XX}$ (solid) and $\hat{H}(t)$ (dashed), including uncertainties of the Rydberg density (shaded areas). Figure and caption taken and adapted from [71].

a demagnetized state over a time of 10 μs, as shown by the red points in Fig. 3.5 a). The dynamics originate from the fact that the x-polarized state is not an eigenstate of the natural XX Hamiltonian and is far from equilibrium (similar as the experiments in Chap. 2). Furthermore, the system possesses no symmetry that conserves the system's magnetization. Next, we initialize the same state along the x-direction but this time apply the WAHUHA sequence, targeting a $\hat{H}_\mathrm{XXX}$ during the evolution time. The relaxation of the magnetization is significantly slowed down for this setting, as shown by the blue points in Fig 3.5 a). This effect is associated with the $SU(2)$ symmetric nature of our target Hamiltonian and the fact that the initial state constitutes an eigenstate of an XXX Hamiltonian. To verify that the dynamics stalling is independent of the initial state and can be applied dynamically, we perform an experiment where we split the evolution in two parts. First, we let the system evolve for 2 μs, creating an entangled state (which is not an eigenstate of $\hat{H}_{\mathrm{XXX}}$). Then, we suddenly switch on the WAHUHA sequence. The result is shown in Fig. 3.5 b). Within the first 2 μs, the magnetization relaxes to roughly half of its initial value. After switching on the periodic driving, we observe a complete freezing of the dynamics, as expected from $\hat{H}_{\mathrm{XXX}}$. This further demonstrates the dynamical realization of the desired engineered Hamiltonian on demand.

Contrary to what one might expect from a pure XXX Hamiltonian, the evolution depicted in Fig 3.5 a) is not entirely frozen. The disordered nature of our spin systems can provide an understanding of this observation (this contrasts the scenario of the ordered sample presented in the previous section). In general, Rydberg atoms in our sample have random distances between them. However, the Rydberg blockade effect (see Appendix A) imposes a lower bound for the minimal distance r_b between two adjacent atoms. In our scenario, the minimal distance translates into a maximum interaction strength of $J_{\mathrm{max}}/2\pi = 2\,C_3/(2\pi r_{\mathrm{b}}^3) = 18$ MHz. At this particular distance, spin pairs significantly violate the condition of Eq. 3.10 required for a valid zeroth-order effective time-independent description, as the cycling frequency $1/t_c = 2$ MHz is much slower. Higher-order terms in the Floquet Hamiltonian are no longer $SU(2)$ symmetric and lead to the observed slow remnant relaxation of the total magnetization. In contrast, the second scenario with the dynamically applied engineering sequence shown in Fig 3.5 b) shows a full freeze out of the dynamics. Here, strongly interacting spins are already demagnetized over the first 2 μs and do not contribute to the system's magnetization. Therefore, the periodically applied drives stall mainly the dynamic of the remaining magnetized spins. We note that this interpretation is qualitative, and the engineering performance will be studied in more detail in the following section. However, we modeled the full driving protocol represented by the Hamiltonian of Eq. 3.5 using semi-classical discrete truncated

Wigner approximation method (dTWA) [121] and found that it reproduces all essential features quantitatively.

3.3.2 Characterization of the engineering efficiency

As observed in Fig. 3.5 a) and discussed in the previous section, our periodic pulse sequence effectively manipulates dynamics that align with the expectations derived from the XXX Hamiltonian. In this section, we quantify the experimental deviation from the zeroth-order Floquet Hamiltonian and understand their origins. To achieve this, we define an efficiency metric for engineering the target Hamiltonian $\hat{H}_{\mathrm{XXX}}$ as $\mathcal{E}_{\mathrm{XXX}}(t) = \frac{M(t)}{1/2}$, where $M(t)$ represents the observed magnetization at time t. As the system's total magnetization is 1/2, an efficiency $\mathcal{E}_{\mathrm{XXX}}(t) = 1$ represents ideal engineering of $\hat{H}_{\mathrm{XXX}}$. For the subsequent investigations, we measure $\mathcal{E}_{\mathrm{XXX}}(t)$ at $t = 10\ \mu$s. We fix the mean interaction strength J_{m} of the sample and vary the cycling time t_c to adjust $1/(J_{\mathrm{m}}t_c)$. Fig. 3.6 a) shows the time traces of the evolution for two cycling times $t_c = 1\ \mu$s and 5 μs, from which we take the value at $t = 10\ \mu$s.

The resulting efficiency curve for various t_c is shown in Fig. 3.6 b). In the absence of the applied pulse sequence, where t_c approaches infinity, the efficiency becomes almost zero due to the relaxation of magnetization caused by $\hat{H}_{\mathrm{XX}}$ (similar to pure relaxation in Fig. 3.5 a). Decreasing t_c, and therefore driving the spin system faster, results in an increase in the observed efficiency. This increase can be attributed to the fact that an increasing number of spin pairs fulfill the fast driving condition of Eq. 3.10. In the theoretical framework, which assumes infinitely fast $\pi/2$ spin rotations, $\mathcal{E}_{\mathrm{XXX}}(t)$ is anticipated to continuously rise with $1/(J_{\mathrm{m}}t_c)$ as the driving approximates the zeroth-order Floquet Hamiltonian with higher precision. In contrast, we observe a convergence of the efficiency towards a finite value for the shortest achievable cycling times, which is also reproduced by dTWA simulations.

To understand this phenomenon, we take into account that interactions persist during the finite-time pulses of length $t_{\pi/2}$, making the delta-pulse approximation inadequate. For shorter cycling times t_c, an increasing number of pulses need to

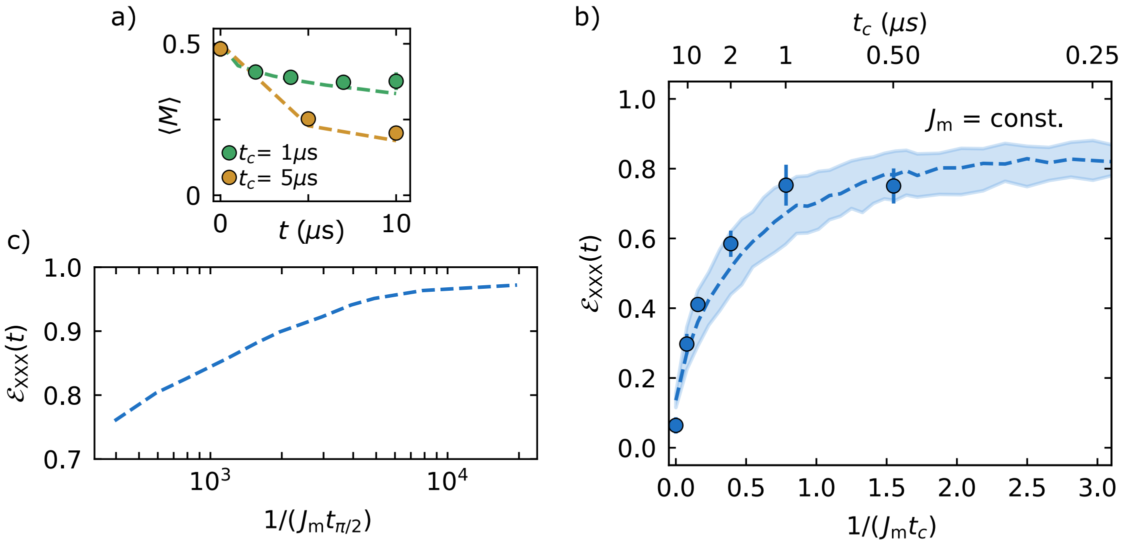

Figure 3.6: Efficiency of engineering the target Hamiltonian. a) Time traces of the magnetizations for cycling times $t_c = 1$ μs and 5 μs for a pulse width $t_{\pi/2} = 12.5$ ns. **b)** Efficiency at $t = 10$ μs as a function of $1/(J_\mathrm{m}t_c)$ for $t_{\pi/2} = 12.5$ ns. Dashed lines are dTWA simulations of $\hat{H}(t)$ with the respective sequence parameters and density uncertainties (shaded area). **c)** Numerical dTWA simulations of the efficiency at $t = 10$ μs with pulse widths ranging from $t_{\pi/2} = 12.5$ ns to 0.25 ns for $t_c = 50$ ns at $1/(J_\mathrm{m}t_c) = 16$. $J_\mathrm{m}/2\pi = 0.2$ MHz is the mean interaction strength for the experiment and theory. Subfigures (b,c)) and caption taken and adapted from [71].

be applied in order to measure the efficiency at the same time $t = 10$ μs. Consequently, the effect of finite pulse length and the fast driving condition of Eq. 3.10 start to compete for a given parameter setting. To achieve higher efficiency, it becomes necessary to further reduce the finite pulse length $t_{\pi/2}$, beyond the current shortest value determined by the bandwidth of our arbitrary waveform generator. To estimate the required pulse length for the nearly perfect engineering efficiency, we numerically simulate pulse lengths down to $t_{\pi/2} = 0.25$ ns at fixed $1/(J_\mathrm{m}t_c) = 16$. The results are shown in Fig. 3.6 c), and the efficiency approaches unity for $t_{\pi/2}$ on the order of 0.25 ns. We note that those conditions are within reach with today's cutting-edge microwave technology.

We note that unlike the prior investigations, our simulations do not incorporate microwave errors. Based on our observations, we conclude that the primary limitation in our experiments primarily arises from the finite pulse duration, as evidenced by the comparison to dTWA simulations.

3.4 Quantum simulation experiments with engineered Rydberg atoms

In the preceding two sections, we validated Floquet Hamiltonian Engineering and demonstrated its ability to manipulate the dynamics of quantum spin systems. This manipulation allowed us to finely tune coherent oscillations and effectively freeze many-body quantum dynamics, whether with a small number of atoms in an ordered scenario or in disordered scenarios involving a larger number of atoms.

In order to demonstrate that Floquet Hamiltonian Engineering is suitable for quantum simulations with tunable interactions, this section presents experiments making use of the ability to arbitrarily tune the delay times and therefore the target XYZ Hamiltonian in Eq. 3.6. We first investigate how symmetries in the spin Hamiltonian affect far-from-equilibrium dynamics in the disordered three-dimensional scenario. Finally, we briefly illustrate that engineering a 1D chain in a domain-wall state can distinguish the transport properties of the XXZ Hamiltonian.

3.4.1 Out-of-equilibrium dynamics and symmetry breaking

In this paragraph, we investigate symmetries in the XYZ Hamiltonian and their effect on magnetization dynamics. The observed magnetization freezing in the previous set of measurements (see Fig. 3.5) directly results from a $SU(2)$ symmetry in the system originating from the engineered XXX Hamiltonian. This symmetry can broken by choosing the driving control parameters in a way that $\delta_x = \delta_y \neq \delta_z$, transforming the effective description from an XXX Hamiltonian to an XXZ Hamiltonian. Typical sequences archiving this transformation are illustrated in Fig. 3.7 a). In the

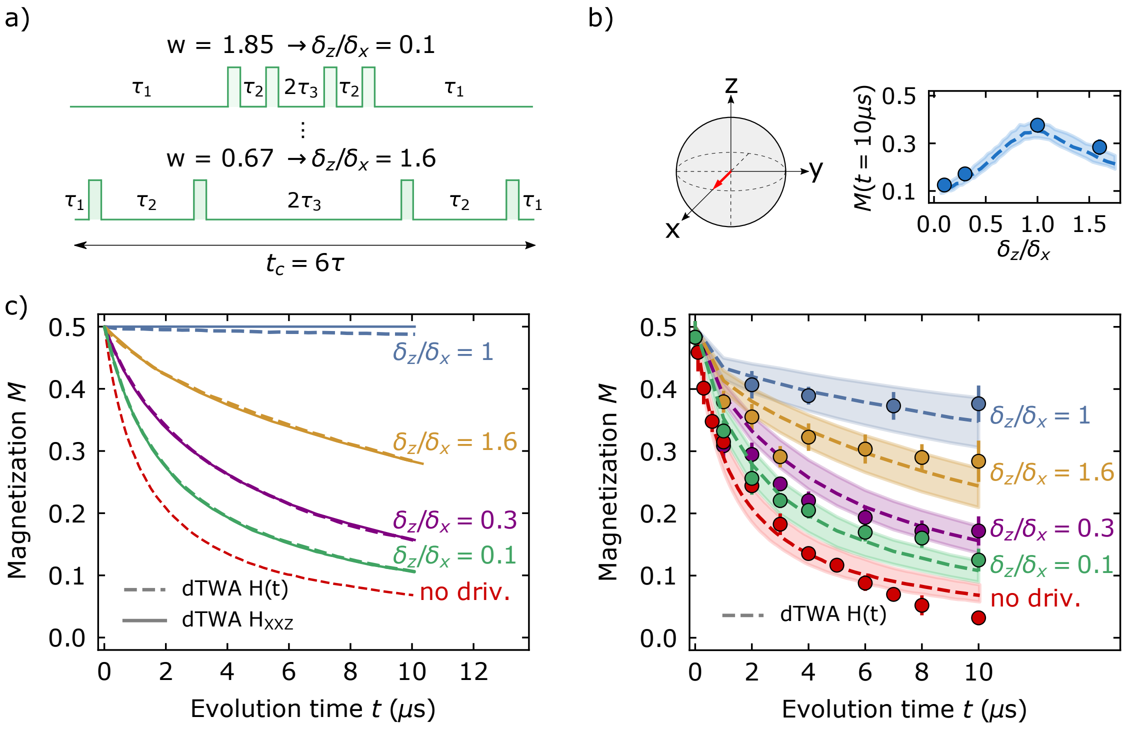

Figure 3.7: Engineered out-of-equilibrium dynamics. a) Illustration of pulse sequences designed to engineer XXZ Hamiltonian with anisotropy $\delta_z/\delta_x = 0.1$ and 1.6. Control parameters u and v are chosen such that $u = (w+v)/2$ and $v = 1$. **b)** Bottom: Magnetization dynamics for drives targeting the XXZ Hamiltonian with different anisotropies, with $t_c = 1\ \mu$s, $t_{\pi/2} = 12.5$ ns, $J_\mathrm{m}/2\pi = 0.2$ MHz. The shaded area corresponds to the density uncertainty in dTWA simulations of $\hat{H}(t)$. The red arrow on the Bloch sphere (top left) indicates the initial state. Magnetization at $t = 10\ \mu s$ as a function of the anisotropy parameter δ_z/δ_x is shown in the top right. **c)** Numerical dTWA simulations of the driven time-dependent Hamiltonian $\hat{H}(t)$ (dashed lines) and the exact XXZ Hamiltonian for various ratio δ_z/δ_x (solid lines) with improved engineering conditions: $t_c = 55$ ns, $t_{\pi/2} = 1.25$ ns, $J_\mathrm{m}/2\pi = 0.2$ MHz. Figures and caption taken and adapted from [71].

absence of $SU(2)$ symmetry, the magnetization of our initial state is expected to exhibit relaxation rather than being conserved.

We measure the magnetization dynamics as a function of the evolution time for anisotropy parameters δ_z/δ_x ranging from 0.1 to 1.6. As shown in Fig. 3.7 b) (bottom), the magnetization relaxes on vastly different time scales and follows a non-exponential fashion (this behavior is characteristic for disordered systems and has been previously observed in Chap. 2). Notably, the relaxation process exhibits a non-monotonic behavior, as depicted on the top right of Fig. 3.7 b), where we display the final magnetization values at a fixed time of 10 μs. As δ_z/δ_x increases, the relaxation slows down until it reaches the $SU(2)$ symmetric Heisenberg point at $\delta_z/\delta_x = 1$. Beyond this point, the relaxation accelerates again, which is consistent with expectation from the XXZ Hamiltonian and is also reproduced by time-dependent dTWA simulations targeting the XXZ Hamiltonian. Therefore, the observed dynamics are features of the broken $SU(2)$ symmetry in the system. As explained earlier, the dynamics of the driven system slightly differ from those expected from the XXZ Hamiltonian due to finite pulse width and the failure to fulfilling the fast driving condition in Eq. 3.10. We propose to explore numerically a scenario that currently exceeds the capabilities of our experimental setup, where both pulse length and cycling time can be significantly reduced ($t_{\pi/2} = 1.25$ ns and $t_c = 50$ ns). For this setting, Fig. 3.7 c) shows a comparison of the driven system with an XXZ Hamiltonian from the anisotropy parameters of the experiment. Firstly, we highlight that the non-monotonous dynamics observed in the experiment is accurately reproduced by both numerical simulations. Secondly, both numerical simulations agree well with each other. This finding indicates that in this specific regime, the Hamiltonian $\hat{H}_{\mathrm{XXZ}}$ provides a reliable representation of $\hat{H}(t)$.

The XXZ Hamiltonian still features a $U(1)$ symmetry, independent of the anisotropy δ_z/δ_x. The conservation law associated with this symmetry consists of the system's magnetization along the z-direction. To demonstrate this conservation, we initialize the system in a state possessing magnetization components along the y- and

z-direction (see Fig. 3.8 a)). Experimentally, this is achieved by the application of a $\pi/4$ pulse. Fig. 3.8 b) shows the time evolution of the three different magnetization components M_x, M_y, and M_z for a $U(1)$ symmetric XXZ Hamiltonian. While the y magnetization relaxes towards zero, the magnetization along the z-direction shows no relevant relaxation, which is consistent with an XXZ Hamiltonian. Due to the effectiveness of the Floquet Hamiltonian description, periodic driving allows us to even break the remaining $U(1)$ symmetry by targeting a fully anisotropic XYZ Hamiltonian (therefore we select $\delta_x \neq \delta_y \neq \delta_z$). As a consequence, we observe an additional relaxation of the z magnetization as shown in Fig. 3.8 c). The relaxation of the z magnetization occurs faster than that of the y magnetization due to their respective scaling factors. The dynamics of the z magnetization scale with $\delta_x - \delta_y = 0.9$, while the dynamics of the y magnetization scale with $\delta_x - \delta_z = 0.45$ (see Appendix C).

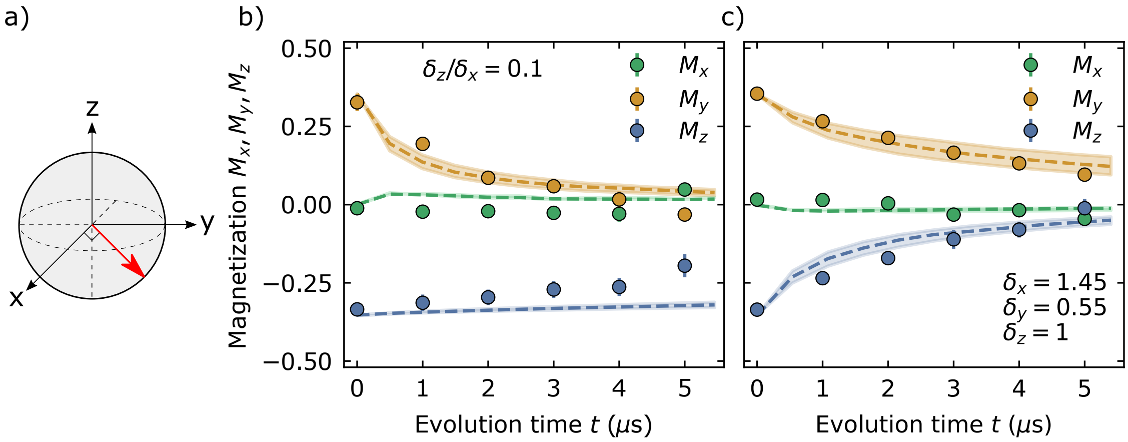

Figure 3.8: Consecutive symmetry breaking for a dual component initial state. **a)** Representation of the state initialized with a $\pi/4$ pulse on the Bloch sphere. **b)** Dynamics of the magnetization components for an XXZ Hamiltonian. **c)** Dynamics of the magnetization component for a fully anisotropic XYZ Hamiltonian. Parameters are $t_c = 0.5\ \mu s$, $t_{\pi/2} = 10.7$ ns, $J_\mathrm{m}/2\pi = 0.4$ MHz and the shaded areas correspond to the density uncertainty of dTWA simulations of $\hat{H}(t)$ (dashed lines). Figure and caption taken and adapted from [71].

3.4.2 Domain wall dynamics in a 1D atom chain

We finally demonstrate that Floquet engineering can be employed to explore the transport properties of many-body spin systems. To achieve this, we prepare the system in a 1D domain wall state where a boundary separates atoms in the $|\downarrow\rangle$ from atoms in $|\uparrow\rangle$ state. The arrangement of the atoms is illustrated in Fig. 3.9 a). The dynamics of this domain wall state strongly depend on the anisotropy of the XXZ Hamiltonian in Eq. 3.13, due to two competing effects. Spin flips occur at a rate of J_x, resulting in a melting of the domain wall, countered by an accompanying energy cost of $2J_z$ that preserves the domain wall. Theoretical studies of this scenario predict melting of the domain wall for $\delta_z/\delta_x < 1$ [152, 153] ballistic in time, a diffusive behavior for $\delta_z/\delta_x = 1$ [154], and freezing of the domain wall for a long time if $\delta > 1$ [153].

For our investigations, the spin is encoded in the $|\downarrow\rangle = |75S_{1/2}, m_j = 1/2\rangle$ and $|\uparrow\rangle = |75P_{3/2}, m_j = -1/2\rangle$ Rydberg states. At a distance of $a =$ 19 μm, the nearest neighbor interaction is $J/2\pi = 270$ kHz and $J_\mathrm{m}/2\pi = 600$ kHz, fulfilling the fast cycling condition in Eq. 3.10. By utilizing the ability to locally address the spins, we initialize five in the $|\downarrow\rangle$ and five in the $|\uparrow\rangle$ state, thus implementing the domain wall state. The evolution of this state is explored under the XXZ Hamiltonian with anisotropy $\delta_z/\delta_x = 0, 1, 2$. Fig. 3.9 b) display the single spin magnetization $\langle\sigma_i^z\rangle$ as a function of the normalized time $t' = tJ_x(\delta_z/\delta_x)/(J \cdot 1\mu\mathrm{s})$. For $\delta_z/\delta_x = 0, 1$, we observe the melting of the domain wall, resulting in an approximately uniform magnetization profile for $t' \geq 3$. The domain wall melts more slowly for $\delta_z/\delta_x = 1$, as expected from the XXZ Hamiltonian. In the case of larger anisotropy $\delta_z/\delta_x = 2$, the domain wall is conserved, and the magnetization profile shows little dynamics for $t' \geq 1$, indicating freezing of the dynamics. A detailed analysis of the transport properties in this few body system is beyond the scope of this thesis but discussed in dissertation of Pascal Scholl [127]. Therefore, our Hamiltonian manipulation allows us to differentiate between diverse spin-transport behaviors corresponding to varying values of the anisotropy δ_z/δ_x.

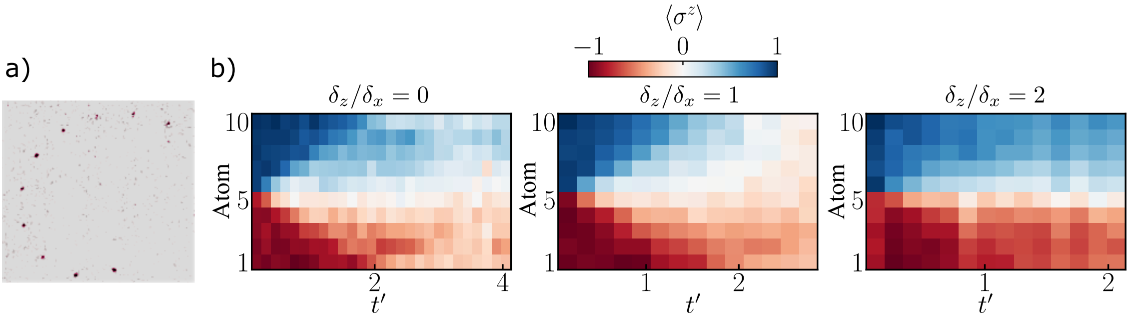

Figure 3.9: Dynamics of a 1D domain-wall state under an XXZ Hamiltonian. **a)** Fluorescence image of the 10 atoms used to realize 1D domain-wall state with open boundary conditions. **b)** Density maps of the temporal evolution of the z magnetization of each spin as a function of t' after preparation of a domain wall state with five atoms in $|{\uparrow}\rangle$ and five atoms in $|{\downarrow}\rangle$ for anisotropies $\delta_z/\delta_x = 0, 1, 2$. Figures and caption taken and adapted from [48].

3.5 Summary and discussion

Summary

In this chapter, we explored how periodic driving can be employed to realize tunable interaction Hamiltonians in many-body quantum spin systems of Rydberg atoms. First, we have introduced the general concept and mathematical framework necessary to understand our driving protocol, which consists of four $\pi/2$ pulses with adjustable delay times. Our engineering approach transforms an XX Hamiltonian into an effective XYZ form, where the explicit interaction parameter can be tuned by varying the delay time between the pulses.

Afterward, we presented the experimental implementation of the protocol in an ordered array of a few Rydberg atoms, realized with optical tweezers. Employing this setup allowed us to benchmark the engineering by observing the coherent oscillation dynamics of two atoms. In this configuration, we observed no significant difference between the engineered dynamics and the expected dynamics from the target Hamiltonian. Following this demonstration, we proceeded to increase the system size to an array of 32 atoms. In this ordered scenario, we measured and characterized the dynamical freezing of magnetization relaxation dynamics. We identified interactions during the pulses as a primary source of imperfections in this array setup, along with minor imperfections in the microwave.

We continued with the validation of Floquet engineering in a completely different regime: a 3D spatially disordered gas of Rydberg atoms. Similar to the implementation in the Rydberg array, we observed the freezing of magnetization dynamics. Remarkably, this freezing can be dynamically turned on and off by switching the pulse sequence. Since we also observed small deviations from the expected XXX Hamiltonian dynamics, we proceeded with a characterization of the engineering efficiency as a function of the sequence time and driving Rabi frequency. This allowed us to identify interactions during the finite-width $\pi/2$ pulses as the primary source for imperfect engineering in the current experimental setup.

After validation of the protocol, we proceeded to explore the full potential of Floquet engineering by observing the magnetization dynamics under the general XYZ Hamiltonian. In particular, we implemented drives that consecutively reduce the symmetries in the system, breaking the $SU(2)$ and $U(1)$ symmetries. As an experimental probe, we employed a measurement of the magnetization components that are conserved by these symmetries. Finally, we presented experiments demonstrating the ability to study transport properties of the XXZ Hamiltonian with tunable anisotropy in a 1D domain-wall state consisting of 10 atoms.

Discussion

In chronological order, the experiments in the disordered atomic gas were conducted before those in the tweezer array. Consequently, it was initially not possible to directly observe the engineering of the underlying coherent oscillation behavior in our experimental setup in Heidelberg. The collaboration with Antoine Browaeys' group, therefore, represents a significant extension, which has allowed for an in-depth characterization of the engineering method in a distinct regime and with distinct observable.

The Floquet Hamiltonian Engineering techniques open up opportunities to explore a wide range of spin models. When combined with the flexibility offered by the Rydberg tweezer-based experiment, one gains nearly complete control over the Hamiltonian parameters, which are determined by the atom arrangement and the chosen model. The elegance of this method lies in its implementation, where arbitrary interactions can be realized by simply adjusting the delay times of global $\pi/2$ pulses, a straightforward task with an Arbitrary Waveform Generator. In contrast to global control pulses, it would be interesting to investigate the effect of local pulses, potentially enhancing the landscape of realizable Hamiltonian. In addition, the approach is not restricted to Rydberg atoms but can be applied on any isolated quantum system with the capability to apply periodic driving. This has recently been demonstrated to tune many-body Hamiltonians in cold molecules [33] and trapped ions [155]. In the context of quantum simulation, the capability of engineering arbitrary XYZ models can be directly applied to address open question ranging across different regimes, including the study of quantum thermalization [9], spin transport [156] or information scrambling [157].

Beyond its applications in quantum simulation, Floquet engineering techniques have diverse potential uses in various quantum technologies. There exist well defined procedures to design multi-pulse sequences for specific target applications, such as optimal sensing, where undesired terms in the Hamiltonian are decoupled [141]. In the context of quantum-enhanced sensing, our demonstrated ability to dynamically freeze dynamics in the system has recently been employed to stall spin squeezing on demand [94]. Another promising route would include investigations in quantum systems consisting of more than two-level which opens the path towards the investigation of richer spin models [158].

CHAPTER 4

Time-reversal in a quantum many-body spin system

Parts of this chapter, are based on the following manuscript, from which parts of the text have been taken verbatim:

Time-reversal in a quantum many-body spin system
S. Geier, A. Braemer, E. Braun, M. Müllenbach, T. Franz, M. Gärttner,
G. Zürn, M. Weidemüller
Submitted

As described in the previous two chapters, dynamics in quantum systems composed of Rydberg atoms can be controlled by carefully selecting the spin encoding Rydberg states. Furthermore, a periodically applied drive allows for the implementation of arbitrary spin models by introducing new effective interaction terms. In the present chapter, we further explore the ability to shape the dynamics of strongly interacting systems by combining these two approaches.

One of the impressive aspects of unitary dynamics in quantum systems is the intriguing ability to effectively reverse the arrow of time by altering the sign of the Hamiltonian. An early example of this technique is found in spin echo experiments, where the Hamiltonian, and thus the dynamics, are reversed by effectively flipping the direction of random magnetic fields that individual spins experience [144, 159]. This reversal causes an apparent demagnetized state to evolve back-in-time into a magnetized state. While spin echo experiments are based on reversing single-particle dynamics, it is also possible to invert the sign of an interacting many-body Hamiltonian [160], leading to the reversal of strong correlations and entanglement in complex states. This not only shows the remarkable behavior associated with time reversal but also provides an important tool for quantum technologies, ranging from metrology to quantum simulation.

Experimental approaches that implement and exploit time-reversal protocols in quantum metrology show phase sensitivity beyond the standard quantum limit, even with limited detection efficiency in collective systems [161–164]. Furthermore, by time-reversing the evolution of many-body system, the effect of decoherence on quantum simulation experiments has been characterized in gate-based quantum processors and nuclear magnetic resonance samples [134, 165]. The capability of reversing time also provides insights into complex phenomena of interacting quantum systems such as information scrambling by measuring out-of-time-order correlators [157], as demonstrated in collective spin models with trapped ions [166], nuclear magnetic resonance samples in mixed states [167], and through a digital approach in superconducting qubits [168]. In this context, the realization of time-reversal in a new class of systems, namely, isolated quantum spin systems featuring power-law interactions holds significant importance, as they occur naturally in various quantum simulation platforms, including Rydberg atoms [169], solid-state spin defects [170], and ultracold molecules [33, 65]. Realizing time-reversal in isolated system with power-law interactions would therefore lay the foundation for various applications.

In this chapter, we demonstrate the reversal of quantum dynamics, governed by a tunable many-body Hamiltonians in a Rydberg spin system. As discussed in Chap. 2 and Chap. 3, Rydberg atoms constitute an ideal platform for quantum science applications as they enable the exploration of pure quantum states in random [49, 171] and controllable spatial geometries [58–60]. Most importantly, their decoupling from the environment enables studying unitary dynamics of a broad class prototypical quantum spin models with long-range interactions [47,49,169,171]. Our approach is based on reversing the sign of a many-body spin Hamiltonian by applying a state transfer during the evolution, effectively changing the spin encoding in the Hilbert space. We demonstrate the time reversal by reviving the magnetization of an initially magnetized state after having fully relaxed and identify experimental contributions to which the time-reversal is sensitive. Finally, by combining the time reversal protocol with Floquet engineering techniques as presented in Chap. 3, we extend the reversal of dynamics to tunable classes of spin Hamiltonians.

This chapter is structured as follows:

- **Section 4.1:** This section introduces an experimental protocol used to reverse the sign of a many-body Hamiltonian within the Rydberg manifold. It is based on transferring the spin state between two Rydberg state combinations, effectively changing the pseudo-spin encoding.

- **Section 4.2:** Here, we implement the introduced reversal protocol in the experiment and demonstrate the revival of many-body quantum dynamics. We explore the reversal of the evolution of a state that demagnetized due to strong spin interactions, demonstrating how it returns back to a magnetized state over time.

- **Section 4.3:** In this section, we further study the performance of our time-reversal protocol and identify the sources for current perturbations. Therefore, we numerically study the influence of atomic motion and finite transfer efficiency on the amount of reversed magnetization.

- **Section 4.4:** Finally, we combine the reversal protocol with Floquet Hamiltonian Engineering as introduced in Chap. 3 and demonstrate the revival of magnetization dynamics for a tunable XXZ Hamiltonian.

4.1 Time-reversal protocol

In this first section, we introduce an experimental protocol that allows for the reversal of the dynamics of an isolated quantum spin system. In general, the evolution of quantum systems is governed by the Schrödinger equation, which leads to unitary dynamics of the particles. An inherent characteristic of these dynamics is that a change in sign of Hamiltonian effectively inverses the arrow of time:

$$e^{-iHt} \to e^{-i(-H)t} \equiv e^{-iH(-t)} \quad . \tag{4.1}$$

This seemingly simple relation has drastic effects. Starting with a basic product state, the trajectory of a system that might have led to a strongly correlated, entangled state, can be reversed, effectively returning the system to its original uncorrelated product state. To realize a sign change in the interaction Hamiltonian, it relies on changing the spin representation within the Rydberg manifold. In the following, we will introduce the time-reversal protocol and discuss the methods employed to engineer this change in sign.

4.1.1 Time-reversal through spin encoding

The general idea of our protocol is sketched in Fig. 4.1. Experimental platforms used to simulate the dynamics of a spin-1/2 system consists of particles that offer various internal degrees of freedom to encode the two pseudo-spin states. This includes, for example, two states in the larger Hilbert space of rotational states in polar molecules [32, 33] or two states in the larger Hilbert space of highly excited states in Rydberg systems. For Rydberg atoms, all these states offer different types of interactions as introduced in Chap. 2. Now, the goal is to identify subspaces in this large Hilbert space, which effectively encode the same interaction Hamiltonian but with an opposite sign. In a first set of encoding states, the interactions are described by a Hamiltonian H_{int}, as illustrated by the red lines in Fig. 4.1. The unitary evolution in this system is governed by $\hat{U} = e^{-iH_{\text{int}}t}$. Now, the quantum state can be coherently transferred into the second subspace of spin-encoding states by $|\downarrow\rangle_1 \rightarrow |\downarrow\rangle_2$ and $|\uparrow\rangle_1 \rightarrow |\uparrow\rangle_2$. This coherent transfer can be realized using two consecutive π pulses. In this second set of encoding states, the dynamics are governed by a Hamiltonian $-kH_{\text{int}}$ and the unitary evolution reads $\hat{U} = e^{ikH_{\text{int}}t}$, as illustrated by the blue lines in Fig. 4.1. Therefore, the sign of H_{int} is reversed for the same Hamiltonian, up to a dimensionless scaling factor k.

Implementation with Rydberg atoms

We apply this protocol to dipolar-interacting Rydberg atoms and identify state combinations that fulfill the requirements of the previous section. The first pseudo-spin encoding consists of Rydberg states $|\downarrow\rangle_1 = |nS\rangle$ and $|\uparrow\rangle_1 = |nP\rangle$, shown as red state combinations. The direct dipolar exchange interactions between these two $S-$ and $P-$states can be represented using a Heisenberg XX Hamiltonian (see Sec. 2.1)

$$\hat{H}_{\text{XX}} = \sum_{i,j} J_{ij} \left(S_x^i S_x^j + S_y^i S_y^j \right) \quad , \tag{4.2}$$

where S_α^i ($\alpha \in x, y, z$) are spin-1/2 operators and $J_{ij} = 2C_3(1 - 3\cos^2\theta_{ij})/r_{ij}^3$. C_3 is the dipolar coupling parameter, θ_{ij} the angle between atom i and j and the quantization axis, and r_{ij} their spatial separation. Therefore, the evolution in the first spin-encoding subspace is governed by $\hat{H}_{\text{XX}}$ and lasts for a time t. Subsequently, the spins are coherently transferred into the second set of spin-encoding states: $|\downarrow\rangle_1 \rightarrow |\downarrow\rangle_2 = |n'P'\rangle$ and $|\uparrow\rangle_1 \rightarrow |\uparrow\rangle_2 = |n'S'\rangle$. We decided to perform the transfer by applying two consecutive π pulses on both states. As these states represent another set of Rydberg $n'P'$ and $n'S'$ states, the evolution is also governed by a XX model, as shown in Eq. 4.2. As will be discussed in the following section, by carefully selecting the specific states, one can engineer a change in the sign of the coupling parameter, such that $C_3 \rightarrow -kC_3$ with $k = |C_3^1/C_3^2|$, representing the ratio between the coupling parameters in the two spin encoding. Therefore, the time evolution in the second spin system follows an XX Hamiltonian with a changed sign, effectively realizing a time-reversal operation with Rydberg atoms.

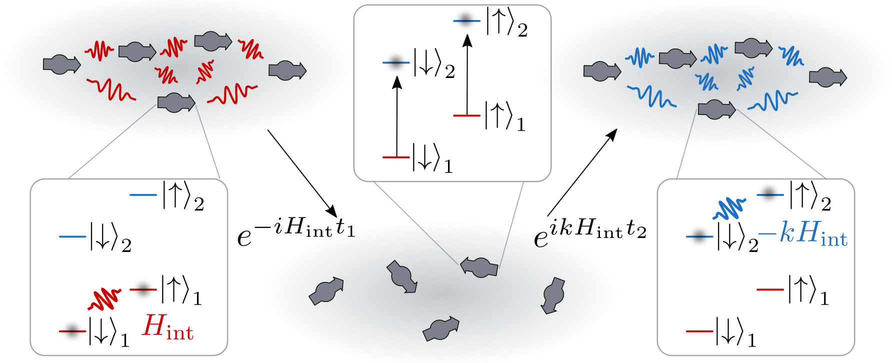

Figure 4.1: Time-reversal on a Rydberg quantum many-body system. Sketch of the time-reversal protocol. The time-reversal is based on transferring the state between two spin-1/2 encodings in the Rydberg manifold: $|\downarrow\rangle_1 = |nS\rangle, |\uparrow\rangle_1 = |nP\rangle$ and $|\downarrow\rangle_2 = |n'S'\rangle, |\uparrow\rangle_2 = |n'P'\rangle$. The unitary evolution in the first spin encoding is given by H_{int} and illustrated by the red lines between the spins. Coherently transferring the state into the second spin encoding state leads to unitary evolution under $-kH_{\text{int}}$, with k being a dimensionless parameter (illustrated by the blue lines between the spins). Figure and caption taken and adapted from the manuscript Geier et al. [172].

4.1.2 Sign changing Rydberg interactions

Our time-reversal protocol is based on dividing the overall evolution into subsets of spin-encoding states with opposite signs in the XX Hamiltonian. In this section, we will briefly discuss how the sign of the resonant dipole-dipole interactions changes by properly selecting the states. The dipole-dipole interactions were introduced in Sec. 2.1. Considering the basis $\{|\downarrow\uparrow\rangle, |\uparrow\downarrow\rangle\}$ the Hamiltonian for two atoms can be expressed as:

$$\hat{H}_{\text{DDI}} = \frac{1-3\cos^2\theta}{r^3}\begin{pmatrix} 0 & C_3 \\ C_3 & 0 \end{pmatrix} \tag{4.3}$$

with the interaction coefficient

$$C_3 = \frac{1}{4\pi\epsilon_0}\langle\uparrow\downarrow|\hat{d}_1^0\hat{d}_2^0 + 1/2\left(\hat{d}_1^+\hat{d}_2^- + \hat{d}_1^-\hat{d}_2^+\right)|\downarrow\uparrow\rangle \quad , \tag{4.4}$$

with $\hat{d}_i^0 = \hat{d}_i^z$ and $\hat{d}_i^\pm = -1/\sqrt{2}(\hat{d}_i^x \pm i\hat{d}_i^y)$.

In the matrix element for C_3, depending on the involved states $|\downarrow\rangle$ and $|\uparrow\rangle$, only one of the three terms contributes. Here, it becomes important to consider the involved m_j quantum numbers and particularly their difference $q = m_j^{\downarrow} - m_j^{\uparrow}$, which are affecting the sign of the C_3 coefficient.

For $q = 0$, only the first term contributes, while for $q = \pm 1$, the second or third term contributes. Therefore, for state combinations with $q = 0$, we obtain $C_3 = \langle\downarrow|\, \hat{d}_1^0 \,|\uparrow\rangle \langle\uparrow|\, \hat{d}_2^0 \,|\downarrow\rangle = |\, \langle\downarrow|\, \hat{d}^0 \,|\uparrow\rangle \,|^2$. Here, we used the complex conjugate relation $(\hat{d}^0)^\dagger = \hat{d}^0$. Hence, state combinations with $q = 0$ always yield a positive interaction coefficient. In contrast, for state combinations with $q = +1$, the interacting coefficient reads $C_3 = \langle\downarrow|\, \hat{d}_1^+ \,|\uparrow\rangle \langle\uparrow|\, \hat{d}_2^- \,|\downarrow\rangle = -|\, \langle\downarrow|\, \hat{d}^+ \,|\uparrow\rangle \,|^2$. Here, we used the complex conjugate relation $(\hat{d}^+)^\dagger = -\hat{d}^-$. Therefore, interaction coefficients for these state combinations are always negative. The same reasoning applies for $q = -1$ transitions. We note that this reasoning is valid for general states in the Rydberg manifold that are dipole-dipole coupled with $q = m_j^{\downarrow} - m_j^{\uparrow}$. In the following, we utilize this property to realize two spin-encoding subspaces with opposite sign in the interaction Hamiltonian.

4.2 Time-reversal of quantum many-body dynamics[1]

The previous section introduced a protocol for reversing many-body quantum dynamics by dividing the evolution in two spin-encoding subspaces in the Rydberg manifold. We now apply this scheme to our spin system of Rydberg atoms [2]. In general, time reversal can be observed in many observable of the system, including the return fidelity to the initial state or reversal of the variance of observables. Our approach consists of reversing the relaxation dynamics of a magnetized spin system,

---

[1] Taken verbatim from the manuscript Geier et al. [172] with minor adaptions for the ease of readability.

[2] To enhance the reader's understanding, our focus in this part is placed on the experimental results. A comprehensive introduction to the experimental setup, system preparation, readout, and strategies for controlling Rydberg spin is provided in Appendix B.

similar to the relaxation measurements presented in the previous chapters.

Fig. 4.2 a) illustrates the experimental sequence. We perform a global two-photon excitation to the $|\downarrow\rangle_1 = |61S_{1/2}, m_j = 1/2\rangle$ Rydberg state in our ultracold gas of rubidium 87 atoms. The system is spatially disordered due to the random positions of the Rydberg atoms in the cloud. The Rydberg density sets a typical length scale which leads to a typical energy scale quantified by the median of the nearest neighbor interaction energy $J_{\mathrm{m}} = \mathrm{median}_j \max_i |J_{ij}|$. The explicit parameter of the experiments presented in this chapter can be found at the end of Sec 4.3. Following the excitation, a microwave $\pi/2$ pulse to $|\uparrow\rangle_1 = |61P_{1/2}, m_j = 1/2\rangle$ initializes the spins in a magnetized state in the equatorial plane of the Bloch sphere, corresponding to the first set of spin-encoding states. The subsequent evolution for a time t_1 follows an XX Hamiltonian as described in the previous section, resulting in a complex many-body state. Our selection of states yield a positive interaction coefficient $C_3^1/2\pi = 3.2$ GHzμm^3. After this first evolution period, we coherently transfer the spin state into the system, encoded with a set of $|\downarrow\rangle_1 \rightarrow |\downarrow\rangle_2 = |61P_{1/2}, m_j = -1/2\rangle$ and $|\uparrow\rangle_1 \rightarrow |\uparrow\rangle_2 = |62S_{1/2}, m_j = 1/2\rangle$ Rydberg states. We perform this transfer by the application of two consecutive π pulses with Rabi frequencies $\Omega/2\pi = 9$ MHz and 11 MHz, respectively. The subsequent evolution in this second spin system lasts for a time t_2 and follows again an XX Hamiltonian. However, due to the selection of the involved states, we obtain a negative sign for the interaction coefficient $C_3^2/2\pi = -2.8$ GHzμm^3. The ratio between the coupling parameters is given by $k = 1.1$. At the end of this sequence, we readout the magnetization in the equatorial plane M_ϕ. Our detection method is based optically exciting the $|\downarrow\rangle_1 = |61S_{1/2}, m_j = 1/2\rangle$ state and therefore, we transfer the state back into the first spin system and perform the readout using a tomographic readout of the phase contrast (see Appendix B).

The time evolution of the magnetization without state transfer is shown as red circles in Fig. 4.2 b). Starting from a fully magnetized state, the magnetization relaxes towards a demagnetized state within the first ~ 0.7 μs. This relaxation is driven by the XX interactions and has also been observed in Chap. 2 and Chap. 3.

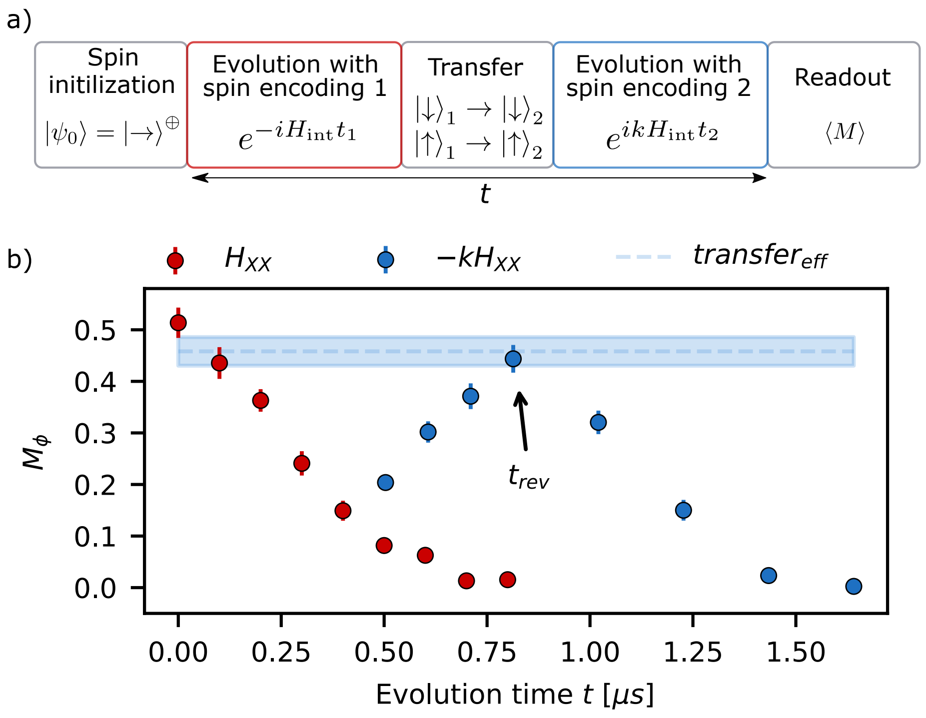

Figure 4.2: Reversal of magnetization dynamics. a) Experimental protocol to measure time reversal of the magnetization dynamics. The two spin encoding states are represented by $|{\downarrow}\rangle_1 = |61S_{1/2}, m_j = 1/2\rangle$, $|{\uparrow}\rangle_1 = |61P_{1/2}, m_j = 1/2\rangle$, $|{\downarrow}\rangle_2 = |61P_{1/2}, m_j = -1/2\rangle$, $|{\uparrow}\rangle_2 = |62S_{1/2}, m_j = 1/2\rangle$ and the state transfer is performed by two consecutive π pulses. **b)** Magnetization dynamics in the first spin encoding states without state transfer (red circles) and with state transfer (in the second set of encoding states), applied after evolving for $t_1 = 0.4$ μs in the first spin system (blue circles). The dashed line displays the state transfer efficiency: the magnetization after transferring the state for $t_1 = t_2 = 0$. The median interaction strength is $J_{\mathrm{m}}/2\pi = 0.43$ MHz. Figures and caption taken and adapted from the manuscript Geier et al. [172].

For the same spin initialization, we now apply the transfer pulses after an evolution time $t_1 = 0.4$ μs, at which point the magnetization relaxed to $M \sim 0.15$. This changes the subsequent evolution in second spin system drastically (blue circles in Fig. 4.2 b)). Instead of relaxing further into a demagnetized state, the system evolves back into a magnetized state after a time $t_2 = 0.41$ μs (or total time $t = 0.81$ μs). This revival of magnetization is expected for a system that evolves back in time or -as done here- for which the sign of the Hamiltonian is reversed as apparent from the unitary evolution of the magnetization $\langle M_\phi(t_1 + t_2)\rangle = \langle\psi_0|e^{iH_{\mathrm{XX}}(t_1 - kt_2)} M_\phi e^{-iH_{\mathrm{XX}}(t_1 - kt_2)}|\psi_0\rangle$ which revives to $M_0 = \langle\psi_0|M_\phi|\psi_0\rangle$ at $t_1 = kt_2$. We note that the time t_{rev}, where the reversal occurs, slightly deviate from theoretical expectation. We expect a ratio between the coupling parameter of $k = 1.1$ but measure $k = 1.03$. We attribute this small difference to interaction times during the finite width microwave pulses which are not included in the theoretical value. The light blue dashed line shows the transfer efficiency, defined as the magnetization obtained after the state transfers with no evolution time i.e. $t_1 = t_2 = 0$, and represents the maximally possible achievable magnetization after the evolution with the reversed Hamiltonian, accounting for infidelities during the transfer. For longer evolution times, the magnetization starts to relax again and ends up in a demagnetized state after ~ 1.6 μs, consistent with expectations for an XX Hamiltonian.

4.3 Time-reversal efficiency[3]

Time-reversal protocols are generally extremely sensitive to perturbations or decoherence, given the complexity of quantum states arising from many-body interactions. To assess the influence of perturbations, such as atomic motion or admixture of other atomic states, we characterize the long-time behavior ($J_{\mathrm{m}}/2\pi \cdot t > 1$) of our protocol by measuring the amount of reversed magnetization at the reversal time $t_{\mathrm{rev}} = t_1 + k \cdot t_1$ (as illustrated in Fig. 4.2 b)) with respect to different evolution

---

[3] Taken verbatim from the manuscript Geier et al. [172] with minor adaptions for the ease of readability.

times t_1 ranging from 0.1 μs to 3 μs. Additionally, we increase the initial Rydberg excitation time, resulting in denser samples with closer atom-to-atom separations and consequently leading to stronger median interactions J_m.

The median interaction strength J_m is estimated by simulating the spin distribution from a hard-spheres excitation model, where each Rydberg excitation is described by a superatom with a given blockade radius and effective Rabi frequency [171]. We note that the excitation model is less accurate for high densities, where the distance between Rydberg atoms is on the order of the blockade radius and the hard-sphere approximation breaks down. However, in order to efficiently perform time-reversal experiments, we prepared rather dense samples with strong interactions, such that the interaction timescales are short compared to decoherence times. The obtained spin distribution serves as an estimate of the typical interaction strengths.

For all interactions, the experimental data shows a decrease in the reversed magnetization with time (see circles in Fig. 4.3 a)), similar to Loschmidt echos with imperfections [173]. For the weakest interactions $J_\mathrm{m}/2\pi = 0.43$ MHz, shown as blue circles, the magnetization still returns to a value of $M \sim 0.2$, even after $t_\mathrm{rev} = 6$ μs. To put that into perspective: The magnetization relaxes to zero after only $t_1 \sim 0.7$ μs for this setup. We observe similar behavior for stronger interactions $J_\mathrm{m}/2\pi = 0.79$ MHz (yellow circles) and $J_\mathrm{m}/2\pi = 0.95$ MHz (green circles) despite the enhanced decrease of the overall reversed magnetization as a function of reversal time.

In an ideal reversal scenario, one would anticipate a complete return to the initial magnetization at all times. To understand which perturbations influence our time reversal process, we employ simulations of a simplified model that only considers two internal states, $|\downarrow\rangle$ and $|\uparrow\rangle$, per spin. The state transfer pulses are mimicked by a simple 2π rotation about the y-axis at the end of the first evolution time [4].

---

[4] We chose the y-axis since it does not respect symmetries of the Hamiltonian or the initial state, which the state transfer pulses in the experiment also do not respect.

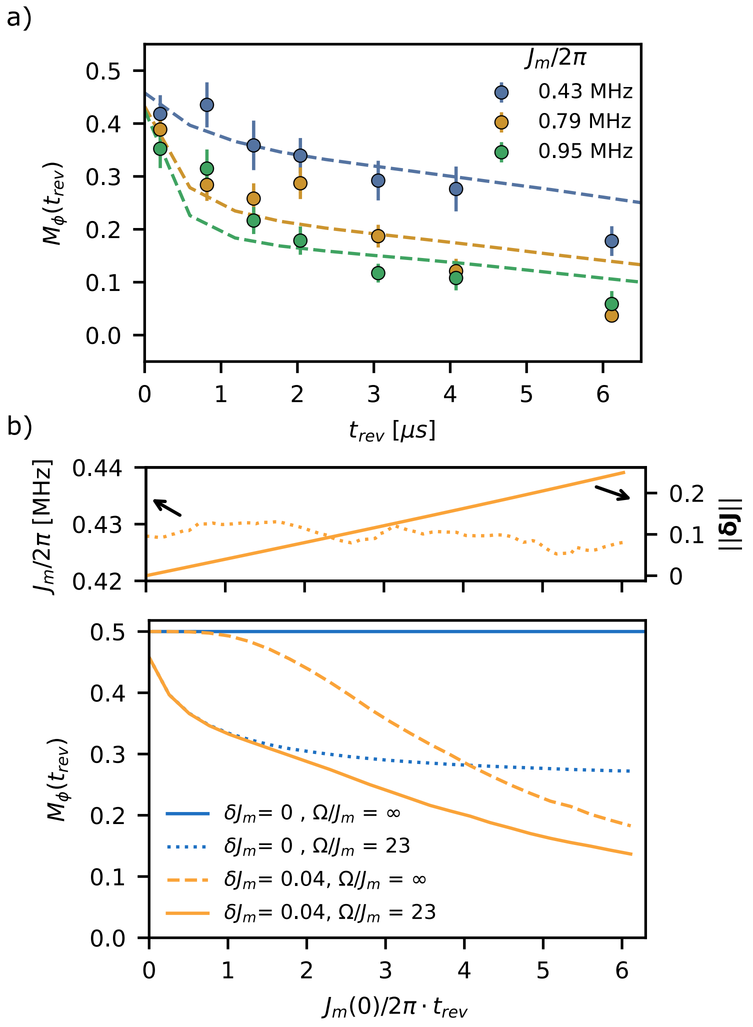

Figure 4.3: Reversal efficiency. a) The reversed magnetization measured at the time of the reversal $t_{\mathrm{rev}} = t_1 + k \cdot t_1$ for various evolution times t_1 (circles). The different colors correspond to increasing median interaction strength $J_{\mathrm{m}}/2\pi$ blue, yellow, and green, respectively. Dashed lines correspond to MACE simulation with a cluster size of 16 atoms. **b)** MACE simulations of the reversed magnetization for $J_{\mathrm{m}}(0)/2\pi = 0.43$ MHz including different experimental imperfections: No atom motion but finite state transfer pulse width (dotted blue line); atom motion but infinitely fast state transfer (dashed orange line); Atom motion and finite transfer pulse width (solid orange line). The blue solid line shows the situation for perfect reversal with infinitely fast transfer and no atom motion. The upper panel displays the change of the median interaction strength J_{m} (dotted orange line) and the distance of the interaction matrix norm of $||\delta\mathbf{J}||$ (solid orange line) (see main text for details). Figure and caption taken and adapted from the manuscript Geier et al. [172].

The system, comprising hundreds of spins, is too large to solve exactly. Therefore, we perform moving-average cluster-expansion (MACE) simulations [174]. This approach involves simulating clusters, each comprising n atoms, and then averaging the results across all possible cluster configurations present in our sample [5].

In the experiment, we restrict the experimental time to a maximum of 6 μs, which is shorter than to the spontaneous lifetime of the involved Rydberg state (527 μs for $|61P\rangle$ and 243 μs for $|61S\rangle$), as well as shorter compared to the combined lifetime, including black-body decay (143 μs for $|61P\rangle$ and 105 μs for $|61S\rangle$). Consequently, experimental timescales are more than an order of magnitude shorter than the lifetimes of the included Rydberg states, allowing to neglect these perturbations in our simulations. Instead, we account for two experimental perturbations that could significantly affect the system. First, the state transfer Rabi frequencies of $\Omega/2\pi \sim$ 10 MHz are only one order of magnitude stronger than the median interaction strength in the sample. We note that the maximum interaction strength for particles at the blockade radius can be much larger than J_{m}. Therefore, interactions lead to a modification of the state during the transfer pulses. Second, we account for the thermal motion of the atoms during the two evolution periods, which slightly changes the Hamiltonian over time, making a simple sign flip insufficient for perfect dynamics reversal. To model this, we assign each atom a fixed velocity v drawn from a Boltzmann distribution at the cloud's temperature $T = 11$ μK and recomputing the couplings every 200 ns according to the changing positions over the course of the simulation, given by $r_{ij}(t) = (x_i + v_i t) - (x_j + v_j t)$. We purely assume classical thermal motion and neglected motion due to forces between the atoms. This is justified by estimating both effects: The distance an atom travels due to the finite cloud temperature is given by $\Delta x = v \cdot t$ with $v = \sqrt{\frac{2k_BT}{m}}$. Therefore, over 1 μs the atom moved by roughly $\sim$ 50 nm. Motion due to atomic forces can be estimated by $\Delta x = a \cdot t^2$ with $a = F/m = \frac{1}{4\pi\epsilon_0}\frac{3d^2}{r^4}/m$. Here, d is the dipole matrix element. Over 1 μs, the atom moved roughly $\sim$ 0.5 nm. Simulations of this simpli-

---

[5] MACE simulations have been conducted by Adrian Braemer with close discussion.

fied model are shown as dashed lines in Fig. 4.3 a), and they capture the decrease in reversed magnetization on a qualitative level. We note, that the cluster sizes of $n = 16$ atoms are still not providing fully converged simulations and therefore our simulation results overestimate the magnetization systematically. A detail analysis has been performed by Adrian Braemer and is discussed in [172]. However, this slow convergence in cluster size is attributed to the high sensitivity of Loschmidt echos.

Our simulation allows us to isolate the influence of atomic motion and finite transfer efficiency so that we can assess the effects individually. When focusing on temperature, we study the change in couplings J_{ij} induced by thermal motion. On the one hand, we find the median interaction strength between nearest neighbors J_m does not vary significantly over the duration of the simulation (dotted orange line in the upper panel of Fig. 4.3 b)). This means that the overall distribution of couplings largely remains the same. On the other hand, when we directly compute the distance of the full interaction matrix $\mathbf{J}$ at the beginning and at time t as $\|\delta\mathbf{J}\| = \frac{\|\mathbf{J(t)}-\mathbf{J(0)}\|_F}{\|\mathbf{J(t)}\|_F}$ (where $\|\cdot\|_F$ denotes the Frobenius norm), we observe a noticeable growing deviation, with approximately 20% difference at 6 interaction cycles (solid orange line in the upper panel of Fig. 4.3 b)). We denote the change in couplings over one interaction cycle as $\delta J_\mathrm{m} = \|\delta\mathbf{J}(t = 2\pi/J_\mathrm{m})\|$.

While the global properties of the coupling distribution remain unchanged, the microscopic configuration does indeed undergo significant changes. The impact on the magnetization can be directly observed by the dashed orange line in the lower panel of Fig. 4.3 b), representing the scenario with perfect transfer efficiency $\Omega/J_\mathrm{m} = \infty$ and our finite cloud temperature ($\delta J_\mathrm{m} = 0.04$). The reversed magnetization starts at 0.5 and, after an initial plateau, gradually decreases over time after a few interaction cycles. This behavior is due to the sensitivity of the Loschmidt echo to different microscopic configurations. The atomic motion clearly affects the long-term behavior of our time reversal protocol but cannot explain the drop in reversed magnetization at short times.

We exclusively investigate the impact of finite state transfer efficiency in a scenario where the sample is at absolute zero temperature ($\delta J_{\mathrm{m}} = 0$). In this case, couplings remain constant in time, but interactions are active during the transfer process (dotted blue line in Fig. 4.3 b) lower). As expected, this reduces the transfer efficiency even at $t = 0$, where no dynamics take place except during the transfer pulse. Surprisingly, the magnetization quickly reaches a plateau and does not appear to decay further. Fortunately, this means finite pulse times introduce an almost constant error in the magnetization that can be calibrated.

By considering both imperfections, we can qualitatively reproduce the results observed in the experiment (orange solid line). We conclude that for short times ($J_{\mathrm{m}}/2\pi \cdot t_{\mathrm{rev}} < 1$), finite transfer efficiency is the dominating perturbation, while the longer-term behavior ($J_{\mathrm{m}}/2\pi \cdot t_{\mathrm{rev}} > 1$) is dominated by the sensitivity to slight changes in the microscopic configuration, due to atomic motion.

Summary of the experimental parameter

Our investigation of the performance includes tuning the median interaction strength by increasing the Rydberg excitation time, denoted as t_{exc}. A change of the excitation time affects the spin distribution in several ways. Longer excitation times increase the atom number N within a certain volume and therefore reduce the median separation between the atoms, denoted as r_{med}. On the other hand, longer excitation times result in a smaller fourier width, which in turn increases the blockade radius (see Appendix A).

The following table summarizes the parameters obtained from our excitation model:

	$J_{\mathrm{m}}/2\pi$ [MHz]	$r_{\mathrm{med}}[\mu m]$	$r_b[\mu m]$	$t_{exc}[\ \mu s]$	N
	0.43	14.3	8.1	0.8	332
	0.79	11.7	9	1.55	917
	0.95	11.1	9.6	2.55	1333

4.4 Time-reversal of tunable XXZ models[6]

For quantum engineering applications, it is important to be able to tune the specific type of Hamiltonian one is interested in studying. Quantum metrology applications benefit from a power-law XXZ Hamiltonian [175], which can directly be combined with time-reversal protocols to enhance phase sensitivity [161, 162]. On the other hand, investigating out-of-time-order correlators as a measure for quantum information scrambling, might reveal distinct behavior for different types of spin models [157].

To realize the reversal of a wide range of many-body Hamiltonians, we combine our protocol with Floquet engineering. This technique, introduced in Chap. 3 and employed in various other quantum simulators to engineer tunable spin Hamiltonians [33, 155], utilizes a periodically applied drive to transform a naturally given Hamiltonian into a desired target form. In our implementation, the specific pulse sequence illustrated in Fig. 4.4 a) transforms the natural XX Hamiltonian into an XXZ Hamiltonian

$$H_{\mathrm{XXZ}} = \sum_{i,j} J_{ij}^{\perp}(S_x^i S_x^j + S_y^i S_y^j) + J_{ij}^{\parallel} S_z^i S_z^j \quad , \tag{4.5}$$

with $J_{ij}^{\perp} = J_{ij}\frac{2(\tau_1+\tau)}{t_c}$ and $J_{ij}^{\parallel} = J_{ij}\frac{2\tau}{t_c}$. Here, $t_c = 2(\tau_1 + 2\tau)$ is the total sequence time and $\tau_2 = \tau_3 = \tau$. The anisotropy $J_{ij}^{\parallel}/J_{ij}^{\perp}$ is tunable with the delay time between the pulses. A detailed derivation of this Hamiltonian is performed in Chap. 3.

To demonstrate the reversal, we employ a protocol similar to the one introduced in Sec. 3.4. We initialize the system in a state in the equatorial plane of the spin system represented the first spin encoding and let it evolve for $t_{\mathrm{prep}} = 100$ ns. The resulting state serves as the initial state with M ~ 0.4 magnetization. We introduce this step to allow the strongest interacting spins in the disordered sample to demagnetize since their interaction cannot be efficiently engineered (see Chap. 3). We

---

[6] Taken verbatim from the manuscript Geier et al. [172] with minor adaptions for the ease of readability.

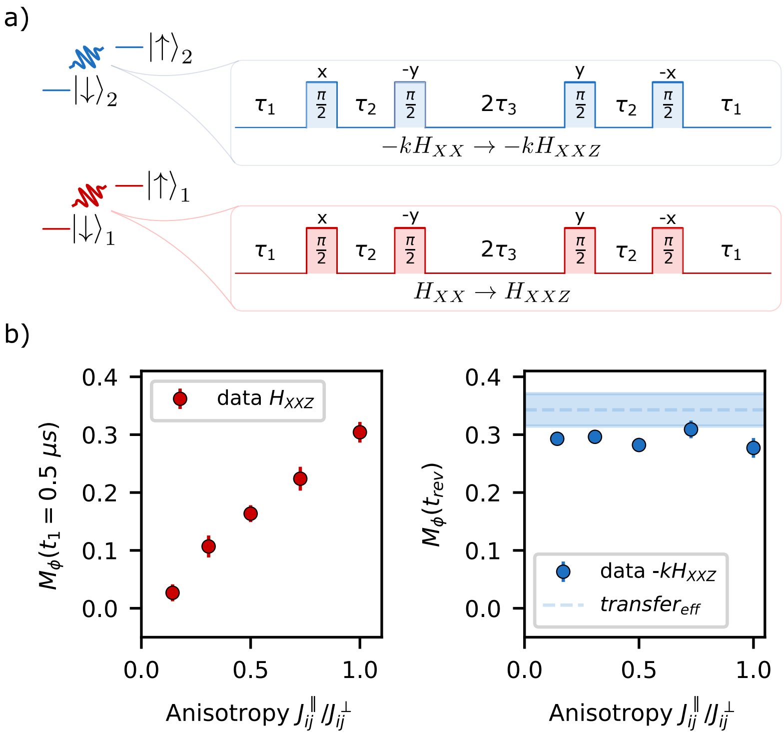

Figure 4.4: Time-reversal of XXZ models with tunable anisotropy. a) Protocol: The periodic driving sequence consisting of $\pi/2$ pulses with tunable delay times is applied to the two systems and transforms the natural XX Hamiltonian into an XXZ Hamiltonian with the respective sign. **b)** Red circles in the left panel: Magnetization at $t_1 = 0.5$ μs as a function of the anisotropy $J_{ij}^{\parallel}/J_{ij}^{\perp}$ in the engineered XXZ Hamiltonian without state transfer (for the first spin encoding). Blue points in the right panel: Magnetization at the reversal time t_{rev} (for $t_1 = 0.5$ μs) after evolving with the same pulse sequence and therefore target Hamiltonian in both spin encoding states, despite the opposite sign. Figure and caption taken and adapted from the manuscript Geier et al. [172].

then apply the pulse sequence and engineer an XXZ Hamiltonian with anisotropies $J_{ij}^{\|}/J_{ij}^{\perp}$ between 0.14 and 1 and measure the magnetization at late times $t_1 = 0.5\ \mu s$. For $J_{ij}^{\|}/J_{ij}^{\perp} = 1$, the system posses a $SU(2)$ symmetry, and the magnetization constitutes a conserved quantity. However, when $J_{ij}^{\|}/J_{ij}^{\perp} < 1$, we expect the magnetization to decrease due to the breaking of this symmetry. The red circles in the first panel of Fig. 4.4 b) show the magnetization at $t_1 = 0.5\ \mu$s as a function of the anisotropy in the system with the first spin encoding. As already observed in Sec. 3.4, the magnetization increases for increasing $J_{ij}^{\|}/J_{ij}^{\perp}$, and we almost completely conserve the initial magnetization ($M \sim 0.4$) when $J_{ij}^{\|}/J_{ij}^{\perp} = 1$.

After evolving in the first spin state encoding, we transfer the state to the second set of encoding states to flip the sign of the natural Hamiltonian. Applying the very same engineering sequence as in the first half then realizes $-kH_{\mathrm{XXZ}}$ without any other operations necessary. We measure the final magnetization at t_{rev}, where we expect the revival. The result is shown by the blue points in the second panel of Fig. 4.4 b). For all probed anisotropies, the reversed magnetization reaches the magnetization expected from the state transfer efficiency, demonstrating the ability to reverse the dynamics for arbitrary XXZ Hamiltonians.

4.5 Summary and discussion

Summary

In this chapter, we introduced and experimentally validated a protocol for reversing the dynamics of strongly interacting spin systems. The approach is based on identifying two subspaces in the Hilbert space, which is spanned by a larger number of Rydberg states, encoding the same spin Hamiltonian but with an opposite sign. These subspaces, denoted as one and two, naturally interact through a dipolar XX model with the respective coupling parameters bearing opposite signs. A coherent state transfer between the spin encodings is realized by employing two consecutive global microwave π pulses.

In the first experimental demonstration, the system was initialized in a fully magnetized state. We then observed the relaxation of magnetization in the first spin-encoding subspace, driven by unitary dynamics governed by the XX Hamiltonian. As the initial state partially demagnetized, we implemented the transfer into the second spin-encoding subspace, resulting in an almost complete revival of magnetization attributed to the opposite interaction sign. For longer times, the magnetization started to relax again, and the system ended up in a fully demagnetized state.

To investigate the sensitivity of our protocol, we examined the performance of our current implementation. We realized this by adjusting the density of the Rydberg sample, thereby varying the spacing between atoms and the strength of their interactions. We introduced a simplified model that allows us to identify two main perturbations: (i) Imperfect transfer pulses, stemming from strong interactions, leading to an offset in the magnetization, affecting the early times, and (ii) motion of the atoms due a finite cloud temperature, which changes the micro configuration of the sample over time, affecting the long-term behavior.

We finally combined our approach to reverse the time evolution of many-body quantum systems with the ability to realize tunable spin Hamiltonian through Floquet engineering, as discussed in the previous Chap. 3. By periodically driving subspace one, we observed the evolution of the magnetization at long times for different anisotropies of an XXZ Hamiltonian. Subsequently, we transferred the state into the second spin-encoding subspace and applied the same periodic driving, targeting the XXZ Hamiltonian with same anisotropies but opposite sign. Notably, at the revival time, the magnetization remained constant, independent of the anisotropy, illustrating the time-reversal property for tunable spin Hamiltonians.

Discussion

While it is mathematically straightforward to comprehend that altering the sign of an interaction Hamiltonian effectively inverts the arrow of time, the consequences on the dynamics are profound. The fact that a demagnetized states essentially "decays" back into a magnetized state under natural interactions showcase the remarkable characteristics inherent in the unitary evolution of quantum systems.

Time-reversal has previously been implemented on platforms which mostly realize collective models [161–163, 166]. Nuclear magnetic resonance experiments have demonstrates the reversal of dynamics for power-law interactions with mixed quantum states by Floquet engineering the natural Hamiltonian [160, 165, 167], any approach which will be further discussed in the Chap. 5. The application to systems featuring power-law interactions in an isolated environment with pure quantum states has, to our knowledge not been realized before. The protocol simply requires the application of a state transfer, making the experimental implementation quite simple and robust. Both effects that are currently affecting the performance of the protocol, being the finite transfer efficiency and atomic motion, are not fundamental and can be reduced by increasing the Rabi frequency and lowering the cloud temperature. We also note that the approach is applicable to general experimental platforms featuring two subspaces for the pseudo-spin encoding with interaction coefficient of opposite sign.

Our implementation in isolated systems with power-law interactions lays the foundation for several directions of application in quantum technologies. It facilitates the investigation of out-of-time-order correlators [166–168] for various Hamiltonians and it might be applied in quantum-enhanced metrology to achieve phase sensitivity close to the Heisenberg limit [162, 164]. Time reversal operations further constitute an important tool to validate the quality of general platforms that are exploiting quantum effects as a resource, by identifying perturbations resulting in an imperfect revival of observables [134, 165].

CHAPTER 5

Two proposals for alternative approaches to engineer quantum spin systems

In the previous chapters 1 to 4 of this thesis, we conducted experimental investigations to explore how Rydberg atoms serve as a versatile platform for studying quantum many-body systems. We employed several approaches, including carefully selected principle quantum numbers, various state combinations, or periodic driving sequences, to shape the interaction Hamiltonian. In this final chapter, we propose two alternative approaches to engineer the Hamiltonian, laying the foundation to study a wide variety of quantum spin models with additional features.

This chapter is divided into two independent parts, each proposing an own experiment and structured as follows:

- **Section 5.1:** The first part investigates an alternative approach to reversing the time evolution of a quantum spin system. We employ well-established nuclear magnetic resonance techniques and integrate them into the Rydberg platform. In order to achieve this, we propose the tuning of dipolar XXZ models with a static electric field as an experimental method, which makes up a major part of this section.

- **Section 5.2:** In the second part of this chapter, we propose a scheme for tweezer array experiments, allowing the combination of spin-1/2 systems with mobile dopants. The system can be mapped on a so-called bosonic $t-J$ model, and our proposed implementation includes a third Rydberg level, effectively realizing a *hole* degree of freedom. In this model, various parameters are tunable with a new set of experimental knobs: the applied magnetic field and the angle between the atoms and the quantization axis.

5.1 Time-reversal through Floquet engineering in a static electric field

In Chap. 4, we introduced and experimentally demonstrated a protocol for reversing the dynamics of many-body spin systems featuring strong interactions. This approach was based on the identification of two subspaces within the large Hilbert space of the Rydberg manifold. These subspaces encode the same spin Hamiltonian but with opposite signs.

In this section, we propose a novel protocol to reverse the sign of a many-body Hamiltonian on the Rydberg platform. It is purely based on Floquet engineering and works without transferring the state. The approach is based on the periodic driving techniques introduced in Chap. 3. However, instead of engineering arbitrary spin models, we employ multi-pulse sequences to specifically target a negative sign in the interaction Hamiltonian. Reversing time through Floquet engineering has found applications in nuclear magnetic resonance (NMR), and established protocols with applications in quantum simulation already exist. An example is illustrated in Wei *et al.* [167]: By simply adjusting the delay times of pulses, this approach has enabled the engineering of disorder and interactions in NMR samples, offering access to a wide range of regimes, ranging from integrable and single-particle-models to models that show signatures of localization. Applying these established NMR techniques to the Rydberg platform, enabling control in an isolated environment, facilitates the quantum simulation of many-body spin systems. However, the existing pulse sequences are tailored for a specific dipolar Hamiltonian naturally occurring in NMR samples. In the following sections, we propose an approach for implementing this Hamiltonian with Rydberg atoms and numerically study the reversal through Floquet engineering in an experimentally realistic scenario.

The central part of our proposal lies in the engineering of dipole-dipole interactions with a static electric field. This allows for the realization of an Ising term in the Hamiltonian, which is necessary to perform our driving protocol, as will be discussed throughout this section.

In Sec. 5.1.1, we outline the requirements for manipulating the sign of the interaction Hamiltonian using Floquet engineering. We then discuss how a static electric field changes the interaction Hamiltonian of Rydberg spin systems and propose an explicit experimental implementation in Sec. 5.1.2. To validate our proposal, we conduct numerical simulation on a 1D chain in Sec. 5.1.3, before discussing experimental challenges in Sec. 5.1.4.

5.1.1 Time-reversal through Floquet engineering

In this section, we introduce the concept of using periodic driving to invert the sign of a many-body Hamiltonian and examine the necessary conditions for its application. The calculations rely on average Hamiltonian theory, which was introduced in Sec. 3.1. It is important to note that we only consider global spin manipulations, which impose certain constraints on the realizable Hamiltonians. To understand the constraints, it is convenient to translate global microwave rotations, as presented in Chap. 3, into rotations on the interaction matrix. For a system comprising two spins, the most general XYZ Hamiltonian can be expressed as

$$\hat{H} = J_x \hat{S}_x^1 \hat{S}_x^2 + J_y \hat{S}_y^1 \hat{S}_y^2 + J_z \hat{S}_z^1 \hat{S}_z^2 = \hat{S}_1 \mathbf{J} \hat{S}_2^T \quad . \tag{5.1}$$

Here, $\mathbf{J} = \mathrm{diag}(J_x, J_y, J_z)$ is the interaction matrix and $\hat{S}_{1,2} = (\hat{S}_x^{1,2}, \hat{S}_y^{1,2}, \hat{S}_z^{1,2})$. When we apply $\pi/2$ rotations to this matrix, we essentially permute the entries. For instance, a $\pi/2$ pulse along the x-direction swaps the J_y and J_z components, resulting in a modified interaction matrix denoted as $\mathbf{J}' = \mathrm{diag}(J_x, J_z, J_y)$. It is important to note that *global* rotations, as employed in this context, do not affect the trace of the interaction matrix. Therefore, time reversal through Floquet engineering is only achievable with Hamiltonians that possess traceless interaction matrices, i.e., $\mathrm{Tr}(\mathbf{J}) = 0$, allowing the transformation $\mathbf{J} \to -\mathbf{J}$. Systems described by an XX Hamiltonian have $\mathbf{J} \propto \mathrm{diag}(1, 1, 0)$ and it is therefore not possible to reverse the sign of $\mathbf{J}$ using Floquet engineering. To realize time reversal, one must select an interaction matrix like $\mathbf{J} \propto \mathrm{diag}(-1, -1, 2)$. Under the application of global rotations, it possible to permute the entries such that we end up with a interaction matrix denoted as $\mathbf{J}' \propto \mathrm{diag}(1, 1, -2)$. This reversed matrix has the same trace as $\mathbf{J}$. Consequently, the experimental objective is to realize an XXZ Hamiltonian with specific interaction parameter: $J_x = J_y = -1$ and $J_z = 2$. The subsequent section proposes a scheme to achieve this using dipolar interacting spins in a static electric field. Detailed discussions regarding the periodic driving sequences employed to realize the reversal are presented in Sec. 5.1.3

5.1.2 Tuning of the interaction Hamiltonian with an electric field

In this section, we present a robust experimental protocol for engineering an XXZ Hamiltonian, utilizing a static electric field. We specifically employ this method to determine parameters that yield an XXZ Hamiltonian characterized by a traceless interaction matrix, suitable to implement time reversal through Floquet engineering.

We consider the case of two interacting Rydberg atoms for the rest of this chapter. The result can readily be extended to a many-body system consisting of individual Rydberg atoms. As introduced in Sec. 2.1, two Rydberg states, $|\downarrow\rangle = |nS\rangle$ and $|\uparrow\rangle = |nP\rangle$, can be mapped on the Heisenberg XX Hamiltonian:

$$\hat{H} = J^{\perp}(\hat{S}_x^1 \hat{S}_x^2 + \hat{S}_y^1 \hat{S}_y^2) \tag{5.2}$$

The coupling term is calculated using the dipolar interaction Hamiltonian $\hat{H}_{\mathrm{DDI}}$

(2.13) of the atomic system and is given by

$$J^{\perp} = \langle\downarrow_1\uparrow_2|\hat{H}_{\mathrm{DDI}}|\uparrow_1\downarrow_2\rangle \quad . \tag{5.3}$$

Most importantly, this Hamiltonian does not feature Ising-like interactions $\propto J^{\parallel}\hat{S}_z^1\hat{S}_z^2$. This can be seen from the form of the Ising term, which is given by (see Sec. 2.1):

$$J^{\parallel} = (E_{\uparrow_1\uparrow_2} + E_{\downarrow_1\downarrow_2}) - (E_{\downarrow_1\uparrow_2} + E_{\uparrow_1\downarrow_2}) \tag{5.4}$$

with $E_{\alpha_1\beta_2} = \langle\alpha_1\beta_2|\hat{H}_{\mathrm{DDI}}|\alpha_1\beta_2\rangle$. For state configurations $|\downarrow\rangle = |nS\rangle$ and $|\uparrow\rangle = |nP\rangle$ energy shifts $E_{\alpha_1\beta_2}$ are dipole-forbidden and $J^{\parallel}$ vanishes.

The situation changes in the presence of a static electric field, which modifies the eigenstate structure of the system. An additional Hamiltonian accounts for the interaction with this electric field and is expressed as $\hat{H} = -\hat{d} \cdot E$. In the case of weak fields, this term can be treated perturbatively, leading to energy shifts in the bare atomic states. However, for strong fields, the electric field significantly couples surrounding Rydberg states, such that perturbation theory breaks down, and one must diagonalize the entire Hamiltonian to accurately describe the system.

The diagonalization of the Hamiltonian leads to the emergence of new eigenstates, which depend on the specific strength of the applied field. These novel eigenstates can be represented as combinations or superpositions of the bare atomic states in the absence of the field:

$$|\psi(E)\rangle = \sum_{n,L,J,m_j}^{\text{barestates}} c_{n,L,J,m_j}(E)\,|nL_J, m_j\rangle \quad . \tag{5.5}$$

Here, $c_{n,L,J,m_j}(E)$ is the electric field dependent probability amplitude of the bare state with quantum numbers n, L, J, m_j in the new eigenstate $|\psi(E)\rangle$.

We now consider two eigenstates within a constant electric field: $|\downarrow\rangle = |\psi(E)\rangle_1$ and $|\uparrow\rangle = |\psi(E)\rangle_2$. Here, we immediately notice that the energy shifts for $J^{\parallel}$ in Eq. 5.4 are no longer zero, as $|\psi(E)\rangle_{1/2}$ contain different angular momentum states, and not all matrix elements are dipolar-forbidden (once again, we consider direct dipolar interactions $\hat{H}_{\mathrm{DDI}}$ (2.3)). Consequently, the application of a static electric

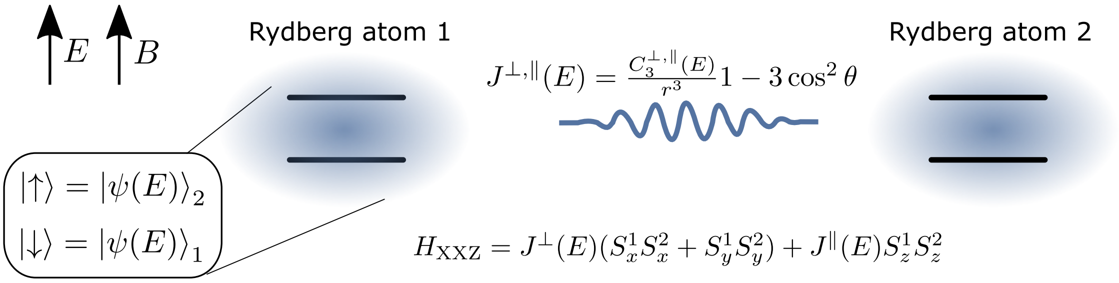

Figure 5.1: Rydberg interactions in an static electric field. The spin states are encoded in two eigenstates in the electric field $|\downarrow\rangle = |\psi(E)\rangle_1$ and $|\uparrow\rangle = |\psi(E)\rangle_2$. With this encoding, two atoms (represented by the blue circles) interact via exchange but also Ising interactions that are tunable with electric field value.

field permits the engineering of Ising interaction terms $J^{\parallel}$ within dipolar Rydberg systems.

We proceed to derive the explicit form of the resulting interaction Hamiltonian. In the following analysis, we exclusively consider electric fields aligned along the quantization axis. With this restriction, the electric field couples states with $\Delta m_j = 0$. Consequently, the new eigenstates presented in Eq. 5.5 are superpositions of bare states that share the same m_j. Fig. 5.1 illustrates this scenario. As the interactions are not changing the total magnetic quantum number, the angle dependence in the dipolar coupling coefficients for exchange and Ising term is given by $1 - 3\cos^2\theta$, as derived in Sec. 2.1. The full XXZ Hamiltonian reads:

$$\hat{H}_{\mathrm{XXZ}} = J^{\perp}(E)\left(S_x^1 S_x^2 + S_y^1 S_y^2\right) + J^{\parallel}(E) S_z^1 S_z^2 \quad , \tag{5.6}$$

with interaction parameter $J^{\perp,\parallel}(E) = \frac{C_3^{\perp,\parallel}(E)}{r^3}\left(1 - 3\cos^2\theta\right)$ which are now explicitly electric field dependent (see Eq. 5.4). Many experiments with exceptional electric field control could directly implement this protocol and engineer desired spin Hamiltonian [91].

In the following, this approach is applied to find Rydberg state combinations that realize an XXZ Hamiltonian with a traceless interaction matrix and, therefore, an anisotropy of $J^{\parallel}/J^{\perp} = -2$.

Starkmap calculations

Generally, numerous state combinations can realize XXZ Hamiltonians with a traceless interaction matrix. However, in order to efficiently perform experiments, we demand the combination to satisfy the following criteria:

- The state $|\downarrow\rangle = |\psi(E)\rangle_1$ should mainly consist of $|nS\rangle$ Rydberg states to enable its coupling and selective addressing through a two-photon excitation from the $|5S\rangle$ ground state.
- The state $|\uparrow\rangle = |\psi(E)\rangle_2$ should primarily contain $|nP\rangle$ Rydberg states to facilitate its coupling and manipulation via a microwave field. Additionally, states without significant $|nP\rangle$ contributions would result in relatively weak interaction parameters $J^{\perp,\parallel}$.

To identify states that meet these criteria, we conducted Starkmap calculations using the Alkali Rydberg Calculator (ARC) [176]. This involves the exact diagonalization of the Hamiltonian within a restricted Hilbert space, considering the conservation of the m_j quantum number. Specifically, we focused on eigenstates in the electric field that predominantly consist of $|48S_{1/2}, m_j = 1/2\rangle$ for $|\downarrow\rangle$ and $|48P_{1/2}, m_j = -1/2\rangle$ for $|\uparrow\rangle$. Stark map near each of these states is presented in Fig. 5.2 a) and b), respectively. These eigenstates undergo changes due to the presence of the electric field, and the color coding in panels a) and b) corresponds to the overlap with the original $|48S_{1/2}, m_j = 1/2\rangle$ and $|48P_{1/2}, m_j = -1/2\rangle$ states in the absence of the field. The two lower panels are a zoom into the stark map close to an electric field around 8 V/cm, a value chosen to realize a traceless XXZ Hamiltonian.

Parameter regime for a traceless interaction matrix

In the Starkmap displayed in Fig. 5.2, we consider an electric field range from 8.278 to 8.288 V/cm and extract the eigenstates with largest $|48S_{1/2}, m_j = 1/2\rangle$ and $|48P_{1/2}, m_j = -1/2\rangle$ components for $|\downarrow\rangle$ and $|\uparrow\rangle$, respectively. With these states, the

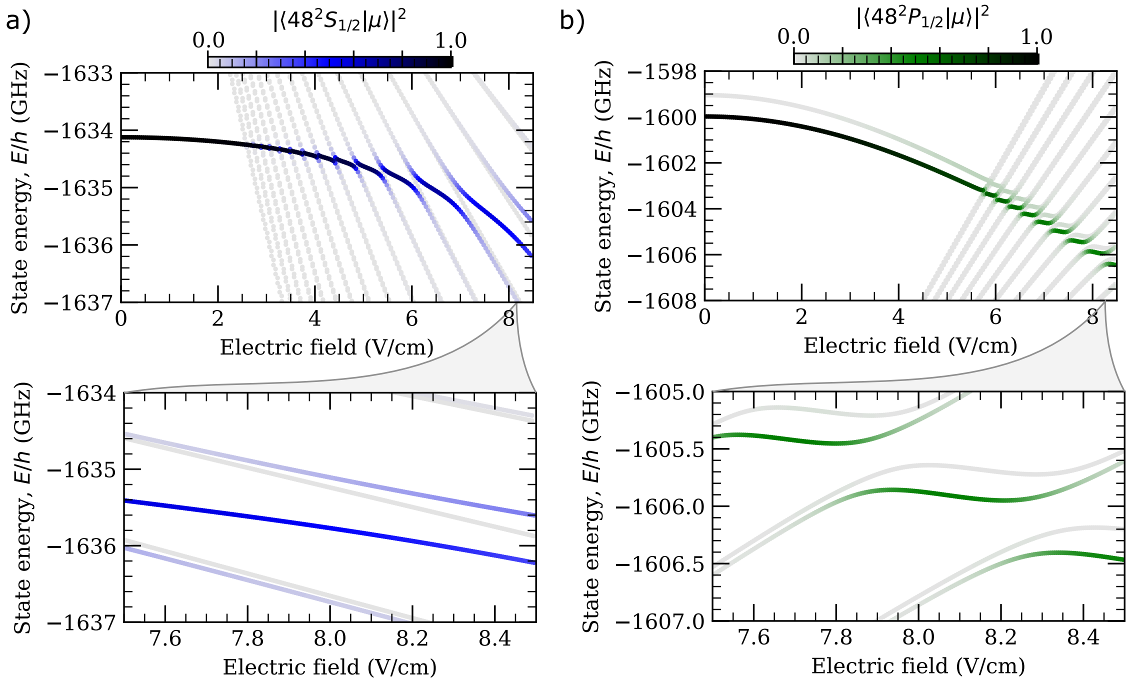

Figure 5.2: Starkmap calculations. a) Upper panel: Coarse Starkmap of rubidium 87. The lines display the ionization energy of the eigenstates in the electric field. Blue color bar display the overlap of $|48S_{1/2}, m_j = 1/2\rangle$ with the eigenstates. Lower panel: Detailed view in the range around 8 V/cm, used to calculate the experimental parameters. **b)** Upper panel: Coarse Starkmap with green color bar display the overlap of $|48P_{1/2}, m_j = -1/2\rangle$ with the eigenstates. Stark map calculations have been performed using the ARC package for Python [176].

matrix elements $J^{\parallel}$ (Eq. 5.4) and $J^{\perp}$ (Eq. 5.3) are calculated. Fig. 5.3 a) displays the resulting anisotropy $J^{\parallel}/J^{\perp}$ as a function of the electric field. At an electric field of $E = 8.283$ V/cm, the anisotropy reaches a value of -2, making the interaction matrix of the Hamiltonian traceless. Furthermore, due to our selection of states and their large overlap with the states in the absence of an electric field, we achieve a significant coupling between the two spin states, which is at the order of the bare state coupling (see Fig. 5.3 b)).

Hence, within the proposed parameter regime, it becomes feasible to implement an XXZ Hamiltonian that allows for changing the sign of the Hamiltonian through Floquet engineering. In the subsequent section, we briefly introduce an example of pulse sequences that realize the time reversal operations.

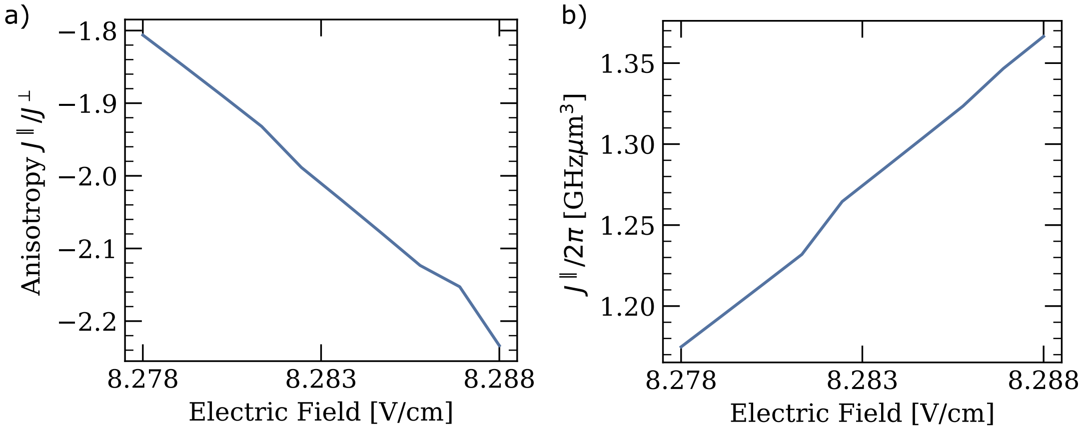

Figure 5.3: Interaction parameter in an electric field. a) Anisotropy $J^{\parallel}/J^{\perp}$ as a function of the electric field. See main text for the involved states. Time-reversal pulse sequences require an anisotropy value of -2. **b)** Interaction strength $J^{\parallel}/2\pi$ as function of the electric field for the anistropies of a).

5.1.3 Numerically testing Floquet time-reversal on a few atom system

In the previous section, we proposed a scheme to realize an XXZ Hamiltonian with Rydberg atoms for performing time reversal through Floquet engineering. The idea originates from NMR experiments, where XXZ Hamiltonian with traceless interaction matrix occur naturally. Moreover, it has been demonstrated that periodic driving can invert dynamics in these NMR systems [160,167]. In general, there exist numerous multi-pulse sequences capable of achieving this with various applications. For instance, in reference Wei *et al.* [167], a 16-pulse sequence was employed to intentionally introduce controllable disorder (using random on-site fields) and specific interactions into the system. This allowed for the exploration of integrable, single-particle, and localized regimes. With our proposed scheme, a similar experiment could be implemented with isolated quantum many-body systems of Rydberg atoms in tweezer arrays [43] with the additional capability of locally manipulating and reading out of the atoms.

While it would be interesting to study how these sophisticated pulse sequences perform on the Rydberg platform, our following investigations explore a first implementation of two basic sequences that are reversing the interaction term. The experimental configuration is sketched in Fig. 5.4 a). We consider 10 atoms in a 1D chain, separated by a lattice spacing of $a = 18$ μm. The Hamiltonian is given by $\hat{H}_{\text{XXZ}} = \sum_{i,j} J\left(-1S_x^i S_x^j - 1S_y^i S_y^j\right) + 2S_z^i S_z^j$, with $J/2\pi = 0.6$ GHzμm$^3/r^3$, taken from the previous parameter regime calculations. For a state polarized along the x-direction, Fig. 5.4 b) shows the simulated relaxation of the magnetization within 2 μs in the absence of driving using exact diagonalization. In order to reverse this relaxation dynamics, we focus on two sequences:

(i) The WAHUHA sequence (whh4), as introduced in Sec. 3.1, choosing the durations $\tau_1/2 = \tau_2 = \tau_3$. This pulse sequences transform $\hat{H}_{\text{XXZ}} \rightarrow -1/5\hat{H}_{\text{XXZ}}$.

(ii) The trev4 sequence [177] comprises two π pulses enclosed by two $\pi/2$ pulses. This sequence transforms $\hat{H}_{\text{XXZ}} \rightarrow -1/2\hat{H}_{\text{XXZ}}$.

Both pulse sequences are illustrated in Fig. 5.4 c). To assess the experimental feasibility of reversing the dynamics using these sequences, we apply the driving after the 2 μs of natural relaxation and measure the return fidelity, which quantifies the overlap of the reversed state with the initial state, after 4 μs (trev4) and 10

μs (whh4). In Chap. 3, we identified interactions during the pulses, as well as the fulfillment of the fast driving condition $J \cdot t_c \ll 2\pi$ (Eq. 3.10), as the main sources for imperfect engineering. Therefore, our simulation takes into account the finite pulse width and investigates the effect of a finite Rabi frequency. Additionally, we probed the fidelity as a function of the number of cycles n. The fidelity as a function of these two parameters is shown in Fig. 5.4 d),e). Under the whh4 sequence (Fig. 5.4 d)) the fidelity increases with the number of cycles for all Rabi frequencies of the $\pi/2$ pulse. We achieve return fidelities of approximately 0.9 for $n = 30$ cycles and $\Omega/2\pi \approx 100$ MHz Rabi frequencies. On the other hand, the fidelity for the trev4 sequence (Fig. 5.4 e)) exhibits a similar behavior but increases significantly faster than for whh4. Already at $n = 15$ cycles and $\Omega/2\pi \approx 100$ MHz, the fidelity surpasses 0.9. This behavior can be explained by the scaling of $-1/2$ for the reversed Hamiltonian, in comparison to $-1/5$, which requires longer cycling times t_c, thereby violating the fast driving condition. Consequently, for simply reversing the interaction Hamiltonian, the trev4 pulse sequence is preferable and effectively reverses the time evolution of a spin system in a realistic experimental scenario with high fidelity.

5.1.4 Experimental challenges

We have presented a scheme for realizing an XXZ Hamiltonian with tunable interaction parameter. While our focus has been on obtaining a traceless interaction matrix in our implementation, this protocol can be readily adapted for various quantum applications involving Rydberg atoms where tunable spin models are required [157, 167, 175].

However, it is important to note that several considerations must be taken into account for experimental implementation. Some of these considerations are discussed below:

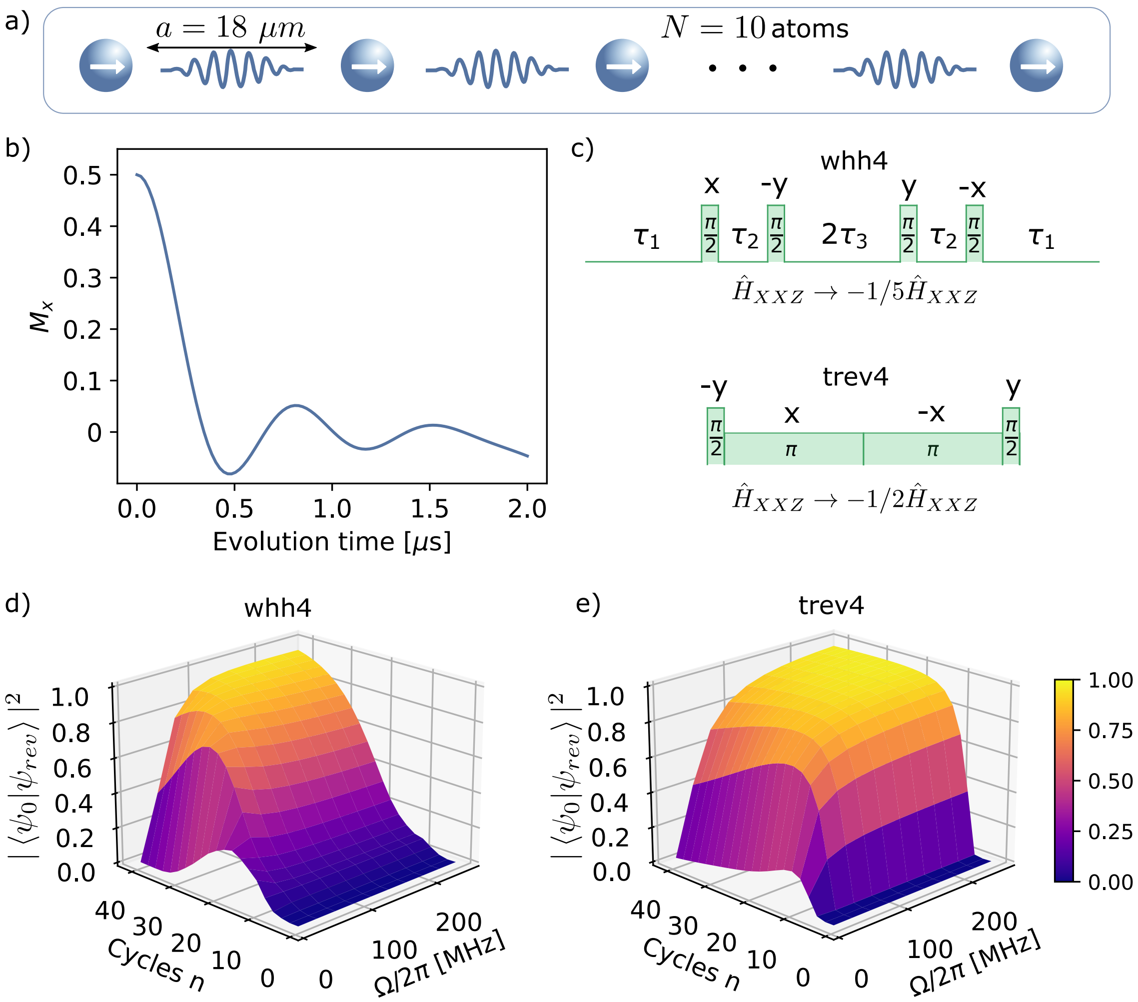

Figure 5.4: Floquet time-reversal on a few atoms system. **a)** System under consideration, consisting of 10 atoms in a 1D configuration with interactions governed by $\hat{H}_{\mathrm{XXZ}}$. **b)** Magnetization relaxation dynamics of the system initialized in a x polarized state $|\psi_0\rangle$, with $J/2\pi = 0.6$ GHzμm$^3/r^3$. **c)** Multi-pulse sequences used to transform $\hat{H}_{\mathrm{XXZ}} \to -1/5\hat{H}_{\mathrm{XXZ}}$ (whh4) and $\hat{H}_{\mathrm{XXZ}} \to -1/2\hat{H}_{\mathrm{XXZ}}$ (trev4). Return fidelity $|\langle\psi_0|\psi_{rev}\rangle|^2$ (z axis) as function as the number of cycles n and the drive Rabi frequencies $\Omega/2\pi$ for the whh4 (**d)**) and the trev4 (**e)**) sequence.

Stable electric field control In order to realize the desired XXZ Hamiltonian, the electric field needs to remain stable at approximately 1 mV/cm. Fluctuations exceeding this value can result in significant variations in the Hamiltonian. Commercially available amplifiers and sources can provide the required level of accuracy.

Microwave control The time-reversal protocol introduced in this section relies on the applications of global microwave pulses. To realize high fidelity microwave pulses, it is crucial to consider surrounding states that may also be coupled by the drive. In principle, these states can be tuned with the applied magnetic field and should be optimized accordingly. Additionally, the coupling to these states strongly depends on the specific bare states involved.

Rydberg state lifetime To efficiently perform experiments within the Rydberg manifold, the interactions must be much faster than the typical lifetime of the atoms. We have chosen eigenstates within the electric field that retain a significant portion of the original bare state while also including states with higher angular quantum numbers. The exact value needs to be calculated for each configuration.

5.1.5 Summary and discussion

Summary

In this section, we proposed a scheme to realize time-reversal operations through Floquet engineering. Due to symmetry considerations, the sign of an interaction Hamiltonian can only be changed by the use of only global pulses if the interaction matrix $\mathbf{J} = \mathrm{diag}(J_x, J_y, J_z)$ is traceless. To realize such a Hamiltonian, we outlined a method involving the application of a static electric field. The electric field modifies the eigenstates, adding an additional Ising interaction to the exchange term, which is already present in the absence of an electric field due to dipole-dipole interactions. Through Starkmap calculations, we identified experimental parameters and state combinations that yield an XXZ Hamiltonian with interaction matrix

$\mathbf{J} \propto \mathrm{diag}(-1,-1,2)$. Implementing this Hamiltonian is crucial for applying time-reversal pulse sequences. Additionally, we explored NMR pulse sequences designed to invert the sign of the interaction Hamiltonian and assessed their performance using a realistic 1D atom chain, which can be realized using Rydberg tweezer arrays. Finally, we discussed challenges associated with the experimental implementation of the proposed schemes.

Discussion

With the proposal presented in this section, Rydberg atoms can implement the dipolar spin Hamiltonian that naturally occurs in the secular approximation in NMR systems. This facilitates the application of well-established Floquet engineering techniques. While this section focused on sequences designed to reverse the dynamics of an interaction Hamiltonian, the next step would involve the investigation of more sophisticated sequences that also engineer other Hamiltonian terms, such as on-side disorder fields [167]. Spin models featuring disordered on-site fields are of particular interest as they serve as prototypical systems to study ergodicity breaking phenomena like many-body localization [99]. This represents an advantage compared to the approach presented in Chap. 4, which currently lacks the capability to reverse additional terms in the Hamiltonian, such as on-site fields (although it may be possible to design pulse sequences to achieve this).

While the primary focus has been on time-reversal operations, the ability to tune a dipolar XX model into arbitrary XXZ models through the application of a static electric field opens up various other possibilities. This is particularly significant considering the high level of control over electric fields realizable in Rydberg experiments [91] (see also Appendix B). In contrast to the XXZ model implementation discussed in Chap. 2, which exhibits a $1/r^6$ scaling of interactions, the approach presented in this chapter enables the realization of XXZ models with a common $1/r^3$ scaling.

5.2 Analog quantum simulation of doped XXZ models

So far, we presented how Rydberg atoms provide a versatile platform to study a wide range of tunable quantum spin-1/2 models by selecting the appropriate pseudo-spin-1/2 encoding in the Rydberg manifold and employing periodic driving. However, the Rydberg manifold inherently contains a vast number of states, enabling the realization of more general spin models, including three or more Rydberg states. In this final section, we propose an experimental protocol for introducing mobile dopants into spin models composed of Rydberg atoms, effectively realizing doped quantum magnets.

Generally, doped quantum magnets are a paradigmatic class of models believed to capture the phenomenology of strongly correlated electrons, such as high-T_c cuprate compounds. In these materials, superconductivity arises upon doping an antiferromagnetic Mott insulator [178] characterized by a competition between hole motion and magnetic ordering of spins [179]. Systems similar to strongly correlated electrons have been simulated using ultracold fermionic atoms in optical lattices, implementing the so-called Fermi-Hubbard model [23, 180–185]. These systems are highly isolated and, due to the development of quantum gas microscopy, allow for single particle readout using fluorescence imaging. Due to the superexchange mechanism in Hubbard models on a lattice at strong coupling, i.e. $U \gg t$, the underlying interactions are of antiferromagnetic nature in fermionic systems, while systems with bosonic atoms show ferromagnetic interactions [186].

This raises the question of how bosonic dopants behave in systems with antiferromagnetic interactions and whether they exhibit fundamental characteristics similar to their fermionic counterparts. Open questions in this field include the pairing mechanism or the phase diagram at low doping. The experimental studies in this area have remained elusive due to ferromagnetic interactions in Bose-Hubbard models, with only a few experiments implementing such a model [187, 188]. Given the numerous intriguing theoretical questions concerning the behavior of this model, we propose a feasible experimental realization of a doped XXZ quantum magnet using a Rydberg tweezer array. This approach will allow us to shed new light onto these questions. Specifically, we propose an experimental realization of the (hard-core) bosonic $t-J$ model [189]. The crucial aspect of our proposed implementation lies in its extensive range of tunable parameters, allowing access to various regimes. The key ingredient is to encode the hole degree of freedom in a third Rydberg state instead of actively removing an atom.

The ideas presented in this chapter emerged during a doctorate exchange with the group of Prof. Mikhail Lukin at the Department of Physics, Harvard University in the United States. The entire work constitutes a collaborative effort with discussions and important contributions from Lukas Homeier, Simon Hollerith and Neng-Chun Chiu. I performed the calculations presented in this section and contributed to the ideas on the implementation with Rydberg atoms. While this chapter exclusively focuses on how bosonic $t-J$ models can be mapped to three states in the Rydberg manifold, experimental details, such as potential ground state preparation schemes, are currently under investigations.

In section 5.2.1, we introduce the general concept of how bosonic $t-J$ models are implemented in Rydberg systems, with a particular emphasis on tweezer arrays. Section 5.2.2 details the implementation of the spin-spin interaction J, while section 5.2.3 focuses on the implementation of the spin-hole interactions t in our proposal. The calculations are performed for rubidium 87 atoms. Additionally, we explore how various parameters, such as magnetic field strength, the angle between atoms and the quantization axis, and the separation between atoms, can be employed to finely adjust a range of properties.

5.2.1 Brief introduction to bosonic $t-J$ models with Rydberg atoms

In this section, we provide a brief introduction to the Hamiltonian under consideration and the general idea of this proposal. The bosonic $t-J$ model consists of spin-1/2 models with preferably antiferromagnetic (AFM) interactions, and mobile bosonic holes. Recent investigations have introduced schemes to map the bosonic $t-J$ model onto pure spin systems of three Schwinger bosons [190], forming the basis of our proposed implementation. The Hilbert space is spanned by three states: $|h\rangle$ (hole state), $|\downarrow\rangle$ and $|\uparrow\rangle$ (the spin states), and the Hamiltonian reads:

$$\begin{aligned}\hat{H}_{t-\mathrm{J}} = &-\sum_{i,j,\sigma} t_{ij}\left(\hat{a}^{\dagger}_{i,\sigma}\hat{a}_{j,\sigma}+\hat{a}_{i,\sigma}\hat{a}^{\dagger}_{j,\sigma}\right)\\ &+\sum_{i,j} J^{\perp}_{ij}\left(\hat{S}^x_i\hat{S}^x_j+\hat{S}^y_i\hat{S}^y_j\right)+J^z_{ij}\hat{S}^z_i\hat{S}^z_j \quad .\end{aligned} \tag{5.7}$$

Here, $\hat{a}^{\dagger}_{i,\sigma}(\hat{a}_{i,\sigma})$ is the creation (annihilation) operator of a particle with spin $\sigma=\uparrow,\downarrow$ at site i. The first term describes the tunneling of particles $\propto t$, while the second term $\propto J^{\perp}, J^z$ describes magnetic XXZ interactions. Fig. 5.5 a) illustrates an example for a 1D chain in an AFM configuration with a single hole positioned on the central side. This scenario directly demonstrates how the mobility of holes, as they hop between sites, can frustrate magnetic order. It highlights the competitive nature of these processes, which has the potential to give rise to broad range of physical phenomena. In our proposal, a single atom is prepared in Rydberg states, with $|h\rangle$ corresponding to the hole in the $t-J$ model. It is therefore not a physical hole. The other atoms are prepared in the spin states $|\uparrow\rangle$ and $|\downarrow\rangle$. We emphasize that interactions in Rydberg systems have long-range character, enabling hopping and magnetic interactions beyond nearest neighbors.

The mapping to Rydberg atoms is illustrated in Fig. 5.5 b). As discussed in Chap. 2, spin-1/2 models with XXZ interactions can be implemented by encoding the spin in two Rydberg states possessing the same parity, such as $|nS\rangle=|\downarrow\rangle$ and $|(n+1)S\rangle=|\uparrow\rangle$. Interactions in this models are of second order, scaling with the distance as $1/r^6$, and are highly tunable by the principle quantum number n. This type of interactions implement the second term, $\propto J$, in the $t-J$ Hamiltonian of Eq. 5.7.

Moreover, we derived and experimentally observed in Chap. 3 that two atoms prepared in Rydberg $|nS\rangle$ and $|nP\rangle$ states exchange their states due to resonant dipole dipole interactions, which can be mapped on an XX model. We employ this type of $flip - flop$ interaction to implement the hole hopping t and, consequently, the first term in the $t - J$ Hamiltonian of Eq. 5.7. Those hopping interactions are direct dipolar exchange interactions and fall off as $\sim 1/r^3$.

In the next section, we outline the procedure for selecting the necessary parameters to experimentally construct the bosonic $t - J$ model for geometries in one and two dimensions. We begin by addressing the implementation of magnetic XXZ interactions with highly adjustable parameters, realized through the precise manipulation of magnetic fields and the angles between atoms and the quantization axis. Here, our primary focus lies in the practical realization of antiferromagnetic interactions. Finally, an experimentally realistic scenario is presented. The studies of this section is particularly interesting for Rydberg tweezer arrays, as they offer the potential to create arbitrary geometries, such as one-dimensional chains [43].

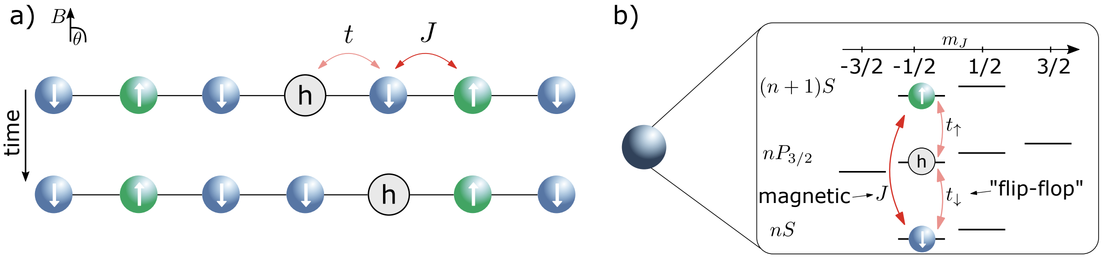

Figure 5.5: Experimental implementation of the $t - J$ Hamiltonian. a) A 1D spin chain in an antiferromagnetic configuration. Green and blue arrows illustrate the $|\uparrow\rangle$ and $|\downarrow\rangle$ states, while the hole is denoted $|h\rangle$. Hopping of the hole $\propto t$ frustrates magnetic order $\propto J(J^{\perp}, J^{\|})$. The angle between the chain and the quantization axis is denoted θ. **b)** Mapping of the $|\uparrow\rangle$, $|\downarrow\rangle$ (magnetic spin) and $|h\rangle$ (hole) degree of freedom to three states in the Rydberg manifold.

5.2.2 Tunable antiferromagnetic interactions

This section focuses on the implementation of tunable XXZ models, providing the magnetic interactions $\propto J^{\perp}, J^{\parallel}$, with a particular emphasis on realizing antiferromagnetic interactions ($J^{\parallel}, J^{\perp} > 0$). As discussed in Chap. 2, encoding the spin in two Rydberg states with the same parity, second-order van der Waals interaction give rise to XXZ Hamiltonians. To further elaborate on this method, we consider a spin encoding scheme in which $|nS\rangle = |{\downarrow}\rangle$ and $|(n+1)S\rangle = |{\uparrow}\rangle$. The interaction parameters associated with this scheme can be adjusted by varying the principal quantum number n, as has been illustrated in Fig. 2.3 a). However, we note that for n exceeding 40, the resulting interactions exhibit ferromagnetic (FM) characteristics $J^{\parallel} < 0$. Working at lower principal quantum number is undesirable due to the short Rydberg lifetime and weak interactions associated with such states. Therefore, additional tuning parameters are necessary to obtain a Hamiltonian with the desired AFM interactions [1]. To start our investigation, we revisit the van der Waals Hamiltonian, which enables the realization of magnetic interactions as discussed in Chap. 2, Eq. 2.15:

$$\hat{H}_{\mathrm{vdW}} = -\sum_{ij} \frac{\hat{H}_{\mathrm{DDI}}(\theta)\,|r_i r_j\rangle\,\langle r_i r_j|\,\hat{H}_{\mathrm{DDI}}(\theta)}{\Delta_F^{ij}(B)} \propto \frac{1}{r^6}\,. \tag{5.8}$$

It is evident that $\hat{H}_{\mathrm{vdW}}$ depends significantly on the Förster defect $\Delta_F^{ij}(B)$, which is related to the intermediate pair state energies. This dependence can be finely adjusted by applying a magnetic field B, shifting the pair state energies. Additionally, the dipole-dipole interaction Hamiltonian $\hat{H}_{\mathrm{DDI}}(\theta)$ couples pair states with distinct angular dependencies on θ, representing the angle between two atoms and the quantization axis (see Sec. 2.1 for details). The presence of potential Förster resonances adds complexity, making it nontrivial to determine a straightforward scaling for the interaction parameter.

---

[1] We note that an encoding $|nS\rangle = |{\downarrow}\rangle$ and $|(n+3)S\rangle = |{\uparrow}\rangle$ yields AFM interactions (see Fig. 2.3 b)). However, the intermediate $|(n+1)P\rangle$ only weakly couples to the spin states, which is unpractical to implement the hole hopping.

In the following discussion, we outline a procedure to realize the desired XXZ Hamiltonian within the Rydberg manifold. Specifically, we consider a scenario involving two Rydberg states $|68S_{1/2}, m_j = -1/2\rangle = |{\downarrow}\rangle$ and $|69S_{1/2}, m_j = -1/2\rangle = |{\uparrow}\rangle$.

Tuning XXZ interactions with a magnetic field in 1D

Our investigation begins with an examination of how the external magnetic field affects the van der Waals interactions, resulting in the XXZ Hamiltonian:

$$\hat{H}_J = \sum_{i<j} \Big(J_{ij}^{\perp}(B, \theta_{ij})(\hat{S}_x^i \hat{S}_x^j + \hat{S}_y^i\ \hat{S}_y^j) + J_{ij}^{\|}(B, \theta_{ij}) \hat{S}_z^i \hat{S}_z^j \Big) \quad . \tag{5.9}$$

The presence of a magnetic field directly influences the Förster defects Δ_F^{ij} within the van der Waals Hamiltonian, altering their strengths and potentially their signs. For relatively low magnetic fields, the Förster defects experience only slight relative modifications, resulting in minimal changes to $\hat{H}_{\mathrm{vdW}}$. The most significant effects are expected near Förster resonances, where different pair states within the intermediate $|68P_{3/2}\rangle$ manifold are individually tuned into and out of resonance. This sensitivity to specific pair states makes the magnetic field an ideal parameter for realizing antiferromagnetic interactions.

In the upper panel of Fig. 5.6 a), we illustrate the anisotropy $J^{\|}/J^{\perp}$ when the magnetic field is oriented perpendicular to the axis connecting two atoms ($\theta = \pi/2$). At low magnetic field strengths, a small negative anisotropy is observed, consistent with the earlier depiction in Fig. 2.3 a). However, as the magnetic field becomes larger than 100 G, the pair states undergo significant shifts, resulting in a substantial change in amplitude and sign of the anisotropy. The red shaded area corresponds to situations where intermediate pair states come into resonance, rendering perturbation theory inapplicable and $\hat{H}_{\mathrm{vdW}}$ an inadequate description (see the end of this section for a detailed discussion). Therefore, we can use the magnetic field as a tool to tune the anisotropy $J^{\perp}/J^{\|}$ of a XXZ Hamiltonian in a given spatial configuration with a fixed angle θ. For a specific magnetic field strength of

$B = 158$ G, we identify an anisotropy $J^{\parallel}/J^{\perp}$ that results in both exchange and Ising interactions being positive, effectively realizing antiferromagnetic interactions.

Applicability of van der Waals interactions Working close to Förster resonances can lead to resonant dipole interactions, as briefly discussed in Sec. 2.1. This situation is undesirable when aiming to implement a pure two-level system. Therefore, it is essential to carefully analyze the energies of intermediate pair states with the objective of excluding such cases from the calculations. In our analysis, we assume the validity of perturbation theory, meaning that the interaction Hamiltonian can be computed using $\hat{H}_{\mathrm{vdW}}$, under the condition that the dipole-dipole interaction energies $J_{\mathrm{DDI}} = C_3/2r^3$ are significantly smaller than the Förster defect:

$$J_{\mathrm{DDI}} \ll \Delta_F^{ij} \quad . \tag{5.10}$$

We define this condition as violated if J_{DDI} is less than an order of magnitude smaller than Δ_F^{ij}, i.e., we require $|\frac{J_{\mathrm{DDI}}}{\Delta_F^{ij}}| \lesssim 1/10$. This becomes particularly true at short distances. For our choice of spin states, considering atom separations $r < 9$ μm, this condition is violated for magnetic fields within the red shaded area in Fig. 5.6 a).

For a magnetic field strength of $B = 158$ G, the pair state $|68P, m_j = -1/2\rangle \otimes |68P, m_j = -1/2\rangle$ has the smallest Förster defect $\Delta_F = 80$ MHz. At a separation distance of $r = 9$ μm, the dipole-dipole interaction energy amounts to $J_{\mathrm{DDI}} = 7$ MHz, making it an order of magnitude smaller.

Tuning XXZ interactions with the atom orientation in 1D

The calculation in the upper panel of Fig. 5.6 a) considers a magnetic field which is perpendicular to the atomic axis ($\theta = \pi/2$). Subsequently, we explore how the alignment between a 1D chain of atoms and the quantization axis influences the Hamiltonian's characteristics (a scenario as depicted in Fig. 5.5 a)). The lower left panel of Fig. 5.6 a) displays the anisotropy $J^{\perp}/J^{\parallel}$ as function of θ between 0 and $\pi/2$. The anisotropy varies between approximately $J^{\parallel}/J^{\perp}$ = -0.5 and around 4, depending on the relative orientation of the 1D atomic chain. This provides the flexibility to adjust the anisotropy of XXZ models widely, including changing its sign, by simply rotating the magnetic field or the atoms. The lower right panel display the interaction coefficient $C_6^{\|}$, resulting in the interaction energy $J_{ij}^{\|} = C_6^{\|}/r_{ij}^6$. This interaction strengths and its sign also vary with θ. Consequently, at $\theta = \pi/2$, one can realize an XXZ Hamiltonian featuring antiferromagnetic interactions and an anisotropy ratio of $J^{\|}/J^{\perp} = 4$.

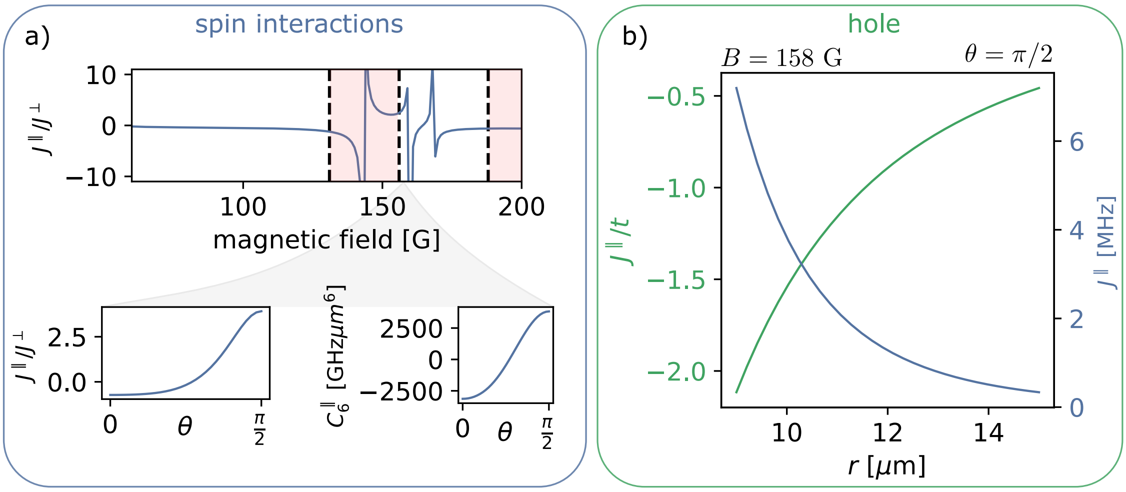

Figure 5.6: Tuning the spin and the hole degree of freedom. a) Tuning the magnetic interactions for a spin encoding $|68S_{1/2}, m_j = -1/2\rangle = |\downarrow\rangle$ and $|69S_{1/2}, m_j = -1/2\rangle = |\uparrow\rangle$. Upper panel: Anisotropy $J^{\perp}/J^{\|}$ as a function of the magnetic field. Red shaded area corresponds to regions where the system cannot be approximated with two levels due to Förster resonances. Lower left: Anisotropy as a function of the angle θ between the 1D chain and the quantization axis. Lower right: Interaction coefficient $C_6^{\|}$ as a function of θ. **b)** Green line: Ratio between the Ising interaction strength $J^{\|}$ and the hole hopping amplitude t as a function of the atom separation r for a fixed parameter configuration $B = 158$ G and $\theta = \pi/2$. Blue line: Interaction strength $J^{\|}$ as a function of the atom separation.

5.2.3 Tunable mobile dopants

The previous section introduced the feasibility of realizing antiferromagnetic XXZ models in spin systems realized with Rydberg atoms. In this section, we outline the method for introducing mobile dopants into the magnetic system. Our approach utilizes resonant dipole interactions between Rydberg $|nS\rangle$ and $|nP\rangle$ states. As previously demonstrated in experimental observations (Sec. 3.2.1), two atoms can exchange their states through these $flip - flop$ interactions (or XX model with exchange interactions in terms of a spin language). This interaction can be seen as hopping of an excitation ($|\downarrow\rangle$) from site i to j, allowing us to introduce the concept of a hole. Consequently, we assign $|nS\rangle = |\downarrow\rangle$ and $|nP\rangle = |h\rangle$ as depicted in Fig. 5.5 b), effectively enabling hopping of a spin-down excitation between two sides with an amplitude denoted as $t_\downarrow$. We define the bosonic annihilation and creation operator as $\hat{a}_\downarrow^\dagger |h\rangle = |\downarrow\rangle$ and $\hat{a}_\downarrow |\downarrow\rangle = |h\rangle$. Notably, each Rydberg atom can only carry one excitation, such that $(\hat{a}^\dagger)^2 = (\hat{a})^2 = 0$. This is called the hard-core boson constraint, and a similar implementation was realized in [46]. The Hamiltonian reads:

$$\hat{H}_{t_\downarrow} = \sum_{i,j} \frac{t_\downarrow}{2} \left(1 - 3\cos^2\theta_{ij}\right) \left(\hat{a}_{i,\downarrow}^\dagger \hat{a}_{j,\downarrow} + \text{H.c.}\right) \quad . \tag{5.11}$$

Here, $t_\downarrow = \frac{C_3}{2r^3}$ is equivalent to the $J^\perp$ dipolar coupling parameter derived in Chap. 2. By carefully selecting the hole state as an intermediate state between the two spin states, we ensure that the hopping amplitude $t_\uparrow$ to the $|\uparrow\rangle = |(n+1)S\rangle$ spin state is approximately equal to $t_\downarrow$. This equality results in the absence of a preferred hopping state, with $t_\downarrow \approx t_\uparrow \equiv t$. The proposed setting implements the hopping term in Eq. 5.7 as

$$\hat{H}_t = \sum_{i,j} \left(1 - 3\cos^2\theta_{ij}\right) \left(\frac{t_\downarrow}{2} \hat{a}_{i,\downarrow}^\dagger \hat{a}_{j,\downarrow} + \frac{t_\uparrow}{2} \hat{a}_{i,\uparrow}^\dagger \hat{a}_{j,\uparrow} + \text{H.c.}\right) \tag{5.12}$$

We note that the dipole interactions between the hole and spin states have a distance dependence of $1/r^3$, in contrast to the $1/r^6$ dependence of the magnetic interactions. Additionally, the hopping amplitude becomes angle dependent. This offers an additional tool to tune the ratio between $J^\perp, J^\parallel$ and t, enabling the exploration of various regimes.

In the current and previous section, our focus was primarily on a 1D chain of atoms, and we proposed specific parameters to realize antiferromagnetic interactions: $|68S_{1/2}, m_j = -1/2\rangle = |{\downarrow}\rangle$, $|69S_{1/2}, m_j = -1/2\rangle = |{\uparrow}\rangle$, a magnetic field of $B = 158$ G, and an angle of $\theta = \pi/2$ between the chain and the quantization axis. In this scenario, the anisotropy was characterized by $J^{\|}/J^{\perp} = 4$. We consider this particular setup and explicitly calculate the parameters where the hole state is represented by $|68P_{3/2}, m_j = -1/2\rangle = |h\rangle$, finding that $t_{\downarrow}/t_{\uparrow} = 1.05$. The green line in Fig. 5.6 b) illustrates the ratio $J^{\|}/t$, which scales as r^3 with the atom separation r. Depending on the separation distance, we can encounter scenarios where either the magnetic interaction or the hole hopping mechanism dominates the system, allowing us to explore various regimes. In particular, the regime $t \lesssim J$ remained experimentally elusive so far. The blue line represents the interaction strength $J^{\|}$ as a function of separation. Notably, at large distances $r > 14$ μm, the interaction times become considerably large and almost equal to the lifetimes of the Rydberg atoms, rendering the implementation inefficient.

Extension to 2D configurations

The previous implementation considered a 1D chain of atoms and demonstrated tunability of magnetic interactions via the magnetic field and the angle with respect to quantization axis θ, while the ratio $J^{\|}/t$ is tuned via the atom separation. This implementation can be directly extended to a 2D configuration as shown below:

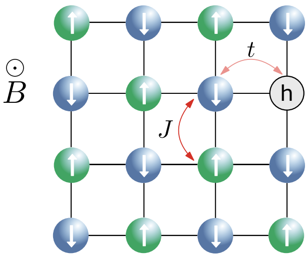

In order to keep the interaction between the spins and the hole constant and equal over the entire array, we fix the magnetic field to be perpendicular to the atom plane, resulting in $\theta = \pi/2$ for all atoms. Therefore, the parameter regime displayed in Fig. 5.6 b) could directly be applied to a 2D configuration.

Selecting a different angle results in spatially anisotropic hopping amplitudes and spin interactions, which may also contain rich physics.

5.2.4 Summary and discussion

Summary

In this section, we have explored the use of Rydberg atoms in optical tweezer arrays for studying doped XXZ models. We discussed how these models can be realized by encoding the spin and hole degrees of freedom into three carefully selected Rydberg states. In the first part, our focus was on the efficiently implementing magnetic interactions. To achieve this, we utilized states possessing the same parity such as $|S\rangle$ and $|S'\rangle$, naturally realizing XXZ models through a second-order van der Waals process. We also examined how a magnetic field could be used to shift the intermediate states close to a Förster resonance, allowing us to tune the system into a regime that features antiferromagnetic interactions. Subsequently, we explored how the angle between the atoms and the quantization axis in a 1D chain provides a parameter that enables highly tunable anisotropies. The following section addressed the implementation of the hole using direct dipolar exchange interactions between $|S\rangle$ and $|P\rangle$ Rydberg states. As these interactions scale as $1/r^3$ in the distance, compared to $1/r^6$ of the magnetic interactions, the distance between the atoms provides an additional tool to adjust the interaction parameter. This enables us to realize regimes where the hopping dominates the spin ordering and vice versa. The magnetic field regime presented for the 1D scenario was chosen to be immediately applicable for tuning the spin anisotropy in a 2D configuration.

Discussion

The proposal presented in this section represents a novel approach to investigate tunable doped antiferromagnetic quantum magnets, with the exceptional control offered by state-of-the-art Rydberg tweezer arrays [43]. Our approach relies on an analog implementation involving three Rydberg states, which can be readily addressed with microwave photons within the Rydberg manifold, similar to previous investigations in this thesis. With an experimental realization of bosonic AFM $t-J$ models within reach, this further motivates theoretical investigations exploring potential connections to high-T_c superconductivity. Due to the AFM frustration, numerical studies are challenging, placing the proposed model in a similar complexity class as its fermionic counterpart. The wide range of tunability offered by our approach provides opportunities to explore various regimes. Furthermore, our implementation of the hole is based on a third Rydberg state rather than atom removal, enabling potential interferometric measurement schemes [191].

In the following, we briefly discuss some prospects for the experimental implementation. It is important to note that, due to possible Förster resonances, the tunability of the individual terms in the XXZ Hamiltonian is not a smooth function of the tuning parameters. Careful parameter selection is necessary for specific target applications. Therefore, the derivations in this chapter should be viewed as a tutorial for finding specific interaction parameter, such as antiferromagnetic interactions with a strong Ising term. It is crucial to always verify that the pair states, through which the XXZ Hamiltonian is implemented, are not resonant with pair states in the two-level system, ensuring that the van der Waals Hamiltonian remains a good description. This is especially important as the tunability of the individual terms in the Hamiltonian requires working near Förster resonances.

In order to perform experiments, it is important to efficiently prepare the desired initial states. Of particular interest are holes doped into the antiferromagnetic ground state of the XXZ model, which is generally highly entangled. Recent experiments in the Rydberg manifold have demonstrated the ability to realize states close to the antiferromagnetic ground state with a dipolar XX model represented by Rydberg nS and nP states in a tweezer array [47]. The approach requires local control of detunings to adiabatically anneal the system into the ground state. Similar approaches might be applicable to our proposed implementation and are under investigation. The ground state could also be implemented with a a different adiabatic ramp involving a transverse magnetic field: In this approach one would initialize all spins in the x-direction of the Bloch sphere and pin them with a strong magnetic field. The x-magnetized state would then be the ground states of the strong magnetic field Hamiltonian. Adiabatically ramping down that field would ideally result in the ground state of the XXZ model. However, those schemes are still under development and require careful analysis.

Finally, it is important to emphasize that the introduced building block may not only be applicable to the implementation of the $t-J$ model but can also find utility in realizing a broad class of strongly correlated systems, such as, for example, non Abelian lattice gauge theories [192].

CHAPTER 6

Conclusion and perspectives

6.1 General conclusion and perspectives

The work presented in this thesis represents a significant advancement in the development of quantum simulators with highly tunable interaction parameters, opening up several new routes in quantum science and technology. We have introduced novel techniques for modifying the Hamiltonian of quantum spin systems and applied them to explore the out-of-equilibrium dynamics of various XYZ quantum spin models.

Our investigations in chapter 2 have demonstrated the ability to realize adjustable XX, XXZ, and Ising models with dipolar and van der Waals interactions in spatially disordered quantum spin-1/2 systems. The implementation of such quantum spin models with power-law interactions holds significant importance, as they naturally occur in various quantum simulation platforms, including different Rydberg setups [169], solid-state spin defects [170], and ultracold molecules [33, 65]. A measurement of the magnetization relaxation dynamics has revealed a remarkable universal behavior where, by rescaling time, all three relaxation curves collapsed on each other, independent of the microscopic details of the Hamiltonian. Building upon previous work presented in the dissertation of Titus Franz [61], we have advanced the description in which the system segregates into effective spin pairs by iteratively integrating out the fastest timescales, an approach known from the strong disorder renormalization group [122–125]. This description reproduces the measurements and suggests that the emergence of these effective pairs is a unifying feature of disordered quantum spin systems. A natural question that arises is whether this description holds for more general initial states and observables. Here, local access could facilitate the direct observation of the microscopic formation of spin pairs and the identification of pair correlations. Recent experiments with disordered ultracold molecules have begun to investigate such correlations with initial results that align with the pair description [33]. Furthermore, previous experiments conducted in our setup, observing the global long-term magnetization in an external field, are inconsistent with a thermal description but can be aptly described by an effective pair Hamiltonian over the experimental time scales [193]. In this context, it will be exciting to explore connections to prethermalization [9, 105–109] and determine if or when the system begins to depart from a pair-based description. Additionally, the observed magnetization relaxation dynamics are well-described by a stretched exponential function, a phenomenology well know from classical spin glasses [6]. This calls for further exploring the connection to spin glasses, which becomes particularly interesting when studying phenomena such as aging, in which the system's time-dependent response to external perturbations reflects its non-equilibrium characteristics [6].

In chapter 3, we have introduced a new building block for programmable quantum simulation. This has involved the introduction of new effective dipolar interactions into isolated quantum spin systems through the application of a periodic drive, denoted as Floquet Hamiltonian engineering. This technique is based on a simple adjustment of the delay time of $\pi/2$ pulses, transforming the natural XX model into a XYZ form, thereby opening several avenues for further exploration. Our application of this method, using an optical tweezer-based platform, provided access to nearly every parameter in the Hamiltonian which are determined by the position of atoms and the quantum spin model governing the dynamics. We have demonstrated the capability to modify spin transport properties in an ordered configuration of a few particles, comprising 10 atoms. Future steps will include scaling the system to larger number of particle and the exploration of various transport regimes, ranging from ballistic [152, 153] to diffusive transport [154], within XXZ Hamiltonians with tunable anisotropies. Furthermore, extending these studies to disordered quantum spin systems is particularly intriguing as disorder can lead to localization, effectively fully suppressing spin transport [99]. By tuning the disorder strength through the Rydberg blockade [50], it may be possible to identify transitions between different localization regimes and for different Hamiltonian parameters. Our current implementation has demonstrated the faithful realization of the desired effective Hamiltonian, with the primary perturbation arising from interactions during the $\pi/2$ pulse - a perturbation of technical nature that can be addressed in near term by faster drives.

Floquet Hamiltonian engineering directly provides new prospects for broader applications in quantum technologies. Multi-pulse sequences can be designed for various purposes, ranging from protecting quantum coherence, where certain noise terms in the Hamiltonian are effectively decoupled, to optimal quantum sensing, where the signal is enhanced through the decoupling of interactions [141]. Our demonstration of dynamically engineering the system to freeze magnetization dynamics has recently be applied to stall squeezed spin states on demand [94], a key feature for quantum-enhanced sensing applications. Floquet Hamiltonian engineering can also be applied to qudit systems with more than two levels, introducing a new route for exploring a richer landscape of realizable Hamiltonians featuring quantum many-body scars or additional spin exchange channels [158]. It will certainly be exciting to embark on this novel path of programmable quantum systems. Furthermore, the technique is not limited to the Rydberg platform. It is applicable to any platform capable of realizing spin models with an external drive, as demonstrated in recent quantum simulation experiments involving trapped ions [155] and polar molecules [33].

The two approaches presented at the beginning of this thesis have provided exceptional control over the microscopic interaction parameters of quantum many-body spin systems. In chapter 4, by combining both of these approaches, we have investigated one of the most intriguing aspects of unitary dynamics in quantum systems: the ability to effectively reverse the arrow of time by altering the sign of the Hamiltonian. This reversal of quantum many-body dynamics has been demonstrated in a dipolar Rydberg spin system featuring power-law interactions, allowing a demagnetized many-body state to evolve back-in-time into a magnetized state, which, again, stimulates new possibilities for more general quantum technologies. By time-reversing the evolution of quantum many-body systems, the effect of decoherence, resulting in an imperfect revival, can be characterized [134, 165]. This constitutes an important tool to validate the quality of general platforms exploiting quantum effects, such as entanglement, as a resource. In the context of quantum simulation, time reversal provides a powerful tool, enabling the measurement of out-of-time-order correlators to investigate quantum information scrambling [157,166–168]. These correlators provide a measure of how quickly information and entanglement spreads. This is once again interesting in disordered quantum systems, which feature localization phenomena. Here, our demonstrated capability to reverse tunable quantum spin models with different symmetries is essential for exploring new regimes. Applications further extend to the field of quantum-enhanced sensing, where time-reversal protocols enable phase sensitivity beyond the standard quantum limit in systems with limited detection efficiency [161–163]. To our knowledge, such protocols have not been applied to dipolar interacting systems, which are particular interesting as they occur in various other system as previously outlined. Building up on recent experiments demonstrating scalable spin squeezing with dipolar interactions [94], a combination with time-reversal protocols [164] could enables a new approach for quantum sensors.

The presented time-reversal protocol essentially involves changing the representation of the pseudo-spin to realize a flip of the sign in the interaction Hamiltonian. Importantly, it is not limited to Rydberg atoms and can be readily applied to other isolated quantum systems where a multitude of internal states is available. It appears also feasible to extend its application to other scenarios, such as the $t - J$ model, where a change of the representation could reverse the sign of the interaction term and the sign of the tunneling term (see Chap. 5).

In the concluding chapter 5 of this thesis, we have transitioned from experimental demonstrations to theoretical investigations, suggesting the potential of Rydberg atoms as a versatile platform for implementing more general quantum spin models. We have introduced a method in which the dipolar Rydberg interactions are engineered using a static electric field, effectively emulating spin Hamiltonians found in nuclear magnetic resonance (NMR) systems [167]. The implementation of this specific model paves the way for the application of sophisticated NMR time-reversal sequences to study diverse phenomena, such as those used to investigating localization in mixed quantum states [167]. The application of these protocols to Rydberg atoms, which offer the capacity to implement pure quantum states in an isolated environment with local readout, will enable in-depth studies of localization regimes and possible transitions [99]. Finally, we have presented a scheme for introducing mobile dopants into the Rydberg spin system by mapping spin and hole degree of freedoms to three Rydberg states, effectively realizing doped quantum magnets. The realized bosonic $t - J$ model has rarely been studied experimentally [187, 188]. It remains unclear whether such a model captures some of the fundamental features of strongly-correlated electrons, such as high-T_c cuprate compounds. Given the large amount of tunable interaction parameters we have introduced in combination with the previously outlined benefits of the Rydberg platform, we are confident that such an implementation will provide new insights in strongly-correlated quantum systems.

In summary, the extensive tunability of Rydberg quantum simulators brings us a step closer to realizing Richard Feynman's initial vision of fully programmable quantum simulators [7]. In addition to its significance in quantum simulation, these studies potentially influence more general quantum technologies. While we are not there yet, the ability to tune the Hamiltonian as desired could open up avenues for in-depth exploration of how microscopic interactions impact macroscopic properties.

This represents a pathway towards customized material design, which may, at some point in the future, have an impact on our everyday lives.

6.2 Perspectives for the Heidelberg Rydberg experiment

The investigations conducted in this thesis have paved the way for additional studies. Below, I will briefly overview potential further experimental investigations, some of which have already begun.

Probing out-of-equilibrium phases of matter Our findings in chapter 2 revealed that the magnetization relaxation dynamics in our Rydberg spin system can be effectively described by a pair model. This suggests that the present disorder prevents it from directly reaching the thermal equilibrium described by the full many-body Hamiltonian. In addition, chapter 3 demonstrated that our system is well-suited for applying periodic spin manipulations. These are two ingredients ideal for investigating the potential emergence of out-of-equilibrium phases of matter within our isolated Rydberg spin system.

Our focus will be on the investigation of so-called discrete time crystals, which represent many-body phases of matter characterized by a spontaneously broken discrete time-translation symmetry. Originally proposed by Frank Wilczek in 2012 as an equilibrium phase of matter with broken continuously time translational symmetry [194], it was proven in 2015 that time crystals are not possible in equilibrium [195]. However, by relaxing the equilibrium requirement, it has been demonstrated that time crystals can indeed exist in systems that are not in thermal equilibrium, such as Floquet systems, where discrete time translational symmetry is broken [196]. Over the recent years, there has been experimental effort to study these systems, with the first demonstrations on two platforms in 2017 [132, 133]. Therefore, it will be interesting to address the following questions: (i) Does such a phase of matter exist in a disordered spin system with power-law interactions in 3D? (ii) What is the lifetime of such a phase? (iii) What is the roll of spin pairs this phase?

To address this question, we will employ a sequence as shown in Fig. 6.1 a), inspired by previous investigations [132, 133]. Starting from a polarized state along the z-direction, we apply a π pulse, inverting the z-magnetization, and allow for interactions over a period τ. We have performed preliminary experiments using this protocol with the results shown in Fig. 6.1 b) - e). We have found that for a perfect π pulse with short waiting time, the z-magnetization exhibits oscillations over 100 cycles of this sequence with a frequency of $\nu = 1/2$ (Fig. 6.1 b)). With the same waiting time but with a small error in the π pulses (a small under-rotation which does not fully invert the z-magnetization), we observe a beating in the magnetization with different frequency components (Fig. 6.1 c)). For the same error but longer waiting time, we recover the $\nu = 1/2$ peak (Fig. 6.1 d)). Furthermore, the so-called crystalline fraction $\frac{|S(\nu=0.5)|}{\sum|S(\nu)|}$, comparing the amplitude at $\nu = 1/2$ frequency to the amplitudes in the rest of the Fourier spectrum as a function of the error ϵ, is enhanced for longer waiting time (Fig. 6.1 e)). Consequently, due to the interactions, the z-magnetization display a periodicity with frequency $\nu = 1/2$ even at small perturbations. These are clear signatures of a discrete-time crystalline phase. It will be exciting to study this phenomenon in further experiments by probing the full phase diagram, conducting a detailed study of the lifetime, and theoretically understanding the connection to the pair model.

Towards aging in disordered quantum spin systems and the possible relation to spin glasses The glassy relaxation dynamics observed in chapter 2 call for further investigations, particularly because such relaxation dynamics are characteristic of classical spin glasses [6]. Below a critical spin glass temperature, where thermal fluctuations are suppressed, these systems relax in a stretched exponential fashion. This due to the fact that, at low temperature, the system is stuck in local minima of the energy landscape, resembling a quasi-equilibrium. This is in contrast to the

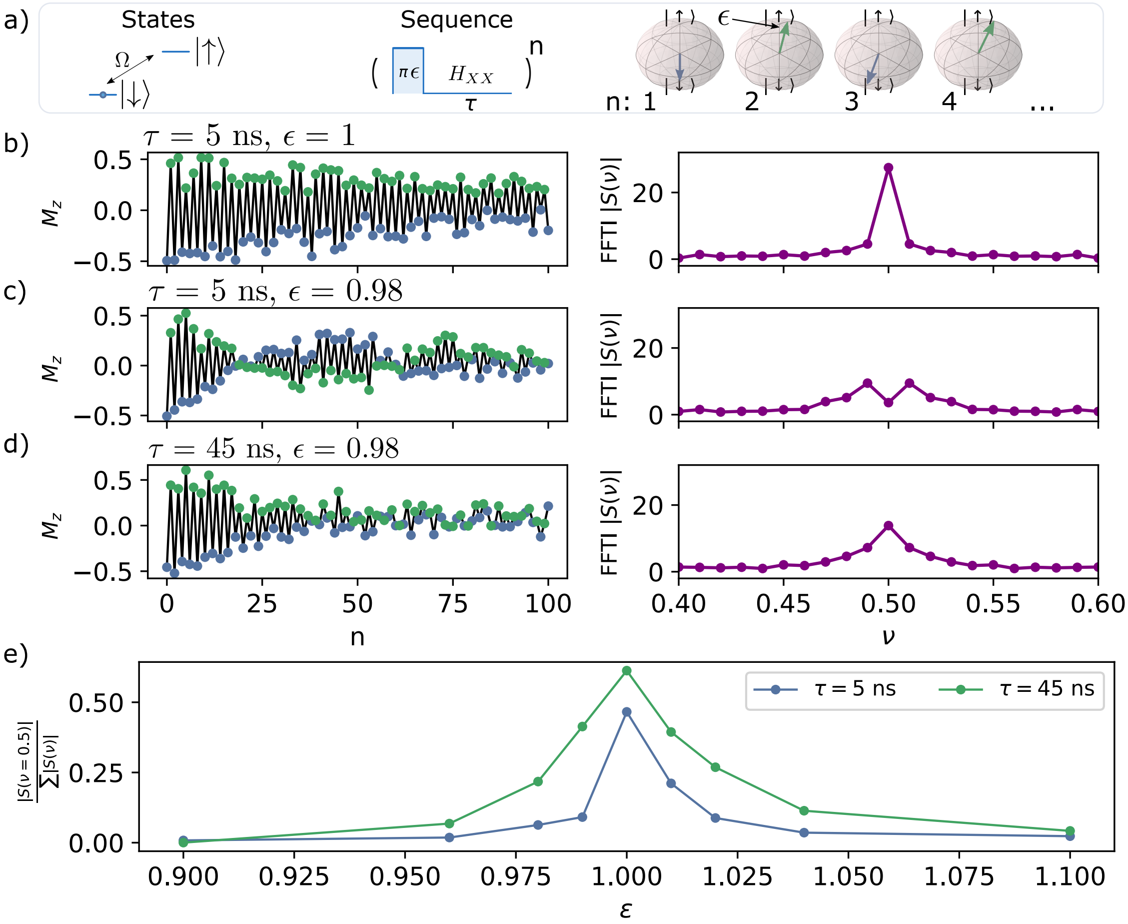

Figure 6.1: Preliminary: Discrete-time crystals. a) Experimental sequence to probe time crystalline behavior: We start with polarized state along the z-direction. The π pulse flips the z-magnetization every cycle. By varying the time of the π pulse, we can induce a slight under-rotation ϵ. **b)** Left: z-magnetization as a function of the number of cycles n (blue: even, green: odd cycles) for waiting time $\tau = 5$ ns and without pulse error $\epsilon = 1$. Right: Fourier transform intensity of the left trace. **c)** as in b) for the same waiting time $\tau = 5$ ns but with a small under-rotation $\epsilon = 0.98$. **d)** as c) for the same pulse error $\epsilon = 0.98$ but with larger waiting time $\tau = 45$ ns. We observe a recovery of the $\nu = 1/2$ oscillations. **d)** Crystalline fraction $\frac{|S(\nu=0.5)|}{\sum|S(\nu)|}$ as a function of ϵ.

quench experiments performed in chapter 2, which involved eigenstates spread across the entire energy spectrum. Therefore, it would be interesting to explore dynamics in the low energy spectrum of disordered quantum spin system and identify potential distinctions or common features to classical spin glasses. A possible phenomena to expect in the low energy regime is aging, where the system's response to a perturbation exhibits significant time-dependent characteristics, meaning it depends on how long the system has evolved before the perturbation is applied. In classical spin glasses, such behavior was observed below the spin glass temperature for extremely long times, reflecting the non-equilibrium nature of the system [6].

A possible experimental protocol to probe such behavior is shown in Fig 6.2 a). The procedure involves initializing the spins along the x-direction of a Bloch sphere and locking them with a strong field pointing along the spins. This state represents the paramagnetic ground state of the transverse field spin model. Adiabatically reducing the field strength then provides access to the low energy spectrum of the Hamiltonian. For an infinitely slow ramp, the true ground state of the Hamiltonian can be reached, while faster ramps prepare states with increasing energy. Following a waiting time τ, the external field is applied again, resulting in a magnetization response along the x-direction. This response may depend on the waiting time τ between the ramp and the perturbation, which called aging [6]. Furthermore, the dependence of this response on the ramp speed may reveal signatures of a potential spin glass phase transition.

Quantum-enhanced sensing with power-law interactions As demonstrated in chapter 4, our Rydberg setup has the capability to reverse the time evolution of a many-body system. Time reversal constitutes a powerful tool in quantum-enhanced sensing protocols [164], demonstrating phase sensitivity below the standard quantum limit [161–163]. The advantages of these protocols stem from the ability to reduce the requirements for the detailed readout of exact complex quantum states. Time reversal approaches involve the generation of entangled states via a Hamiltonian process. In this entangled state, the system is subjected to the signal under consid-

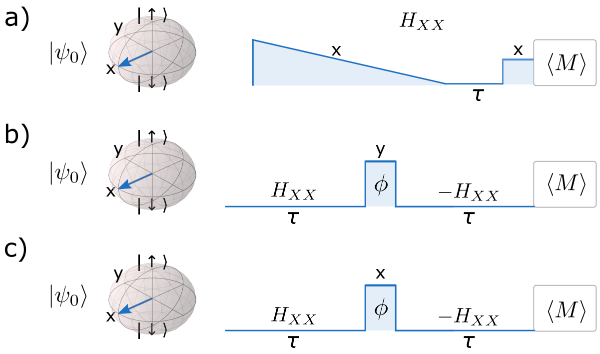

Figure 6.2: Experimental protocols for further studies. Left: Sketch of the initial state along the x-direction. **a)** Sequence to study aging phenomena. An external field that locks the spins is gradually reduced to access the low energy spectrum of the Hamiltonian. After a waiting time τ, the field is turned on again and the response in the magnetization measured. **b)** Sequence to study quantum-enhanced sensing. The polarized state evolves into an entangled state under H_{XX}. Subsequently, the state is rotated by an angle ϕ about the y-axis, before $-H_{\mathrm{XX}}$ is applied. In this protocol ϕ translates into a y-magnetization. **c)** Sequence to study out-of-time-order correlators. Same as b), with the only difference being a rotation about the x-axis.

eration, which typically consists of a phase ϕ, induced by a rotation. Afterward, the reversed Hamiltonian is applied and the system evolves backward in time. Consequently, the final state can become displaced relative to the initial state, resulting in an amplification of the phase signal ϕ [164].

Inspired by previous proposals for collective spin models [164], a possible experimental sequence consists in a spin initialization long the x-direction in a Bloch sphere as illustrated in Fig 6.2 b). Then the many-body system evolves under the XX model into a complex state. One then can apply a phase shift ϕ about the y-axis, which is realized by the microwave field and results in a finite z-magnetization. Afterward, the reversed Hamiltonian is applied before measuring the global magnetization components. The displacement with respect to the initial state becomes apparent with a y-magnetization component that increases for longer evolution times and, consequently, more complex states that sense the phase ϕ.

As described previously, due to the recent experimental observations of scalable spin squeezing in dipolar interacting Rydberg systems [94], it will be interesting to investigate how time-reversal-based sensing protocols combine with dipolar interactions, as the naturally appear in various systems ranging from solid-state spin defects [170] to ultracold molecules [33,65]. In general such sensing protocols rely on strongly entangled states, which are extremely sensitive to the perturbation. Therefore, it will be exciting to see how the disorder in our system, typically slowing down the build-up of entanglement, affects the amplification of the signal ϕ. Even more interestingly, we can directly investigate how the amplification depends on disorder since it can be tuned by changing the Rydberg density (at a fixed Rydberg blockade radius) [50].

Measuring information spreading through out-of-time-order correlators The ability to reverse many-body dynamics is also directly applicable to study quantum information scrambling through the measurement of out-of-time-order correlator [157]. They provide a measure of how quickly information and correlation spread in the system by assessing the sensitivity of the revival of a quantum state to small perturbations, similar to the sensing experiment.

As a first step, the protocol previously presented in the context of a collective spin system [166] can be applied to our Rydberg system featuring power-law interactions (see Fig 6.2 c)). An x-magnetized state evolves for a certain time before a rotation around the x-axis with an angle ranging from 0 to 2π perturbs the system. Reversing the evolution and Fourier transforming the signal reveals information about the multiple quantum coherence spectrum. It will be particularly interesting to investigate how out-of-time-order correlators depend on the degree of disorder in the system, which can, again, be tuned through the Ryderg density [50]. In a localized system, information spreading is expected to be suppressed, while ordered, non-localized systems, faster information spreading is expected. Such measurements can directly be used to further investigate the effective pair description, which predicts that correlations are not spreading over the system to 0th order.

Appendices

APPENDIX A

Alkali Rydberg atoms and their properties

This appendix summarizes selected properties of Rydberg atoms that are relevant for understanding the experiments presented in this thesis. A more detailed overview can be found in [44]. Atoms that have at least one electron excited to a high-lying atomic state, characterized by a large principal quantum number n, are commonly referred to as Rydberg atoms. Compared to ground-state atoms, the electron is on average up to four orders of magnitude further away from the core and thus weakly bound, making the atoms extremely sensitive to external fields. At first glance, this sensitivity may seem like a disadvantage, as the atom can be easily perturbed. However, advances in laser cooling and trapping techniques have enabled the precise creation and control of these atoms, with their sensitivity being the key resource for quantum engineering applications over the past few centuries.

While Rydberg atoms can be created with atoms possessing multiple valence electrons, this thesis uses rubidium 87, an alkali atom with one valence electron. Considering the valence electron as excited to a high-lying state, the electrons on the inner shell are effectively shilding the charge of the core. Therefore, the valence electron experiences a modified hydrogen-like potential with a sole positive charge. The wavefunctions are hydrogen-like, and the binding energies can be calculated by the modified Rydberg formula:

$$E_{n^*} = -hc\frac{R_{Rb}}{n^{*2}} = -hc\frac{R_{Rb}}{.}(n-\delta_{n,l})^2 \tag{A.1}$$

Here, R_{Rb} is the effective Rydberg constant for rubidium and $n^* = n - \delta_{n,l}$ the effective principal quantum number. $\delta_{n,l}$ is the so called quantum defect and reflects the shielding of the core by the inner electrons.

Many important properties scale as n^* to the power of some exponent. A few selected properties are listed in table A.1.

Property	n^* scaling
Level spacing $E_{n^*+1} - E_{n^*}$	n^{*-3}
Dipole moment d	n^{*2}
Direct dipolar interaction strength	n^{*4}
van-der-Waals interaction strength	n^{*11}
Polarizability	n^{*7}
Radiative lifetime τ	n^{*3}
Ionizing field E	n^{*-4}

Table A.1: Scaling of selected of Rydberg atoms properties with the effective principal quantum number n^*.

The energy level spacing between adjacent $|n^*S\rangle$ and $|n^*P\rangle$ states decreases with n^{*-3}. These energy levels usually fall within the microwave regime, corresponding to frequencies in the range of several tenths of GHz. State-of-the-art microwave generators have advanced to the point where they can directly create these frequencies with an exceptionally high degree of coherence that surpasses experimental timescales by orders of magnitude. Furthermore, arbitrary waveforms can be produced that result in high control fidelity. The dipole moment d between two adjacent states scales as n^{*2}. Thus, Rydberg atoms exhibit extremely strong dipolar ($\sim n^{*4}$) and van der Waals interactions ($\sim n^{*11}$). The latter of these can be up to ten orders of magnitude greater than for ground-state atoms and typically falls in the range of several tenths of GHz. The lifetime of atoms in Rydberg states scales as n^{*3} and is usually on the order of tenths of microseconds. Thus, the ratio between lifetime and interaction strength enables long coherence times. Additionally, experiments that are on the order of a few microseconds are less sensitive to technical noise. Another important property of Rydberg atoms is the n^{*-4} scaling of the electric field required to ionize the atom. Therefore, the electric field required to ionize Rydberg atoms is orders of magnitude smaller than for ground-state atoms. For the rest of this thesis, we define the effective principle quantum number n^* without * for better readability.

Rydberg blockade mechanism

The Rydberg-Rydberg interactions described in Chap. 2 have a significant impact on the excitation dynamics of Rydberg atoms. In this thesis, we consider excitation to a Rydberg $|nS\rangle$ state. For two atoms, Fig. A.1 shows the pair states energies as a function of their distance R. The energy of both atoms in the ground state $|gg\rangle$ or one being excited to the Rydberg state $(|gr\rangle, |rg\rangle)$ does not change as a function of the distance R. The situation is different for the doubly excited Rydberg state $|rr\rangle$, where energy shifts as a function of R due to the distance-dependent van der Waals Rydberg-Rydberg interaction.

As a consequence, a single-frequency excitation laser that can excite $|rr\rangle$ at large distances is not able to excite $|rr\rangle$ at small distances. The critical distance below which two atoms can no longer be simultaneously excited is called the blockade radius R_b. In general, R_b depends on the excitation bandwidth, which is, for example, affected by the strength of the laser or the excitation pulse length. This Rydberg blockade effect is one of the key resources for quantum technology applications, such as fast gate-based quantum computing [120, 197–199].

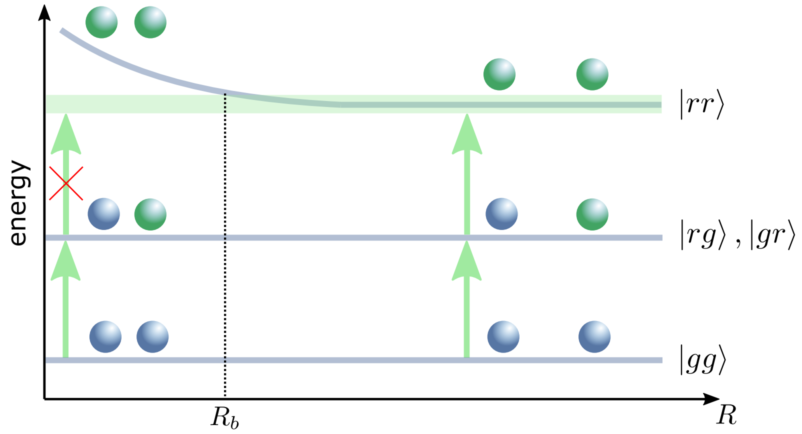

Figure A.1: The Rydberg blockade. Energies of the two atom pair states as function of the inter atomic distance R. Atoms in the ground state illustrated by the blue spheres, while atoms in the Rydberg state are green. For distances below R_b, the double excited pair state is shifted out of resonance and can not be excited. The width of the shallow green line displays the Rydberg excitation bandwidth.

APPENDIX B

Experimental preparation and manipulation of Rydberg atoms

B.1 Experimental preparation of Rydberg atoms

Various experimental settings have been used for implementing Heisenberg spin models with Rydberg atoms. One of these approaches involves neutral atom arrays, where single atoms are trapped and rearranged using optical tweezers (tightly focused laser beams) before being excited to the Rydberg state. This method provides access to local control and readout of a few hundred atoms and turned out to be a powerful approach [43] and is relevant for the experiments presented in Chap. 3. In contrast, our experimental approach at the Rydberg experiment in Heidelberg differs as we prioritize realizing large systems with thousands of Rydberg atoms in three spatial dimensions and give up local control. The Rydberg excitation is performed in a gas of neutral atoms, rendering the system spatially disordered. Instead of addressing the spins locally, we use a global microwave field to perform coherent spin manipulations.

In order to efficiently perform quantum simulation experiments, the experimental setup has to fulfill certain points:

(i) Preparation of cold atomic samples: While there exist experiments that study the effect of atomic motion on quantum dynamics, the experiments presented in this thesis aim to study interactions between atoms at rest. In this so-called frozen gas regime, atoms are not moving significantly over the timescales of the experiments, and the coupling parameters in the Hamiltonian are therefore time-independent. To achieve this, we require cloud temperatures where atomic motion has a negligible effect on quantum dynamics.

(ii) Preparation of a well-defined ground state: For experiments with spin-1/2 systems, it is important to implement two isolated levels in the Rydberg manifold. Therefore, a single hyperfine state in the ground state manifold is prepared, from which Rydberg atoms are excited into one Rydberg state.

(iii) Rydberg excitation: For the quantum simulation experiments presented in this thesis, we exploit strong Rydberg-Rydberg interactions. Therefore, after having prepared atoms in the ground state, the energy difference to the Rydberg manifold has to be overcome. This is achievable with a two-photon transition, including a red 780 nm and blue 480 nm laser.

(iv) External field control: The main characteristic of alkali Rydberg atoms is the large separation between the atomic core and the valence electron, rendering them extremely sensitive to external electric fields. Therefore, we require high-level electric field control that can be adjusted to cancel stray fields.

In addition to electric fields, the ability to apply a large magnetic field is crucial to splitting the different Zeeman sub-levels in the Rydberg manifold in order to separate an isolated two-level spin system.

(v) State-sensitive Rydberg atom detection: Detecting a two-level system in a state-sensitive manner is important for experiments with spin-1/2 systems. As our spin-1/2 system will be encoded in the Rydberg manifold, we need to distinguish two Rydberg states that are nearby in energy. This is realizable with a combination of de-exciting one Rydberg state while ionizing the other one. The resulting ions can be detected using a multi-channel plate.

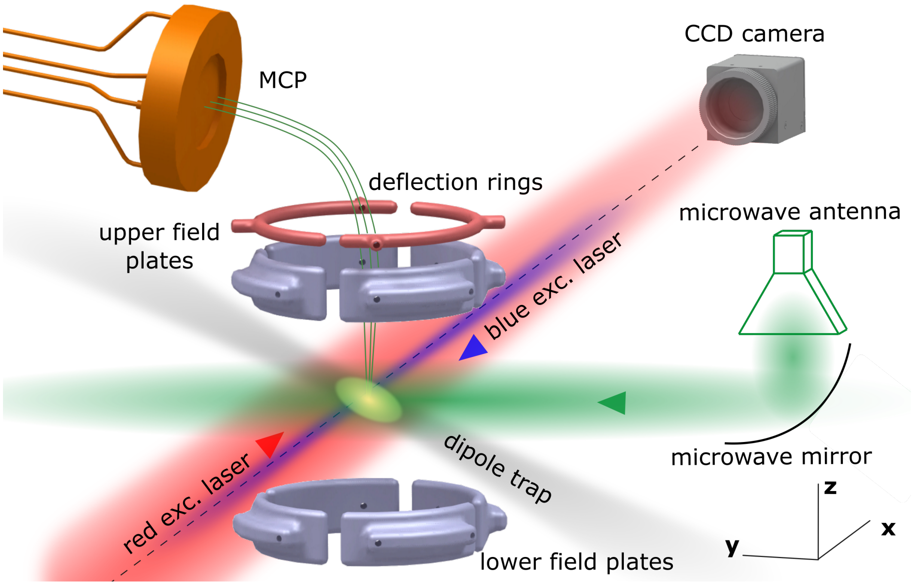

Figure B.1: Experimental apparatus. After the MOT phase, rubidium atoms are trapped in an optical dipole trap (grey line). The cloud is imaged with a CCD camera. The two-photon excitation to the Rydberg state is performed using a red 780 nm and a blue 480 nm laser (red and blue lines). An antenna emits the microwave radiation which is then focused in the chamber using a microwave mirror (green line). By using the upper and lower field plates, an electric field is applied to ionize the atoms and detect the ions in a multi channel plate (MCP). Figure adapted from [200].

In the subsequent part of this section, we present the most important stages of the experiment employed for creating cold rubidium atom samples, exciting them into the Rydberg state, and detecting the Rydberg states. The experimental sequence is sketched in Fig. B.3 b) and the relevant energy level scheme in Fig. B.3 a). The microwave control which is used to coherently manipulate the spins, is part of the next section.

(i) Preparation of cold atomic samples

The experimental apparatus, which is used to perform the main experiments in this thesis, is sketched in Fig. B.1. A more detailed description of the setup can be found in previous thesis [200–203]. It exploits well-developed laser cooling and trapping techniques, widely applied in the field of ultra-cold atom experiments [13, 204]. Rubidium 87 atoms are initially cooled within a 2D magneto-optical trap (MOT). Subsequently, they are moved into the primary scientific chamber, where the atomic cloud undergoes additional cooling through a 3D MOT setup. Afterwards, the atoms are loaded into a dipole trap, which is used for spatial confinement and further evaporative cooling, enabling temperatures of tenths of μK. In the following, the essential elements of these traps and the associated experimental sequence for generating a cold atomic cloud are outlined.

2D-MOT Our experiments start with a dispenser used to emit rubidium atoms. Unfortunately, the typical velocities of these emitted atoms are approximately a few hundred meters per second, which are above the usual trapping velocities of 3D-MOTs, typically around ~ 10 m/s [205]. While there are several methods for pre-cooling the atoms, our approach is based on a 2D MOT: The dispenser emits a rubidium background vapor inside a glass cell that is placed outside the main science chamber [205]. Here, the atoms are cooled in two spatial dimensions, before a beam pushes them along the third dimension inside the science chamber through a differential pumping stage. This ensures that mainly rubidium 87 is present in the main chamber. Furthermore, for better optical access, the glass cell of the 2D MOT is connected on a viewport off-axis [206] (see Fig. B.2).

3D-MOT Following pre-cooling, the atoms are loaded into a 3D-MOT positioned within the central area of the scientific chamber. This 3D-MOT involves the use of two laser beams that are counter-propagating along each of the three dimensions.

As depicted in the energy level diagram in Fig. B.3 a), the cooling cycle includes cooler beams operating on the $|5S_{1/2}, F = 2\rangle \rightarrow |5P_{3/2}, F = 3\rangle$ transitions, which are detuned by $\Delta_c = 3\Gamma$ (where Γ represents the decay rate of the $|5P_{3/2}, F = 3\rangle$ state). To close the cooling cycle, a second resonant beam is applied to the $|5S_{1/2}, F = 1\rangle \rightarrow |5P_{3/2}, F = 2\rangle$ transition, effectively repumping atoms that ended up in the $|5S_{1/2}, F = 1\rangle$

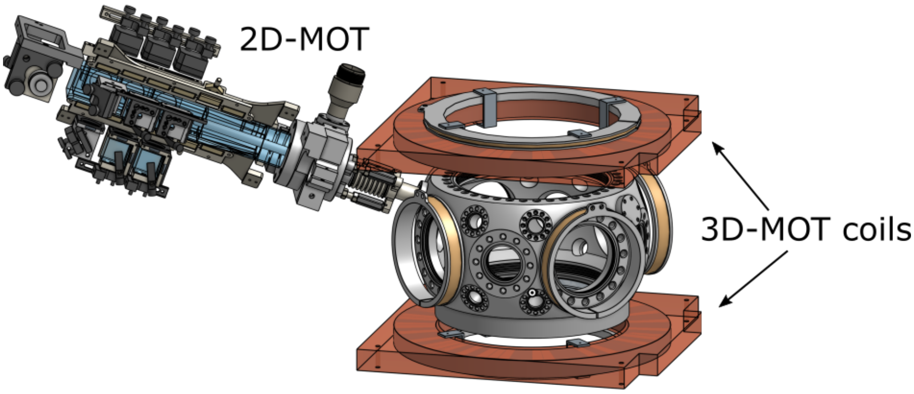

Figure B.2: 2D- and 3D Magneto optical trap setup. Large water cooled 3D-MOT coils are placed below and above the science chamber. The 2D-MOT is placed off-axis.

state due to decay. The water-cooled magnetic field coils are placed above and below the science chamber, connected in an anti-Helmholtz configuration (see Fig. B.2). Furthermore, smaller, so-called compensation coils are attached to the chamber's view port, enabling it to shift the position of the zero magnetic field inside the chamber. In order to increase the atomic density and lower the temperature in the MOT, a compressed MOT phase [207] and a dark MOT phase [208] are applied, which also helps to efficiently load into the dipole trap. The green circles in the $|5S_{1/2}, F = 2\rangle$ manifold in Fig. B.3 a) illustrate the populated hyperfine states after this MOT phase. Typical MOT loading times are on the order of 500–1000 ms.

Optical dipole trap After the 3D MOT phase, the atoms are loaded into an optical dipole trap. These traps utilize a light-induced modification of the ground state energy of neutral atoms, resulting in a trapping potential that scales proportional with the intensity of the laser [209]. For red-detuned light, atoms are trapped in regions of high intensity. In the experiment, the dipole trap is realized using 1064 nm light emitted from a Mephisto MOPA. Instead of using a single focused laser beam, we "recycle" the light and built a crossed dipole trap, where the beam is sent back into the science chamber and crosses the original beam under an angle of ~ 9 degree. This approach increases the axial confinement in comparison to a single-arm

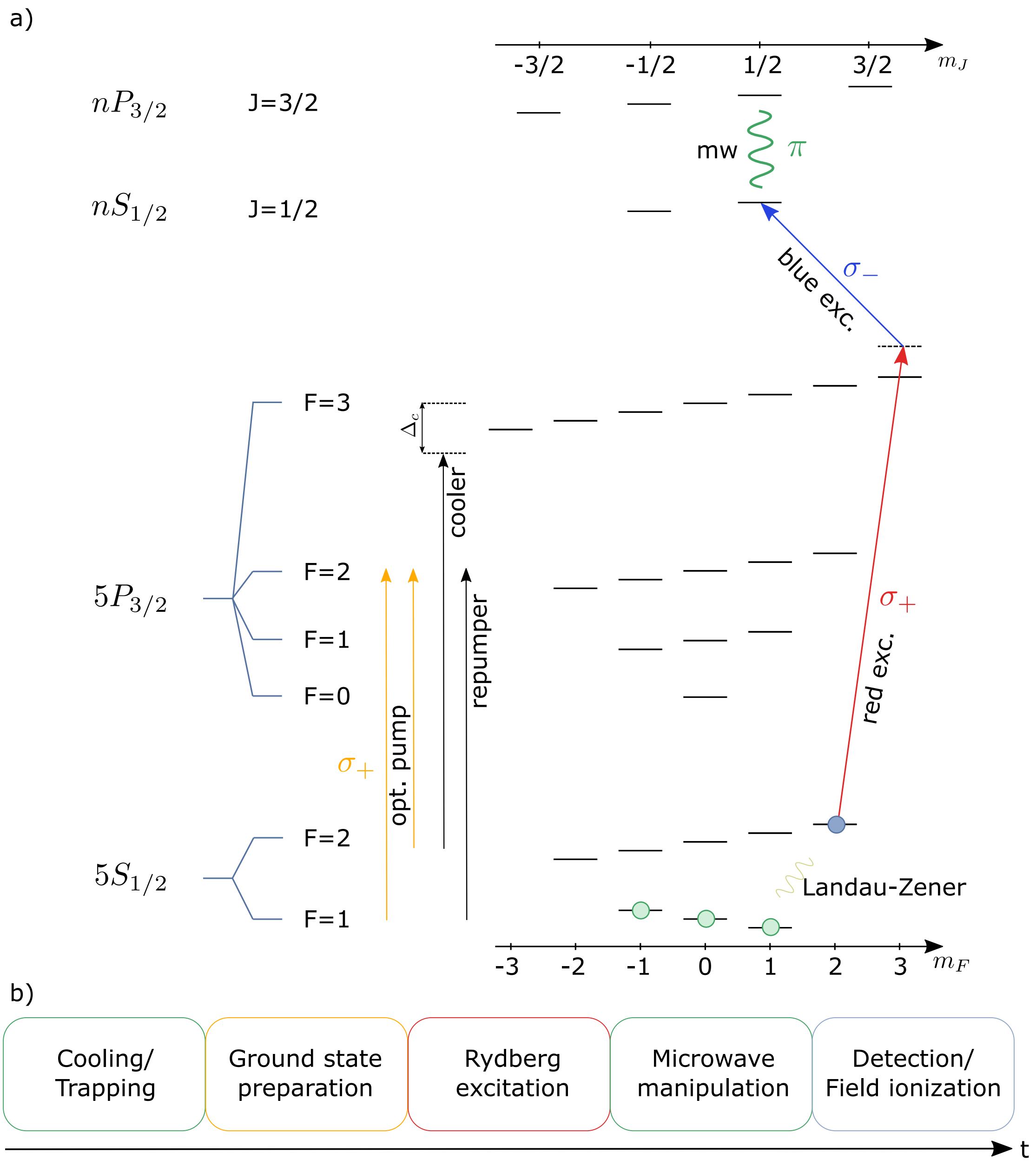

Figure B.3: Energy level diagram of ^{87}Rb and the experimental sequence. a) Energy level diagram of rubidium 87. See the main text for details on the applied preparation laser. **b)** Experimental sequence to perform experiments with an ultracold cloud of Rydberg atoms.

optical dipole trap. The waists of the 1064 nm laser were selected such that trap depth and size optimized the loading procedure. An illustration is shown by the gray beams in Fig. B.1.

The beam for the optical dipole trap is already turned on during the 3D-MOT phase. We let the atoms thermalize for $\sim$ 300 ms and decreased the intensity to allow for a bit of evaporative cooling. With this approach, we can achieve atom densities on the order of $2 \cdot 10^{11}$ cm^{-3} and temperatures of about tenths of μK.

(ii) Preparation of a well-defined ground state

To efficiently prepare a specific Rydberg state, it is crucial to start the excitation process in a well-defined ground state. As mentioned previously, the rubidium atoms populate the $|5S_{1/2}, F = 1\rangle$ hyperfine manifold (green circles in Fig. B.3 a)). Our target ground state is the $|5S_{1/2}, F = 2, m_F = 2\rangle$ hyperfine state (blue circle in Fig. B.3 a)). This state is prepared using optical pumping techniques [210]. We present an overview of these schemes in the following. More details can be found in reference [203].

Optical pumping In order to transfer the atoms from the equally populated m_F hyperfine state in the $|5S_{1/2}, F = 1\rangle$ manifold to the target $|5S_{1/2}, F = 2, m_F = 2\rangle$ state, we apply an optical pumping scheme. Therefore, a resonant circular polarized beam addresses the $|5S_{1/2}, F = 1\rangle \rightarrow |5P_{3/2}, F = 2\rangle$ transition as illustrated by the yellow arrows in Fig. B.3 a). From $|5P_{3/2}, F = 2\rangle$, the atoms decay either to the target $|5S_{1/2}, F = 2\rangle$ manifold or back to $|5S_{1/2}, F = 1\rangle$. A second, also circular polarized, beam is 7 MHz detuned from the $|5S_{1/2}, F = 2\rangle \rightarrow |5P_{3/2}, F = 2\rangle$ transition. After a few ms, the atoms cycled to the target $|5S_{1/2}, F = 2, m_F = 2\rangle$ state, which is a dark state for the applied light and scatters no photons.

Landau-Zener passage Due to inefficiencies in the optical pumping scheme, some remaining atoms occupy the other m_F levels within $|5S_{1/2}, F = 2\rangle$. We remove these atoms using two Landau-Zener passages [210]: For a simplified two-level system, the population of the initial state can be transferred to the second state via a sweep over the resonance. Exploiting this concept, we sweep a 6.8 GHz microwave field across the $|5S_{1/2}, F=2, m_F=2\rangle \rightarrow |5S_{1/2}, F=1, m_F=1\rangle$ resonance. Afterwards, we apply a beam that is resonant with $|5S_{1/2}, F=2\rangle \rightarrow |5P_{3/2}, F=2\rangle$ to depopulate residual atoms. Afterwards, we apply a second Landau-Zener passage from $|5S_{1/2}, F=1, m_F=1\rangle \rightarrow |5S_{1/2}, F=2, m_F=2\rangle$. With this procedure, typically 95 percent of the atoms populate the desired ground state. Moreover, this method serves to adjust the density within the target ground state.

(iii) Rydberg excitation

In our investigation of quantum spin systems involving atoms in highly excited states, we must overcome the energy difference to access the Rydberg manifold. This can be achieved through either a single-photon transition utilizing a UV laser or, as employed in the experiments in this thesis, a two-photon transition. To address the Rydberg state, we use a red 780 nm laser (Toptica DLpro) coupling $|5S_{1/2}, F=2, m_F=2\rangle \rightarrow |5P_{3/2}, F=3, m_F=3\rangle$, as well as a blue 480 nm laser (Toptica SHG system) coupling $|5P_{3/2}, F=3, m_F=3\rangle$ to a Rydberg with typical principle quantum number $n \approx 48-61$ (see Fig. B.3 a)). For the excitation, the laser is tuned to the two-photon resonance, but the intermediate state is detuned by $\sim$ 100 MHz. With this, we can adiabatically eliminate the intermediate state and describe the excitation process as a quasi-two-level system with Rabi frequency $\Omega_{2\gamma} = \frac{\Omega_r \Omega_b}{2\Delta}$. In typical settings, this technique allows us to tune the Rydberg atom number from a few tenths to a few thousands with in 1 to 5 μs. Furthermore, the blue 480 nm laser is focused on the atoms, and the lense is mounted on a translation stage, allowing for tuning the size of the beam.

(iv) External field control

Magnetic field control In order to realize controlled two-level systems within the Rydberg manifold and study the physics of the spin-1/2 system, for a given Rydberg state, surrounding Zeeman states need to be shifted away by a magnetic field. This is particularly important for scenarios that involve microwave driving where Zeeman shifts need to be larger than typical Rabi frequencies. During the course of this thesis, a H-bridge was built and connected to the 3D-MOT coils (see Fig. B.2). A H-bridge allows for switching the direction of current, going from an anit-Helmholtz configuration to a Helmholtz configuration. The big advantage comes with the water cooling of these coils, allowing them to apply currents larger than 200 A. At these magnetic fields, Zeem substates are shifted by more than 100 MHz.

Electric field control Due to their larger polarizability, Rydberg atoms are extremely sensitive to electric fields. The experimental setup also possesses eight electric field electrodes, which are 14 cm away from the atom [200]. They allow us to compensate for electric stray fields in three dimensions. Additionally, we can apply a field larger than a few hundred V/cm, enough to ionize Rydberg atoms with the principle quantum number $n > 48$, employed in this thesis. The electric field ramps are realized with an arbitrary waveform generator before being amplified to high voltages using a custom-made amplifier.

Rydberg atom detection

To conduct efficient spin experiments, it is crucial to differentiate between different spins, and thus Rydberg states. For this purpose, a robust electric field of hundreds of V/cm is applied to ionize the atoms. The resulting ions are then guided by our field plates and a deflection ring to the multi channel plate (MCP). A fast oscilloscope is used to read out the time trace, which allows us to reconstruct the number of ions. Due to geometrical constraints on the MCP channels, this method provides detection efficiencies of maximally 40 %. For our experiments, we typically use between 100 and a few thousand Rydberg atoms. To distinguish the two Rydberg states, we can apply two approaches:

Optical de-excitation: One approach to differentiate between the two spin states involves the removal of one of them before applying the ionization field. This is achieved by optical de-excitation of the $|nS\rangle$ state by means of a strong single photon on-resonant coupling to the intermediate $|5P_{3/2}, F=3, m_F=3\rangle$ state using our 480 nm laser (illustrated in Fig. B.4). This state decays back to the $5S$ ground state with a rate of $\Gamma/2\pi = 6$ MHz, such that the $|nS\rangle$ state is depopulated within typical de-excitation pulse times of $\sim \mu s$. Details of this scheme can be found in [211]. After removing this state, the remaining one gets ionized. This detection scheme is used to perform the experiments presented in the thesis.

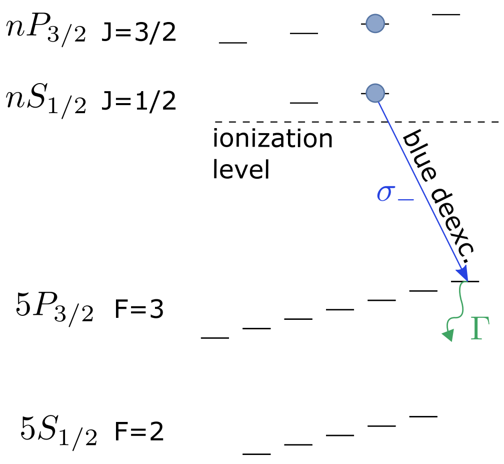

Figure B.4: Optical de-excitation. After performing experiments with spin represented by Rydberg $|nS\rangle$ and $|nP\rangle$ states, a resonant blue laser at 480 nm couples $|nS\rangle$ to the $|nP_{3/2}, F=3, m_F=3\rangle$, that decay at a rate of $\Gamma/2\pi = 6$ MHz. After de-exciting $|nS\rangle$, we apply a strong electric field ionizing the remaining $|nP\rangle$ atoms which allows us to distinguish the two states.

State-selective field ionization: The previous method has the disadvantage that information about one of the spin states is lost. However, it is generally desirable to detect both spin states in a single experimental realization. This is achieved by the application of a slow electric field ramp, ionizing first the upper state and afterwards the lower one. The results are two bunches of ion peaks hitting the MCP, separated in time. However, in strongly interacting regimes or for low energy splittings between the two Rydberg states (mainly for high principal quantum numbers), these two bunches overlap and are hard to distinguish. In the future, we want to optimize this procedure in terms of field ramps to access both populations in one shot.

B.2 Rydberg state microwave control

One of the main desired capabilities of quantum simulation platforms is the ability to perform coherent spin manipulations. Our experiments in the Rydberg manifold start with atoms in a $|nS\rangle$ state. The level spacing of adjacent states scales with n^{-3}, resulting in typical transition frequencies lying in the GHz range. How these frequencies are generated and how the field is applied to the atoms is the subject of this section.

The main microwave setup was designed and built during the course of my master's thesis [149]. During the time of this thesis, a new fast 64 GSa/s arbitrary waveform generator was implemented, allowing for spin manipulations on the picosecond time scale.

Arbitrary waveform generation

The advantage of transition frequencies in the microwave regime lies in their ability to be directly synthesized using arbitrary waveform generators (AWGs). These days, AWGs are readily available commercial devices that enable the precise setting of electric field values with resolutions as fine as a few picoseconds. Consequently, one can program a predefined waveform and transmit it to the Rydberg atoms once the AWG is triggered. Depending on the choice of Rydberg state and the AWG, the transition frequency cannot be directly generated and needs to be up-converted with a frequency mixer. During this thesis, we worked with $n = 48$ and 61 corresponding to transition frequencies of ~ 35 and 16 GHz between $|nS\rangle$ and $|nP\rangle$, respectively.

Frequency up-conversion During this work, two AWGs with sampling rates of 5 GSa/s (Tabor SE5082) and 64 GSa/s (Keysight M8195A) have been used. Neither is able to directly generate a $\sim$ 35 GHz waveform needed to drive $|nS\rangle$ and $|nP\rangle$ transitions below $n = 49$. To overcome this limitation, we generate the arbitrary waveform at lower frequencies (intermediate frequency IF) and up-convert them using a high and constant-frequency local oscillator (LO: Anritsu MG3697, output frequency up to 67 GHz). The up-conversion is performed using a mixer (MM1-1467H), and the resulting sideband at frequency $\nu_{\mathrm{LO}} + \nu_{\mathrm{IF}}$ is used to drive the atomic transition (see [149] for details). During the mixing process, additional mixing sidebands appear, which might influence the quality of the driving in certain regimes.

Direct transition driving For $n > 49$, the waveform is directly synthesized using our 64 GSa/s AWG. This removes additional mixing sidebands, which are not affecting the quality of the drive anymore.

Transmitting the microwave field

Following the waveform generation, a horn antenna (SGH-22) is used to emit the radiation towards the atoms. A picture of the microwave setup is shown in Fig. B.5 a). The radiation pattern immediately after the horn is divergent, and we utilize a parabolic aluminum mirror to focus the radiation on the atoms. Fig. B.5 b) displays a COMSOL physics [212] simulation of the intensity pattern and is adapted from [149]. By employing this configuration, the radiation is directed outward from the steel chamber, effectively preventing back reflections. Furthermore, the polarization of the field is controlled to be linear using a wire grid polarizer. In our typical approach, we drive transitions from $m_j = 0.5$ to $m_j = 0.5$ using π polarized microwaves. This setup not only suppresses coupling to other Zeeman levels by shifting them with a magnetic field but also by exploiting polarization effects, which are essential to isolating a two-level system in the Rydberg manifold.

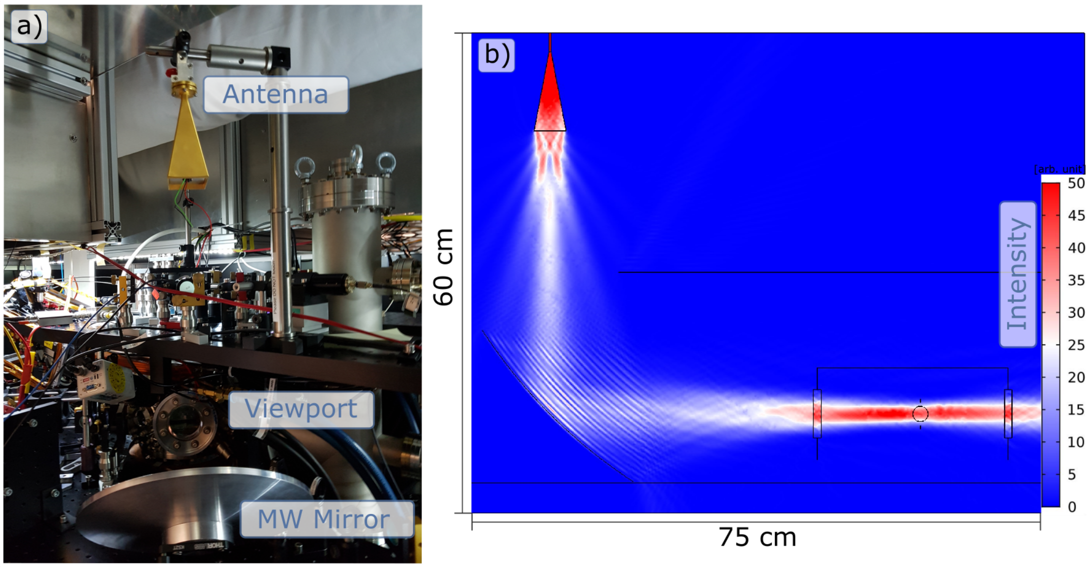

Figure B.5: The microwave setup. a) Picture of the experimental microwave setup. The horn antenna at the top is used to emit the microwave radiation. Afterwards a parabolic aluminum mirror focuses the field through the viewport at the atom position. **b)** COMSOL physics [212] simulations of the setup displaying the intensity pattern after the horn antenna. Adapted from [149].

B.2.1 Coherent spin manipulations

The experimental setup provides the capability for the application of arbitrary and fast spin-1/2 manipulations by controlling the phase, amplitude, and frequency of the microwave radiation. Assuming no interactions, a single spin evolves according to the Hamiltonian

$$\hat{H}_{\text{drive}}(t) = \sum_i \Omega(t) \left[\cos\phi(t) \hat{S}_x^i + \sin\phi(t) \hat{S}_y^i \right] + \Delta(t) \sum_i \hat{S}_z^i. \tag{B.1}$$

Here, $\Omega(t)$ is the time-dependent Rabi frequency of the drive, $\phi(t)$ the phase and $\Delta(t)$ the detuning of the field with respect to the transition resonance. We employ the ability to perform fast time-dependent spin manipulations through out this thesis. By applying this drive to the two isolated levels within our Rydberg manifold, we can observe typical Rabi oscillations and atomic spectra, as illustrated in Fig. B.6.

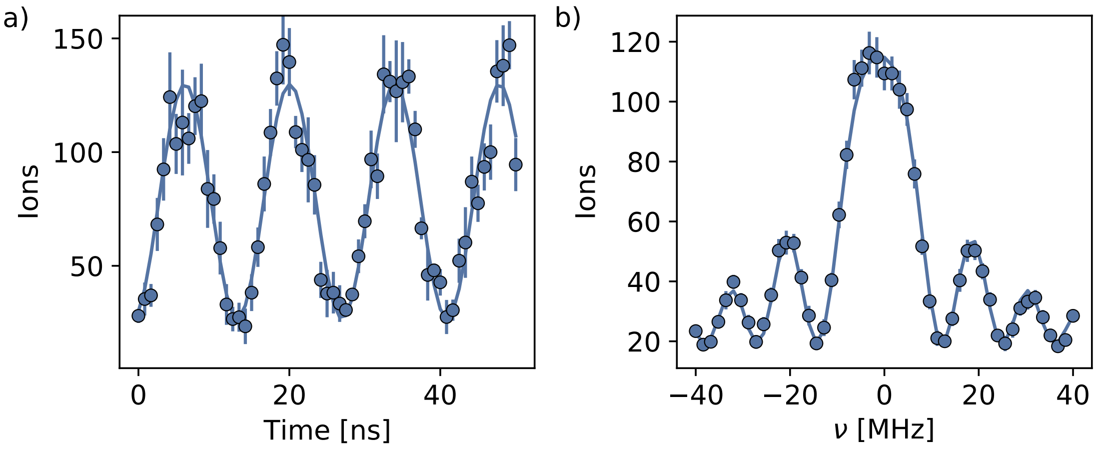

Figure B.6: Coherent microwave spin manipulations. a) Rabi oscillations between $|48S_{1/2}, m_j = 1/2\rangle$ and $|48P_{3/2}, m_j = 1/2\rangle$. Y-axis displays the number of ions in $|48P_{3/2}, m_j = 1/2\rangle$ after de-exciting $|48S_{1/2}, m_j = 1/2\rangle$. Solid line is a damped cosine fit with a Rabi frequency of $\Omega/2\pi = 72$ MHz. **b)** Spectrum of the same transition taken with $\Omega/2\pi = 15$ MHz at $t = 100$ ns. Solid line displays a fit with the Rabi formular $A\frac{\Omega^2}{\Omega_{\text{eff}}^2} \cdot \sin^2(2\pi \cdot \Omega_{\text{eff}} t) + \text{offset}$ with the effective Rabi frequency $\Omega_{\text{eff}} = \sqrt{\Omega^2 + \nu^2}$. We subtracted the transition frequency of 35062 MHz.

Achieving such fast Rabi oscillations on the order of up to $\sim$ 100 MHz allows to implement these manipulations faster than the typical interaction timescales in our system, which are on the order of a few MHz.

B.2.2 Tomographic magnetization readout

The experiments in this thesis mainly focus on measuring the magnetization dynamics of a many-body state. The following discussion on how the magnetization is mapped out closely follows the description in [50]. This procedure is based on a tomographic readout using $\pi/2$ microwave pulses. We consider a given state, composed of atoms in $|\downarrow\rangle$ and $|\uparrow\rangle$. The detection is performed by measuring the number of ions in the $|\uparrow\rangle$ states after de-exciting the $|\downarrow\rangle$ states as described previously.

To reconstruct the full magnetization of a state, we furthermore measured dif-

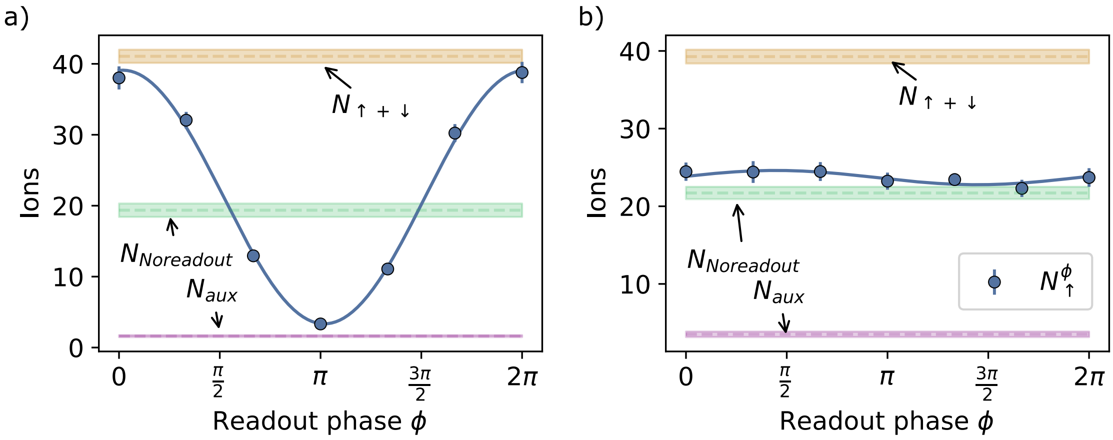

Figure B.7: Tomographic readout of the magnetization. a) Example of the readout components of a fully magnetized state in the equatorial plane in a Bloch sphere. Blue points correspond to the ion number $N_{\uparrow}^{\phi}$ in $|\uparrow\rangle$ after the $\pi/2$ readout pulse with phase ϕ and deexcitation of $|\downarrow\rangle$. The solid line corresponds to a fit $A \cdot \sin(\phi + \phi_0) + c$. The ion numbers N_{aux}, $N_{Noreadout}$ and $N_{\uparrow+\downarrow}$ are respectively shown by the dashed purple, green and yellow line and are taken without readout pulse. **b)** Readout for a state after magnetization relaxation, where the phase contrast is lost.

ferent quantities in multiple runs of the experiment: the total number of ions $N_{\uparrow+\downarrow}$, by ionizing the sample without de-exciting $|\downarrow\rangle$. The number of ions in $|\uparrow\rangle$ after de-excitation of $|\downarrow\rangle$ ($N_{Noreadout}$). The number of ions in $|\uparrow\rangle$ after a $\pi/2$ readout pulse with variable phase ϕ ($N_{\uparrow}^{\phi}$). In the Rydberg excitation and due to the finite lifetime, one might slightly populate surrounding auxiliary Rydberg states that can not be de-excited. These states lead to an offset in the measured ion number which we denote N_{aux}. N_{aux} is determined by first exciting atoms to $|\downarrow\rangle$, then allowing them to remain in this state for the duration of the experiment, and finally de-exciting the atoms back to the ground state and ionizing the auxiliary ions. These quantities allow us to reconstruct the system's magnetization in the following way. The z magnetization is determined by $N_{Noreadout}$ and $N_{\uparrow+\downarrow}$, which are corrected by the N_{aux} offset: $\mathrm{M_z} = \frac{\mathrm{N_{Noreadout}} - \mathrm{N_{aux}}}{\mathrm{N_{\uparrow+\downarrow}} - \mathrm{N_{aux}}} - \frac{1}{2}$, $\mathrm{M}_{\phi} = \frac{\mathrm{N}_{\uparrow}^{\phi} - \mathrm{N_{aux}}}{\mathrm{N_{\uparrow+\downarrow}} - \mathrm{N_{aux}}} - \frac{1}{2}$. Furthermore, the ion number $N_{\uparrow}^{\phi}$ of the tomographic readout is a sinusoidal function in ϕ with an amplitude of A

given by the contrast in ion numbers. The magnetization in the equatorial plane is reconstructed by the contrast in the phase readout as well as N_{aux} and $N_{\uparrow+\downarrow}$ such that $\mathrm{M}_{\mathrm{equatorial}} = \frac{\mathrm{A}}{\mathrm{N}_{\uparrow+\downarrow}-\mathrm{N}_{\mathrm{aux}}} - \frac{1}{2}$. Taking the phase into account directly translates to the x (M_{x}) and y magnetization (M_{y}).

Fig. B.7 illustrates measurements of the quantities for a state initially polarized in the equatorial plane (by a $\pi/2$ pulse) for early times (fully magnetized, full phase contrast: a)) and late times (after relaxation, no phase contrast: b)).

APPENDIX C

Relaxation of the magnetization under an XYZ Hamiltonian[1]

We derive the time evolution of the magnetization using the Heisenberg equation of motion for the general case of an XYZ Hamiltonian as given by Eq. 3.6 in the main text. Considering $\hat{S}_z = \sum_i \hat{S}^i_z$, $\hat{S}_x = \sum_i \hat{S}^i_x$, $\hat{S}_y = \sum_i \hat{S}^i_y$ we obtain

- $d\hat{S}_x/dt = i/\hbar[\hat{S}_x, \hat{H}_{\text{XYZ}}] = (\delta_z - \delta_y)\left[3\sum_{i,j,i\neq j} J_{ij}\left(\hat{S}^i_z\hat{S}^j_y + \hat{S}^j_z\hat{S}^i_y\right)/(2\hbar)\right]$
- $d\hat{S}_y/dt = i/\hbar[\hat{S}_y, \hat{H}_{\text{XYZ}}] = (\delta_x - \delta_z)\left[3\sum_{i,j,i\neq j} J_{ij}\left(\hat{S}^i_x S^j_z + \hat{S}^j_x\hat{S}^i_z\right)/(2\hbar)\right]$
- $d\hat{S}_z/dt = i/\hbar[\hat{S}_z, \hat{H}_{\text{XYZ}}] = -(\delta_x - \delta_y)\left[3\sum_{i,j,i\neq j} J_{ij}\left(\hat{S}^i_y\hat{S}^j_x + \hat{S}^j_y\hat{S}^i_x\right)/(2\hbar)\right]$

In the scenario of the engineering of an XXX Hamiltonian, $\delta_y = \delta_x = \delta_z$ which implies $[\hat{S}_x, \hat{H}_{\text{XYZ}}] = 0$, $[\hat{S}_y, \hat{H}_{\text{XYZ}}] = 0$ and $[\hat{S}_z, \hat{H}_{\text{XYZ}}] = 0$. All the components $\hat{S}_x$, $\hat{S}_y$, $\hat{S}_z$ are constant of motions of the system associated to the presence of the $SU(2)$ symmetry. Thus, the total magnetization constitutes a conserved quantity. For an XXZ Hamiltonian, $\delta_y = \delta_x$ which implies $[\hat{S}_z, \hat{H}_{\text{XYZ}}] = 0$. S_z constitutes then a constant of motion which is associated to the presence of the $U(1)$ symmetry in the system. For an XYZ Hamiltonian ($\delta_x \neq \delta_y \neq \delta_z$), there is no constant of motion due to the fact that all unitary symmetries are broken. More specifically,

---

[1] Taken from [71] (Supplemental Material)and slightly adapted.

the dynamics of a component $\hat{S}_x$ for example scales with the difference between δ_z and δ_y. Qualitatively, the relaxation dynamics of $\hat{S}_x$ will be faster if the value $\delta_z - \delta_y$ is important. This reasoning can be applied to all the components and explains the faster relaxation observed for the $z-$component compared to $y-$component in Fig. 3.8.

Bibliography

[1] A. Einstein, B. Podolsky, and N. Rosen. Can quantum-mechanical description of physical reality be considered complete? *Phys. Rev.*, 47:777–780, May 1935.

[2] Walther Gerlach and Otto Stern. Der experimentelle nachweis der richtungsquantelung im magnetfeld. *Zeitschrift für Physik*, 9(1):349–352, Dec 1922.

[3] Alain Aspect, Jean Dalibard, and Gérard Roger. Experimental test of bell's inequalities using time-varying analyzers. *Phys. Rev. Lett.*, 49:1804–1807, Dec 1982.

[4] Stuart J. Freedman and John F. Clauser. Experimental test of local hidden-variable theories. *Phys. Rev. Lett.*, 28:938–941, Apr 1972.

[5] Dik Bouwmeester, Jian-Wei Pan, Klaus Mattle, Manfred Eibl, Harald Weinfurter, and Anton Zeilinger. Experimental quantum teleportation. *Nature*, 390(6660):575–579, Dec 1997.

[6] K. Binder and A. P. Young. Spin glasses: Experimental facts, theoretical concepts, and open questions. *Rev. Mod. Phys.*, 58:801–976, Oct 1986.

[7] Richard P. Feynman. Simulating physics with computers. *International Journal of Theoretical Physics*, 21(6):467–488, Jun 1982.

[8] John Parkinson and Damian J J Farnell. *An Introduction to Quantum Spin Systems*, volume 816 of *Lecture Notes in Physics*. Springer Berlin Heidelberg, Berlin, Heidelberg, 2010.

[9] Masahito Ueda. Quantum equilibration, thermalization and prethermalization in ultracold atoms. *Nature Reviews Physics*, 2(12):669–681, December 2020.

[10] Rahul Nandkishore and David A. Huse. Many-body localization and thermalization in quantum statistical mechanics. *Annual Review of Condensed Matter Physics*, 6(1):15–38, 2015.

[11] Wolfgang Paul. Electromagnetic traps for charged and neutral particles. *Rev. Mod. Phys.*, 62:531–540, Jul 1990.

[12] Hans Dehmelt. Experiments with an isolated subatomic particle at rest. *Rev. Mod. Phys.*, 62:525–530, Jul 1990.

[13] William D. Phillips. Nobel lecture: Laser cooling and trapping of neutral atoms. *Rev. Mod. Phys.*, 70:721–741, Jul 1998.

[14] Steven Chu. Nobel lecture: The manipulation of neutral particles. *Rev. Mod. Phys.*, 70:685–706, Jul 1998.

[15] Claude N. Cohen-Tannoudji. Nobel lecture: Manipulating atoms with photons. *Rev. Mod. Phys.*, 70:707–719, Jul 1998.

[16] Serge Haroche. Nobel lecture: Controlling photons in a box and exploring the quantum to classical boundary. *Rev. Mod. Phys.*, 85:1083–1102, Jul 2013.

[17] I. M. Georgescu, S. Ashhab, and Franco Nori. Quantum simulation. *Rev. Mod. Phys.*, 86:153–185, Mar 2014.

[18] Ehud Altman, Kenneth R. Brown, Giuseppe Carleo, Lincoln D. Carr, Eugene Demler, Cheng Chin, Brian DeMarco, Sophia E. Economou, Mark A. Eriksson, Kai-Mei C. Fu, Markus Greiner, Kaden R.A. Hazzard, Randall G. Hulet, Alicia J. Kollár, Benjamin L. Lev, Mikhail D. Lukin, Ruichao Ma, Xiao Mi, Shashank Misra, Christopher Monroe, Kater Murch, Zaira Nazario, Kang-Kuen Ni, Andrew C. Potter, Pedram Roushan, Mark Saffman, Monika Schleier-Smith, Irfan Siddiqi, Raymond Simmonds, Meenakshi Singh, I.B.

Spielman, Kristan Temme, David S. Weiss, Jelena Vucković, Vladan Vuletić, Jun Ye, and Martin Zwierlein. Quantum simulators: Architectures and opportunities. *PRX Quantum*, 2:017003, Feb 2021.

[19] J. Hubbard and Brian Hilton Flowers. Electron correlations in narrow energy bands. *Proceedings of the Royal Society of London. Series A. Mathematical and Physical Sciences*, 276(1365):238–257, 1963.

[20] Daniel P. Arovas, Erez Berg, Steven A. Kivelson, and Srinivas Raghu. The hubbard model. *Annual Review of Condensed Matter Physics*, 13(1):239–274, 2022.

[21] Immanuel Bloch, Jean Dalibard, and Sylvain Nascimbène. Quantum simulations with ultracold quantum gases. *Nature Physics*, 8(4):267–276, Apr 2012.

[22] Immanuel Bloch, Jean Dalibard, and Wilhelm Zwerger. Many-body physics with ultracold gases. *Reviews of Modern Physics*, 80(3):885–964, July 2008.

[23] Tilman Esslinger. Fermi-hubbard physics with atoms in an optical lattice. *Annual Review of Condensed Matter Physics*, 1(1):129–152, 2010.

[24] Florian Schäfer, Takeshi Fukuhara, Seiji Sugawa, Yosuke Takasu, and Yoshiro Takahashi. Tools for quantum simulation with ultracold atoms in optical lattices. *Nature Reviews Physics*, 2(8):411–425, Aug 2020.

[25] W. Heisenberg. Zur theorie des ferromagnetismus. *Zeitschrift für Physik*, 49(9):619–636, Sep 1928.

[26] H. Bethe. Zur theorie der metalle. *Zeitschrift für Physik*, 71(3):205–226, Mar 1931.

[27] R. Blatt and C. F. Roos. Quantum simulations with trapped ions. *Nature Physics*, 8(4):277–284, 2012.

[28] J. I. Cirac and P. Zoller. Quantum Computations with Cold Trapped Ions. *Physical Review Letters*, 74(20):4091–4094, May 1995.

[29] B. P. Lanyon, C. Hempel, D. Nigg, M. Müller, R. Gerritsma, F. Zähringer, P. Schindler, J. T. Barreiro, M. Rambach, G. Kirchmair, M. Hennrich, P. Zoller, R. Blatt, and C. F. Roos. Universal Digital Quantum Simulation with Trapped Ions. *Science*, 334(6052):57–61, October 2011.

[30] C. Monroe, W. C. Campbell, L.-M. Duan, Z.-X. Gong, A. V. Gorshkov, P. W. Hess, R. Islam, K. Kim, N. M. Linke, G. Pagano, P. Richerme, C. Senko, and N. Y. Yao. Programmable quantum simulations of spin systems with trapped ions. *Rev. Mod. Phys.*, 93:025001, Apr 2021.

[31] Bo Yan, Steven A. Moses, Bryce Gadway, Jacob P. Covey, Kaden R. A. Hazzard, Ana Maria Rey, Deborah S. Jin, and Jun Ye. Observation of dipolar spin-exchange interactions with lattice-confined polar molecules. *Nature*, 501(7468):521–525, September 2013.

[32] Jun-Ru Li, Kyle Matsuda, Calder Miller, Annette N. Carroll, William G. Tobias, Jacob S. Higgins, and Jun Ye. Tunable itinerant spin dynamics with polar molecules. *Nature*, 614(7946):70–74, February 2023.

[33] Lysander Christakis, Jason S. Rosenberg, Ravin Raj, Sungjae Chi, Alan Morningstar, David A. Huse, Zoe Z. Yan, and Waseem S. Bakr. Probing site-resolved correlations in a spin system of ultracold molecules. *Nature*, 614(7946):64–69, February 2023.

[34] D. DeMille. Quantum computation with trapped polar molecules. *Phys. Rev. Lett.*, 88:067901, Jan 2002.

[35] Y. L. Zhou, M. Ortner, and P. Rabl. Long-range and frustrated spin-spin interactions in crystals of cold polar molecules. *Phys. Rev. A*, 84:052332, Nov 2011.

[36] Y. Nakamura, Yu. A. Pashkin, and J. S. Tsai. Coherent control of macroscopic quantum states in a single-Cooper-pair box. *Nature*, 398(6730):786–788, April 1999.

[37] Irfan Siddiqi. Engineering high-coherence superconducting qubits. *Nature Reviews Materials*, 6(10):875–891, Oct 2021.

[38] A. Wallraff, D. I. Schuster, A. Blais, L. Frunzio, R.-. S. Huang, J. Majer, S. Kumar, S. M. Girvin, and R. J. Schoelkopf. Strong coupling of a single photon to a superconducting qubit using circuit quantum electrodynamics. *Nature*, 431(7005):162–167, Sep 2004.

[39] Hendrik Weimer, Markus Müller, Igor Lesanovsky, Peter Zoller, and Hans Peter Büchler. A Rydberg quantum simulator. *Nature Physics*, 6(5):382–388, May 2010.

[40] M. Saffman, T. G. Walker, and K. Mølmer. Quantum information with rydberg atoms. *Rev. Mod. Phys.*, 82:2313–2363, Aug 2010.

[41] C S Adams, J D Pritchard, and J P Shaffer. Rydberg atom quantum technologies. *Journal of Physics B: Atomic, Molecular and Optical Physics*, 53(1):012002, dec 2019.

[42] Jongseok Lim, Han-gyeol Lee, and Jaewook Ahn. Review of cold rydberg atoms and their applications. *Journal of the Korean Physical Society*, 63(4):867–876, Aug 2013.

[43] Antoine Browaeys and Thierry Lahaye. Many-body physics with individually controlled Rydberg atoms. *Nature Physics*, 16(2):132–142, February 2020.

[44] Thomas F. Gallagher. *Rydberg atoms*, volume 3 of *Cambridge monographs on atomic, molecular, and chemical physics.* Cambridge University Press, Cambridge, 1994.

[45] Daniel Barredo, Henning Labuhn, Sylvain Ravets, Thierry Lahaye, Antoine Browaeys, and Charles S. Adams. Coherent Excitation Transfer in a Spin Chain of Three Rydberg Atoms. *Physical Review Letters*, 114(11):113002, March 2015.

[46] Sylvain De Léséleuc, Vincent Lienhard, Pascal Scholl, Daniel Barredo, Sebastian Weber, Nicolai Lang, Hans Peter Büchler, Thierry Lahaye, and Antoine Browaeys. Observation of a symmetry-protected topological phase of interacting bosons with Rydberg atoms. *Science*, 365(6455):775–780, August 2019.

[47] Cheng Chen, Guillaume Bornet, Marcus Bintz, Gabriel Emperauger, Lucas Leclerc, Vincent S. Liu, Pascal Scholl, Daniel Barredo, Johannes Hauschild, Shubhayu Chatterjee, Michael Schuler, Andreas M. Läuchli, Michael P. Zaletel, Thierry Lahaye, Norman Y. Yao, and Antoine Browaeys. Continuous symmetry breaking in a two-dimensional Rydberg array. *Nature*, 616(7958):691–695, April 2023.

[48] P. Scholl, H. J. Williams, G. Bornet, F. Wallner, D. Barredo, L. Henriet, A. Signoles, C. Hainaut, T. Franz, S. Geier, A. Tebben, A. Salzinger, G. Zürn, T. Lahaye, M. Weidemüller, and A. Browaeys. Microwave Engineering of Programmable X X Z Hamiltonians in Arrays of Rydberg Atoms. *PRX Quantum*, 3(2):020303, April 2022.

[49] Asier P. Orioli, A. Signoles, H. Wildhagen, G. Günter, J. Berges, S. Whitlock, and M. Weidemüller. Relaxation of an isolated dipolar-interacting rydberg quantum spin system. *Phys. Rev. Lett.*, 120:063601, Feb 2018.

[50] A. Signoles, T. Franz, R. Ferracini Alves, M. Gärttner, S. Whitlock, G. Zürn, and M. Weidemüller. Glassy Dynamics in a Disordered Heisenberg Quantum Spin System. *Physical Review X*, 11(1):011011, January 2021.

[51] Pascal Scholl, Michael Schuler, Hannah J. Williams, Alexander A. Eberharter, Daniel Barredo, Kai-Niklas Schymik, Vincent Lienhard, Louis-Paul Henry, Thomas C. Lang, Thierry Lahaye, Andreas M. Läuchli, and Antoine Browaeys. Quantum simulation of 2d antiferromagnets with hundreds of rydberg atoms. *Nature*, 595(7866):233–238, Jul 2021.

[52] Hannes Bernien, Sylvain Schwartz, Alexander Keesling, Harry Levine, Ahmed Omran, Hannes Pichler, Soonwon Choi, Alexander S. Zibrov, Manuel Endres, Markus Greiner, Vladan Vuletić, and Mikhail D. Lukin. Probing many-body dynamics on a 51-atom quantum simulator. *Nature*, 551(7682):579–584, November 2017.

[53] Sylvain de Léséleuc, Sebastian Weber, Vincent Lienhard, Daniel Barredo, Hans Peter Büchler, Thierry Lahaye, and Antoine Browaeys. Accurate mapping of multilevel rydberg atoms on interacting spin-1/2 particles for the quantum simulation of ising models. *Phys. Rev. Lett.*, 120:113602, Mar 2018.

[54] Alexander Keesling, Ahmed Omran, Harry Levine, Hannes Bernien, Hannes Pichler, Soonwon Choi, Rhine Samajdar, Sylvain Schwartz, Pietro Silvi, Subir Sachdev, Peter Zoller, Manuel Endres, Markus Greiner, Vladan Vuletić, and Mikhail D. Lukin. Quantum Kibble–Zurek mechanism and critical dynamics on a programmable Rydberg simulator. *Nature*, 568(7751):207–211, April 2019.

[55] Sepehr Ebadi, Tout T. Wang, Harry Levine, Alexander Keesling, Giulia Semeghini, Ahmed Omran, Dolev Bluvstein, Rhine Samajdar, Hannes Pichler, Wen Wei Ho, Soonwon Choi, Subir Sachdev, Markus Greiner, Vladan Vuletić, and Mikhail D. Lukin. Quantum phases of matter on a 256-atom programmable quantum simulator. *Nature*, 595(7866):227–232, July 2021.

[56] G Semeghini, H Levine, A Keesling, S Ebadi, T T Wang, D Bluvstein, R Verresen, H Pichler, M Kalinowski, R Samajdar, A Omran, S Sachdev, A Vishwanath, M Greiner, V Vuletic, and M D Lukin. Probing topological spin liquids on a programmable quantum simulator. 2021.

[57] D. Bluvstein, A. Omran, H. Levine, A. Keesling, G. Semeghini, S. Ebadi, T. T. Wang, A. A. Michailidis, N. Maskara, W. W. Ho, S. Choi, M. Serbyn, M. Greiner, V. Vuletić, and M. D. Lukin. Controlling quantum many-body dynamics in driven rydberg atom arrays. *Science*, 371(6536):1355–1359, 2021.

[58] Manuel Endres, Hannes Bernien, Alexander Keesling, Harry Levine, Eric R. Anschuetz, Alexandre Krajenbrink, Crystal Senko, Vladan Vuletic, Markus Greiner, and Mikhail D. Lukin. Atom-by-atom assembly of defect-free one-dimensional cold atom arrays. *Science*, 354(6315):1024–1027, 2016.

[59] Daniel Barredo, Sylvain de Léséleuc, Vincent Lienhard, Thierry Lahaye, and Antoine Browaeys. An atom-by-atom assembler of defect-free arbitrary two-dimensional atomic arrays. *Science*, 354(6315):1021–1023, 2016.

[60] Daniel Barredo, Vincent Lienhard, Sylvain de Léséleuc, Thierry Lahaye, and Antoine Browaeys. Synthetic three-dimensional atomic structures assembled atom by atom. *Nature*, 561(7721):79–82, Sep 2018.

[61] Franz, Titus. Studies of out-of-equilibrium dynamics of disordered heisenberg spin models on a rydberg quantum simulator. *Dissertation, DOI: 10.11588/heidok.00032379*, 2022.

[62] Markus Greiner, Olaf Mandel, Tilman Esslinger, Theodor W. Hänsch, and Immanuel Bloch. Quantum phase transition from a superfluid to a mott insulator in a gas of ultracold atoms. *Nature*, 415(6867):39–44, Jan 2002.

[63] W. S. Bakr, A. Peng, M. E. Tai, R. Ma, J. Simon, J. I. Gillen, S. Fölling, L. Pollet, and M. Greiner. Probing the Superfluid–to–Mott Insulator Transition at the Single-Atom Level. *Science*, 329(5991):547–550, July 2010.

[64] Immanuel Bloch. Ultracold quantum gases in optical lattices. *Nature Physics*, 1(1):23–30, October 2005.

[65] Adam M. Kaufman and Kang-Kuen Ni. Quantum science with optical tweezer arrays of ultracold atoms and molecules. *Nature Physics*, 17(12):1324–1333, December 2021.

[66] Loïc Anderegg, Lawrence W. Cheuk, Yicheng Bao, Sean Burchesky, Wolfgang Ketterle, Kang-Kuen Ni, and John M. Doyle. An optical tweezer array of ultracold molecules. *Science*, 365(6458):1156–1158, September 2019.

[67] Rainer Blatt and David Wineland. Entangled states of trapped atomic ions. *Nature*, 453(7198):1008–1015, June 2008.

[68] M. H. Devoret and R. J. Schoelkopf. Superconducting Circuits for Quantum Information: An Outlook. *Science*, 339(6124):1169–1174, March 2013.

[69] Yu Chen, C. Neill, P. Roushan, N. Leung, M. Fang, R. Barends, J. Kelly, B. Campbell, Z. Chen, B. Chiaro, A. Dunsworth, E. Jeffrey, A. Megrant, J. Y. Mutus, P. J. J. O'Malley, C. M. Quintana, D. Sank, A. Vainsencher, J. Wenner, T. C. White, Michael R. Geller, A. N. Cleland, and John M. Martinis. Qubit architecture with high coherence and fast tunable coupling. *Phys. Rev. Lett.*, 113:220502, Nov 2014.

[70] A. Piñeiro Orioli, A. Signoles, H. Wildhagen, G. Günter, J. Berges, S. Whitlock, and M. Weidemüller. Relaxation of an Isolated Dipolar-Interacting Rydberg Quantum Spin System. *Physical Review Letters*, 120(6):063601, February 2018.

[71] Sebastian Geier, Nithiwadee Thaicharoen, Clément Hainaut, Titus Franz, Andre Salzinger, Annika Tebben, David Grimshandl, Gerhard Zürn, and Matthias Weidemüller. Floquet Hamiltonian engineering of an isolated many-body spin system. *Science*, 374(6571):1149–1152, November 2021.

[72] Matthias Schmidt, Stephanie M. Bohaichuk, Vijin Venu, Florian Christaller, Chang Liu, Fabian Ripka, Harald Kübler, and James P. Shaffer. Rydberg atom-based radio frequency sensors: amplitude regime sensing, June 2023. arXiv:2307.00121 [physics].

[73] Sébastien Gleyzes, Stefan Kuhr, Christine Guerlin, Julien Bernu, Samuel Deléglise, Ulrich Busk Hoff, Michel Brune, Jean-Michel Raimond, and Serge

Haroche. Quantum jumps of light recording the birth and death of a photon in a cavity. *Nature*, 446(7133):297–300, March 2007.

[74] E. K. Dietsche, A. Larrouy, S. Haroche, J. M. Raimond, M. Brune, and S. Gleyzes. High-sensitivity magnetometry with a single atom in a superposition of two circular Rydberg states. *Nature Physics*, 15(4):326–329, April 2019.

[75] Shuo Ma, Genyue Liu, Pai Peng, Bichen Zhang, Sven Jandura, Jahan Claes, Alex P. Burgers, Guido Pupillo, Shruti Puri, and Jeff D. Thompson. High-fidelity gates with mid-circuit erasure conversion in a metastable neutral atom qubit, May 2023. arXiv:2305.05493 [physics, physics:quant-ph].

[76] Pascal Scholl, Adam L. Shaw, Richard Bing-Shiun Tsai, Ran Finkelstein, Joonhee Choi, and Manuel Endres. Erasure conversion in a high-fidelity Rydberg quantum simulator, May 2023. arXiv:2305.03406 [cond-mat, physics:physics, physics:quant-ph].

[77] Dolev Bluvstein, Harry Levine, Giulia Semeghini, Tout T. Wang, Sepehr Ebadi, Marcin Kalinowski, Alexander Keesling, Nishad Maskara, Hannes Pichler, Markus Greiner, Vladan Vuletić, and Mikhail D. Lukin. A quantum processor based on coherent transport of entangled atom arrays. *Nature*, 604(7906):451–456, April 2022.

[78] A. Signoles, T. Franz, R. Ferracini Alves, M. Gärttner, S. Whitlock, G. Zürn, and M. Weidemüller. Glassy Dynamics in a Disordered Heisenberg Quantum Spin System. *Physical Review X*, 11(1):011011, January 2021.

[79] R. C. Stoneman, M. D. Adams, and T. F. Gallagher. Resonant-collision spectroscopy of rydberg atoms. *Phys. Rev. Lett.*, 58:1324–1327, Mar 1987.

[80] W. R. Anderson, J. R. Veale, and T. F. Gallagher. Resonant dipole-dipole energy transfer in a nearly frozen rydberg gas. *Phys. Rev. Lett.*, 80:249–252, Jan 1998.

[81] Robert J. Le Roy. Long-range potential coefficients from rkr turning points: C6 and c8 for b(3ou+)-state cl2, br2, and i2. *Canadian Journal of Physics*, 52(3):246–256, 1974.

[82] Sebastian Weber, Christoph Tresp, Henri Menke, Alban Urvoy, Ofer Firstenberg, Hans Peter Büchler, and Sebastian Hofferberth. Calculation of rydberg interaction potentials. *Journal of Physics B: Atomic, Molecular and Optical Physics*, 50(13):133001, jun 2017.

[83] M. E. Rose. The electrostatic interaction of two arbitrary charge distributions. *Journal of Mathematics and Physics*, 37(1-4):215–222, 1958.

[84] Peter R. Fontana. Theory of long-range interatomic forces. i. dispersion energies between unexcited atoms. *Phys. Rev.*, 123:1865–1870, Sep 1961.

[85] A. Dalgarno and W.D. Davison. The calculation of van der waals interactions. volume 2 of *Advances in Atomic and Molecular Physics*, pages 1–32. Academic Press, 1966.

[86] A. A. Kamenski, N. L. Manakov, S. N. Mokhnenko, and V. D. Ovsiannikov. Energy of van der waals and dipole-dipole interactions between atoms in rydberg states. *Phys. Rev. A*, 96:032716, Sep 2017.

[87] A. Reinhard, T. Cubel Liebisch, B. Knuffman, and G. Raithel. Level shifts of rubidium rydberg states due to binary interactions. *Phys. Rev. A*, 75:032712, Mar 2007.

[88] Nolan Samboy. Long-range interactions between rubidium and potassium rydberg atoms. *Phys. Rev. A*, 95:032702, Mar 2017.

[89] Robert Löw, Hendrik Weimer, Johannes Nipper, Jonathan B Balewski, Björn Butscher, Hans Peter Büchler, and Tilman Pfau. An experimental and theoretical guide to strongly interacting rydberg gases. *Journal of Physics B: Atomic, Molecular and Optical Physics*, 45(11):113001, may 2012.

[90] Th. Förster. Zwischenmolekulare energiewanderung und fluoreszenz. *Annalen der Physik*, 437(1-2):55–75, 1948.

[91] Sylvain Ravets, Henning Labuhn, Daniel Barredo, Lucas Béguin, Thierry Lahaye, and Antoine Browaeys. Coherent dipole–dipole coupling between two single Rydberg atoms at an electrically-tuned Förster resonance. *Nature Physics*, 10(12):914–917, December 2014.

[92] Thad G. Walker and M. Saffman. Consequences of zeeman degeneracy for the van der waals blockade between rydberg atoms. *Phys. Rev. A*, 77:032723, Mar 2008.

[93] A. Piñeiro Orioli, A. Signoles, H. Wildhagen, G. Günter, J. Berges, S. Whitlock, and M. Weidemüller. Relaxation of an isolated dipolar-interacting rydberg quantum spin system. *Phys. Rev. Lett.*, 120:063601, Feb 2018.

[94] Guillaume Bornet, Gabriel Emperauger, Cheng Chen, Bingtian Ye, Maxwell Block, Marcus Bintz, Jamie A. Boyd, Daniel Barredo, Tommaso Comparin, Fabio Mezzacapo, Tommaso Roscilde, Thierry Lahaye, Norman Y. Yao, and Antoine Browaeys. Scalable spin squeezing in a dipolar Rydberg atom array. *Nature*, August 2023.

[95] Shannon Whitlock, Alexander W Glaetzle, and Peter Hannaford. Simulating quantum spin models using rydberg-excited atomic ensembles in magnetic microtrap arrays. *Journal of Physics B: Atomic, Molecular and Optical Physics*, 50(7):074001, mar 2017.

[96] M. Heyl, A. Polkovnikov, and S. Kehrein. Dynamical Quantum Phase Transitions in the Transverse-Field Ising Model. *Physical Review Letters*, 110(13):135704, March 2013.

[97] J. Zhang, G. Pagano, P. W. Hess, A. Kyprianidis, P. Becker, H. Kaplan, A. V. Gorshkov, Z.-X. Gong, and C. Monroe. Observation of a many-body dynamical

phase transition with a 53-qubit quantum simulator. *Nature*, 551(7682):601–604, November 2017.

[98] Maksym Serbyn, Dmitry A. Abanin, and Zlatko Papić. Quantum many-body scars and weak breaking of ergodicity. *Nature Physics*, 17(6):675–685, June 2021.

[99] Dmitry A. Abanin, Ehud Altman, Immanuel Bloch, and Maksym Serbyn. *Colloquium* : Many-body localization, thermalization, and entanglement. *Reviews of Modern Physics*, 91(2):021001, May 2019.

[100] J. Smith, A. Lee, P. Richerme, B. Neyenhuis, P. W. Hess, P. Hauke, M. Heyl, D. A. Huse, and C. Monroe. Many-body localization in a quantum simulator with programmable random disorder. *Nature Physics*, 12(10):907–911, October 2016.

[101] Michael Schreiber, Sean S. Hodgman, Pranjal Bordia, Henrik P. Lüschen, Mark H. Fischer, Ronen Vosk, Ehud Altman, Ulrich Schneider, and Immanuel Bloch. Observation of many-body localization of interacting fermions in a quasirandom optical lattice. *Science*, 349(6250):842–845, August 2015.

[102] Alexander Lukin, Matthew Rispoli, Robert Schittko, M. Eric Tai, Adam M. Kaufman, Soonwon Choi, Vedika Khemani, Julian Léonard, and Markus Greiner. Probing entanglement in a many-body–localized system. *Science*, 364(6437):256–260, April 2019.

[103] Jae-yoon Choi, Sebastian Hild, Johannes Zeiher, Peter Schauß, Antonio Rubio-Abadal, Tarik Yefsah, Vedika Khemani, David A. Huse, Immanuel Bloch, and Christian Gross. Exploring the many-body localization transition in two dimensions. *Science*, 352(6293):1547–1552, June 2016.

[104] Anatoli Polkovnikov, Krishnendu Sengupta, Alessandro Silva, and Mukund Vengalattore. *Colloquium* : Nonequilibrium dynamics of closed interacting quantum systems. *Reviews of Modern Physics*, 83(3):863–883, August 2011.

[105] Pai Peng, Chao Yin, Xiaoyang Huang, Chandrasekhar Ramanathan, and Paola Cappellaro. Floquet prethermalization in dipolar spin chains. *Nature Physics*, 17(4):444–447, April 2021.

[106] Antonio Rubio-Abadal, Matteo Ippoliti, Simon Hollerith, David Wei, Jun Rui, SL Sondhi, Vedika Khemani, Christian Gross, and Immanuel Bloch. Floquet Prethermalization in a Bose-Hubbard System. *Physical Review X*, 10(2):021044, May 2020.

[107] Maximilian Prüfer, Philipp Kunkel, Helmut Strobel, Stefan Lannig, Daniel Linnemann, Christian-Marcel Schmied, Jürgen Berges, Thomas Gasenzer, and Markus K. Oberthaler. Observation of universal dynamics in a spinor Bose gas far from equilibrium. *Nature*, 563(7730):217–220, November 2018.

[108] Christoph Eigen, Jake A. P. Glidden, Raphael Lopes, Eric A. Cornell, Robert P. Smith, and Zoran Hadzibabic. Universal prethermal dynamics of Bose gases quenched to unitarity. *Nature*, 563(7730):221–224, November 2018.

[109] Leigh S. Martin, Hengyun Zhou, Nathaniel T. Leitao, Nishad Maskara, Oksana Makarova, Haoyang Gao, Qian-Ze Zhu, Mincheol Park, Matthew Tyler, Hongkun Park, Soonwon Choi, and Mikhail D. Lukin. Controlling local thermalization dynamics in a Floquet-engineered dipolar ensemble, September 2022.

[110] Giancarlo Benettin, Roberto Livi, and Giorgio Parisi. Ergodicity: How Can It Be Broken? *Large Deviations in Physics*, pages 29–70, 2014.

[111] Massimo Bernaschi, Alain Billoire, Andrea Maiorano, Giorgio Parisi, and Federico Ricci-Tersenghi. Strong ergodicity breaking in aging of mean-field spin glasses. *Proceedings of the National Academy of Sciences*, 117(30):17522–17527, July 2020.

[112] S. A. Parameswaran, Andrew C. Potter, and Romain Vasseur. Eigenstate phase transitions and the emergence of universal dynamics in highly excited states. *Annalen der Physik*, 529(7):1600302, 2017.

[113] Joonhee Choi, Soonwon Choi, Georg Kucsko, Peter C. Maurer, Brendan J. Shields, Hitoshi Sumiya, Shinobu Onoda, Junichi Isoya, Eugene Demler, Fedor Jelezko, Norman Y. Yao, and Mikhail D. Lukin. Depolarization Dynamics in a Strongly Interacting Solid-State Spin Ensemble. *Physical Review Letters*, 118(9):093601, March 2017.

[114] G. Kucsko, S. Choi, J. Choi, P. C. Maurer, H. Zhou, R. Landig, H. Sumiya, S. Onoda, J. Isoya, F. Jelezko, E. Demler, N. Y. Yao, and M. D. Lukin. Critical thermalization of a disordered dipolar spin system in diamond. *Phys. Rev. Lett.*, 121:023601, Jul 2018.

[115] Christian Sommer, Guido Pupillo, Nobuyuki Takei, Shuntaro Takeda, Akira Tanaka, Kenji Ohmori, and Claudiu Genes. Time-domain Ramsey interferometry with interacting Rydberg atoms. *Physical Review A*, 94(5):053607, November 2016.

[116] Nobuyuki Takei, Christian Sommer, Claudiu Genes, Guido Pupillo, Haruka Goto, Kuniaki Koyasu, Hisashi Chiba, Matthias Weidemüller, and Kenji Ohmori. Direct observation of ultrafast many-body electron dynamics in an ultracold Rydberg gas. *Nature Communications*, 7(1):13449, December 2016.

[117] P. Schultzen, T. Franz, S. Geier, A. Salzinger, A. Tebben, C. Hainaut, G. Zürn, M. Weidemüller, and M. Gärttner. Glassy quantum dynamics of disordered Ising spins. *Physical Review B*, 105(2):L020201, January 2022.

[118] P. Schultzen, T. Franz, C. Hainaut, S. Geier, A. Salzinger, A. Tebben, G. Zürn, M. Gärttner, and M. Weidemüller. Semiclassical simulations predict glassy dynamics for disordered Heisenberg models. *Physical Review B*, 105(10):L100201, March 2022.

[119] Titus Franz, Sebastian Geier, Clément Hainaut, Adrian Braemer, Nithiwadee Thaicharoen, Moritz Hornung, Eduard Braun, Martin Gärttner, Gerhard Zürn, and Matthias Weidemüller. Observation of universal relaxation dynamics in disordered quantum spin systems, September 2023. arXiv:2209.08080 [physics, physics:quant-ph].

[120] M. D. Lukin, M. Fleischhauer, R. Cote, L. M. Duan, D. Jaksch, J. I. Cirac, and P. Zoller. Dipole Blockade and Quantum Information Processing in Mesoscopic Atomic Ensembles. *Physical Review Letters*, 87(3):037901, June 2001.

[121] J. Schachenmayer, A. Pikovski, and A. M. Rey. Many-Body Quantum Spin Dynamics with Monte Carlo Trajectories on a Discrete Phase Space. *Physical Review X*, 5(1):011022, February 2015.

[122] Ronen Vosk and Ehud Altman. Many-Body Localization in One Dimension as a Dynamical Renormalization Group Fixed Point. *Physical Review Letters*, 110(6):067204, February 2013.

[123] David Pekker, Gil Refael, Ehud Altman, Eugene Demler, and Vadim Oganesyan. Hilbert-Glass Transition: New Universality of Temperature-Tuned Many-Body Dynamical Quantum Criticality. *Physical Review X*, 4(1):011052, March 2014.

[124] R. Vasseur, A. C. Potter, and S. A. Parameswaran. Quantum Criticality of Hot Random Spin Chains. *Physical Review Letters*, 114(21):217201, May 2015.

[125] Romain Vasseur, Aaron J. Friedman, S. A. Parameswaran, and Andrew C. Potter. Particle-hole symmetry, many-body localization, and topological edge modes. *Physical Review B*, 93(13):134207, April 2016.

[126] Adrian Braemer, Titus Franz, Matthias Weidemüller, and Martin Gärttner. Pair localization in dipolar systems with tunable positional disorder. *Physical Review B*, 106(13):134212, October 2022.

[127] Scholl, Pascal. Quantum simulation of spin models with large arrays of rydberg atoms. *Dissertation,⟨NNT : 2021UPASP130⟩. ⟨tel-03523082⟩*, 2021.

[128] Gaston Floquet. Sur les équations différentielles linéaires à coefficients périodiques. *Annales de l'École Normale Supérieure*, 12:47–88, 1883.

[129] N. Goldman and J. Dalibard. Periodically driven quantum systems: Effective hamiltonians and engineered gauge fields. *Phys. Rev. X*, 4:031027, Aug 2014.

[130] Jon H. Shirley. Solution of the schrödinger equation with a hamiltonian periodic in time. *Phys. Rev.*, 138:B979–B987, May 1965.

[131] P. Jurcevic, H. Shen, P. Hauke, C. Maier, T. Brydges, C. Hempel, B. P. Lanyon, M. Heyl, R. Blatt, and C. F. Roos. Direct observation of dynamical quantum phase transitions in an interacting many-body system. *Phys. Rev. Lett.*, 119:080501, Aug 2017.

[132] J. Zhang, P. W. Hess, A. Kyprianidis, P. Becker, A. Lee, J. Smith, G. Pagano, I. D. Potirniche, A. C. Potter, A. Vishwanath, N. Y. Yao, and C. Monroe. Observation of a discrete time crystal. *Nature*, 543(7644):217–220, 2017.

[133] Soonwon Choi, Joonhee Choi, Renate Landig, Georg Kucsko, Hengyun Zhou, Junichi Isoya, Fedor Jelezko, Shinobu Onoda, Hitoshi Sumiya, Vedika Khemani, and et al. Observation of discrete time-crystalline order in a disordered dipolar many-body system. *Nature*, 543(7644):221–225, Mar 2017.

[134] Xiao Mi, Matteo Ippoliti, Chris Quintana, Ami Greene, Zijun Chen, Jonathan Gross, Frank Arute, Kunal Arya, Juan Atalaya, Ryan Babbush, Joseph C. Bardin, Joao Basso, Andreas Bengtsson, Alexander Bilmes, Alexandre Bourassa, Leon Brill, Michael Broughton, Bob B. Buckley, David A. Buell, Brian Burkett, Nicholas Bushnell, Benjamin Chiaro, Roberto Collins, William Courtney, Dripto Debroy, Sean Demura, Alan R. Derk, Andrew Dunsworth, Daniel Eppens, Catherine Erickson, Edward Farhi, Austin G. Fowler, Brooks

Foxen, Craig Gidney, Marissa Giustina, Matthew P. Harrigan, Sean D. Harrington, Jeremy Hilton, Alan Ho, Sabrina Hong, Trent Huang, Ashley Huff, William J. Huggins, L. B. Ioffe, Sergei V. Isakov, Justin Iveland, Evan Jeffrey, Zhang Jiang, Cody Jones, Dvir Kafri, Tanuj Khattar, Seon Kim, Alexei Kitaev, Paul V. Klimov, Alexander N. Korotkov, Fedor Kostritsa, David Landhuis, Pavel Laptev, Joonho Lee, Kenny Lee, Aditya Locharla, Erik Lucero, Orion Martin, Jarrod R. McClean, Trevor McCourt, Matt McEwen, Kevin C. Miao, Masoud Mohseni, Shirin Montazeri, Wojciech Mruczkiewicz, Ofer Naaman, Matthew Neeley, Charles Neill, Michael Newman, Murphy Yuezhen Niu, Thomas E. O'Brien, Alex Opremcak, Eric Ostby, Balint Pato, Andre Petukhov, Nicholas C. Rubin, Daniel Sank, Kevin J. Satzinger, Vladimir Shvarts, Yuan Su, Doug Strain, Marco Szalay, Matthew D. Trevithick, Benjamin Villalonga, Theodore White, Z. Jamie Yao, Ping Yeh, Juhwan Yoo, Adam Zalcman, Hartmut Neven, Sergio Boixo, Vadim Smelyanskiy, Anthony Megrant, Julian Kelly, Yu Chen, S. L. Sondhi, Roderich Moessner, Kostyantyn Kechedzhi, Vedika Khemani, and Pedram Roushan. Time-crystalline eigenstate order on a quantum processor. *Nature*, 601(7894):531–536, January 2022.

[135] A. Kyprianidis, F. Machado, W. Morong, P. Becker, K. S. Collins, D. V. Else, L. Feng, P. W. Hess, C. Nayak, G. Pagano, N. Y. Yao, and C. Monroe. Observation of a prethermal discrete time crystal. *Science*, 372(6547):1192–1196, June 2021.

[136] Gregor Jotzu, Michael Messer, Rémi Desbuquois, Martin Lebrat, Thomas Uehlinger, Daniel Greif, and Tilman Esslinger. Experimental realization of the topological Haldane model with ultracold fermions. *Nature*, 515(7526):237–240, 2014.

[137] N. Fläschner, B. S. Rem, M. Tarnowski, D. Vogel, D.-S. Lühmann, K. Sengstock, and C. Weitenberg. Experimental reconstruction of the berry curvature in a floquet bloch band. *Science*, 352(6289):1091–1094, 2016.

[138] M. Aidelsburger, M. Atala, M. Lohse, J. T. Barreiro, B. Paredes, and I. Bloch. Realization of the Hofstadter Hamiltonian with Ultracold Atoms in Optical Lattices. *Physical Review Letters*, 111(18):185301, October 2013.

[139] Karen Wintersperger, Christoph Braun, F. Nur Ünal, André Eckardt, Marco Di Liberto, Nathan Goldman, Immanuel Bloch, and Monika Aidelsburger. Realization of an anomalous Floquet topological system with ultracold atoms. *Nature Physics*, 16(10):1058–1063, October 2020.

[140] Christian Schweizer, Fabian Grusdt, Moritz Berngruber, Luca Barbiero, Eugene Demler, Nathan Goldman, Immanuel Bloch, and Monika Aidelsburger. Floquet approach to $\mathbb{Z}_2$ lattice gauge theories with ultracold atoms in optical lattices. *Nature Physics*, 15(11):1168–1173, Sep 2019.

[141] Joonhee Choi, Hengyun Zhou, Helena S. Knowles, Renate Landig, Soonwon Choi, and Mikhail D. Lukin. Robust dynamic hamiltonian engineering of many-body spin systems. *Phys. Rev. X*, 10:031002, Jul 2020.

[142] Ashok Ajoy and Paola Cappellaro. Quantum simulation via filtered hamiltonian engineering: Application to perfect quantum transport in spin networks. *Phys. Rev. Lett.*, 110:220503, May 2013.

[143] E. L. Hahn. Spin echoes. *Phys. Rev.*, 80:580–594, Nov 1950.

[144] H. Y. Carr and E. M. Purcell. Effects of diffusion on free precession in nuclear magnetic resonance experiments. *Phys. Rev.*, 94:630–638, May 1954.

[145] J. S. Waugh, L. M. Huber, and U. Haeberlen. Approach to high-resolution nmr in solids. *Phys. Rev. Lett.*, 20:180–182, Jan 1968.

[146] Ken Xuan Wei, Chandrasekhar Ramanathan, and Paola Cappellaro. Exploring localization in nuclear spin chains. *Phys. Rev. Lett.*, 120:070501, Feb 2018.

[147] U. Haeberlen and J. S. Waugh. Coherent averaging effects in magnetic resonance. *Phys. Rev.*, 175:453–467, Nov 1968.

[148] Wilhelm Magnus. On the exponential solution of differential equations for a linear operator. *Communications on Pure and Applied Mathematics*, 7(4):649–673, 1954.

[149] Sebastian Geier. Engineering rydberg-spin hamiltonian using microwave pulse sequences. *Master Thesis*, 2019.

[150] Nicolas Schlosser, Georges Reymond, Igor Protsenko, and Philippe Grangier. Sub-poissonian loading of single atoms in a microscopic dipole trap. *Nature*, 411(6841):1024–1027, June 2001.

[151] Kaden R. A. Hazzard, Bryce Gadway, Michael Foss-Feig, Bo Yan, Steven A. Moses, Jacob P. Covey, Norman Y. Yao, Mikhail D. Lukin, Jun Ye, Deborah S. Jin, and Ana Maria Rey. Many-Body Dynamics of Dipolar Molecules in an Optical Lattice. *Physical Review Letters*, 113(19):195302, November 2014.

[152] Mario Collura, Andrea De Luca, and Jacopo Viti. Analytic solution of the domain-wall nonequilibrium stationary state. *Phys. Rev. B*, 97:081111, Feb 2018.

[153] Grégoire Misguich, Nicolas Pavloff, and Vincent Pasquier. Domain wall problem in the quantum XXZ chain and semiclassical behavior close to the isotropic point. *SciPost Phys.*, 7:025, 2019.

[154] Grégoire Misguich, Kirone Mallick, and P. L. Krapivsky. Dynamics of the spin-$\frac{1}{2}$ heisenberg chain initialized in a domain-wall state. *Phys. Rev. B*, 96:195151, Nov 2017.

[155] W. Morong, K.S. Collins, A. De, E. Stavropoulos, T. You, and C. Monroe. Engineering Dynamically Decoupled Quantum Simulations with Trapped Ions. *PRX Quantum*, 4(1):010334, March 2023.

[156] Paul Niklas Jepsen, Jesse Amato-Grill, Ivana Dimitrova, Wen Wei Ho, Eugene Demler, and Wolfgang Ketterle. Spin transport in a tunable Heisenberg model realized with ultracold atoms. *Nature*, 588(7838):403–407, December 2020.

[157] Brian Swingle. Unscrambling the physics of out-of-time-order correlators. *Nature Physics*, 14(10):988–990, October 2018.

[158] Hengyun Zhou, Haoyang Gao, Nathaniel T. Leitao, Oksana Makarova, Iris Cong, Alexander M. Douglas, Leigh S. Martin, and Mikhail D. Lukin. Robust Hamiltonian Engineering for Interacting Qudit Systems, May 2023. arXiv:2305.09757 [cond-mat, physics:quant-ph].

[159] E. L. Hahn. Spin echoes. *Phys. Rev.*, 80:580–594, Nov 1950.

[160] W-K. Rhim, A. Pines, and J. S. Waugh. Time-Reversal Experiments in Dipolar-Coupled Spin Systems. *Physical Review B*, 3(3):684–696, February 1971.

[161] D. Linnemann, H. Strobel, W. Muessel, J. Schulz, R. J. Lewis-Swan, K. V. Kheruntsyan, and M. K. Oberthaler. Quantum-enhanced sensing based on time reversal of nonlinear dynamics. *Phys. Rev. Lett.*, 117:013001, Jun 2016.

[162] Simone Colombo, Edwin Pedrozo-Peñafiel, Albert F. Adiyatullin, Zeyang Li, Enrique Mendez, Chi Shu, and Vladan Vuletić. Time-reversal-based quantum metrology with many-body entangled states. *Nature Physics*, 18(8):925–930, August 2022.

[163] Kevin A. Gilmore, Matthew Affolter, Robert J. Lewis-Swan, Diego Barberena, Elena Jordan, Ana Maria Rey, and John J. Bollinger. Quantum-enhanced sensing of displacements and electric fields with two-dimensional trapped-ion crystals. *Science*, 373(6555):673–678, August 2021.

[164] Emily Davis, Gregory Bentsen, and Monika Schleier-Smith. Approaching the heisenberg limit without single-particle detection. *Phys. Rev. Lett.*, 116:053601, Feb 2016.

[165] Jared Rovny, Robert L. Blum, and Sean E. Barrett. Observation of Discrete-Time-Crystal Signatures in an Ordered Dipolar Many-Body System. *Physical Review Letters*, 120(18):180603, May 2018.

[166] Martin Gärttner, Justin G. Bohnet, Arghavan Safavi-Naini, Michael L. Wall, John J. Bollinger, and Ana Maria Rey. Measuring out-of-time-order correlations and multiple quantum spectra in a trapped-ion quantum magnet. *Nature Physics*, 13(8):781–786, August 2017.

[167] Ken Xuan Wei, Chandrasekhar Ramanathan, and Paola Cappellaro. Exploring Localization in Nuclear Spin Chains. *Physical Review Letters*, 120(7):070501, February 2018. arXiv:1612.05249 [cond-mat, physics:quant-ph].

[168] Jochen Braumüller, Amir H. Karamlou, Yariv Yanay, Bharath Kannan, David Kim, Morten Kjaergaard, Alexander Melville, Bethany M. Niedzielski, Youngkyu Sung, Antti Vepsäläinen, Roni Winik, Jonilyn L. Yoder, Terry P. Orlando, Simon Gustavsson, Charles Tahan, and William D. Oliver. Probing quantum information propagation with out-of-time-ordered correlators. *Nature Physics*, 18(2):172–178, February 2022.

[169] Antoine Browaeys and Thierry Lahaye. Many-body physics with individually controlled rydberg atoms. *Nature Physics*, 16(2):132–142, Jan 2020.

[170] Gary Wolfowicz, F. Joseph Heremans, Christopher P. Anderson, Shun Kanai, Hosung Seo, Adam Gali, Giulia Galli, and David D. Awschalom. Quantum guidelines for solid-state spin defects. *Nature Reviews Materials*, 6(10):906–925, April 2021.

[171] A. Signoles, T. Franz, R. Ferracini Alves, M. Gärttner, S. Whitlock, G. Zürn, and M. Weidemüller. Glassy dynamics in a disordered heisenberg quantum spin system. *Phys. Rev. X*, 11:011011, Jan 2021.

[172] Geier S., Braemer A., Braun E., Müllenbach M., Franz T., Gärttner M., Zürn G., and Weidemüller M. Time-reversal in a quantum many-body spin system. *Manuscript*, 2023.

[173] A. Goussev, R. A. Jalabert, H. M. Pastawski, and D. Ariel Wisniacki. Loschmidt echo. *Scholarpedia*, 7(8):11687, 2012. revision #127578.

[174] Kaden R. A. Hazzard, Bryce Gadway, Michael Foss-Feig, Bo Yan, Steven A. Moses, Jacob P. Covey, Norman Y. Yao, Mikhail D. Lukin, Jun Ye, Deborah S. Jin, and Ana Maria Rey. Many-body dynamics of dipolar molecules in an optical lattice. *Phys. Rev. Lett.*, 113:195302, Nov 2014.

[175] Michael A. Perlin, Chunlei Qu, and Ana Maria Rey. Spin Squeezing with Short-Range Spin-Exchange Interactions. *Physical Review Letters*, 125(22):223401, November 2020.

[176] E.J. Robertson, N. **S**ibalić, R.M. Potvliege, and M.P.A. Jones. ARC 3.0: An expanded Python toolbox for atomic physics calculations. *Computer Physics Communications*, 261:107814, April 2021.

[177] K. Takegoshi and C. A. McDowell. A "magic echo" pulse sequence for the high-resolution NMR spectra of abundant spins in solids. *Chemical Physics Letters*, 116(2):100–104, 1985.

[178] Patrick A. Lee, Naoto Nagaosa, and Xiao-Gang Wen. Doping a mott insulator: Physics of high-temperature superconductivity. *Rev. Mod. Phys.*, 78:17–85, Jan 2006.

[179] Annabelle Bohrdt, Lukas Homeier, Christian Reinmoser, Eugene Demler, and Fabian Grusdt. Exploration of doped quantum magnets with ultracold atoms. *Annals of Physics*, 435:168651, 2021.

[180] Russell A. Hart, Pedro M. Duarte, Tsung-Lin Yang, Xinxing Liu, Thereza Paiva, Ehsan Khatami, Richard T. Scalettar, Nandini Trivedi, David A. Huse, and Randall G. Hulet. Observation of antiferromagnetic correlations in the Hubbard model with ultracold atoms. *Nature*, 519(7542):211–214, March 2015.

[181] Lawrence W. Cheuk, Matthew A. Nichols, Melih Okan, Thomas Gersdorf, Vinay V. Ramasesh, Waseem S. Bakr, Thomas Lompe, and Martin W. Zwierlein. Quantum-gas microscope for fermionic atoms. *Phys. Rev. Lett.*, 114:193001, May 2015.

[182] Anton Mazurenko, Christie S. Chiu, Geoffrey Ji, Maxwell F. Parsons, Márton Kanász-Nagy, Richard Schmidt, Fabian Grusdt, Eugene Demler, Daniel Greif, and Markus Greiner. A cold-atom Fermi–Hubbard antiferromagnet. *Nature*, 545(7655):462–466, May 2017.

[183] Maxwell F. Parsons, Florian Huber, Anton Mazurenko, Christie S. Chiu, Widagdo Setiawan, Katherine Wooley-Brown, Sebastian Blatt, and Markus Greiner. Site-resolved imaging of fermionic ^{6}Li in an optical lattice. *Phys. Rev. Lett.*, 114:213002, May 2015.

[184] Guillaume Salomon, Joannis Koepsell, Jayadev Vijayan, Timon A. Hilker, Jacopo Nespolo, Lode Pollet, Immanuel Bloch, and Christian Gross. Direct observation of incommensurate magnetism in Hubbard chains. *Nature*, 565(7737):56–60, January 2019.

[185] Ahmed Omran, Martin Boll, Timon A. Hilker, Katharina Kleinlein, Guillaume Salomon, Immanuel Bloch, and Christian Gross. Microscopic observation of pauli blocking in degenerate fermionic lattice gases. *Phys. Rev. Lett.*, 115:263001, Dec 2015.

[186] L.-M. Duan, E. Demler, and M. D. Lukin. Controlling spin exchange interactions of ultracold atoms in optical lattices. *Phys. Rev. Lett.*, 91:090402, Aug 2003.

[187] Hui Sun, Bing Yang, Han-Yi Wang, Zhao-Yu Zhou, Guo-Xian Su, Han-Ning Dai, Zhen-Sheng Yuan, and Jian-Wei Pan. Realization of a bosonic antiferromagnet. *Nature Physics*, 17(9):990–994, September 2021.

[188] Paul Niklas Jepsen, Wen Wei Ho, Jesse Amato-Grill, Ivana Dimitrova, Eugene Demler, and Wolfgang Ketterle. Transverse spin dynamics in the anisotropic heisenberg model realized with ultracold atoms. *Phys. Rev. X*, 11:041054, Dec 2021.

[189] Yuki Nakano, Takumi Ishima, Naohiro Kobayashi, Kazuhiko Sakakibara, Ikuo Ichinose, and Tetsuo Matsui. Finite-temperature phase diagram of the three-dimensional hard-core bosonic *t-j* model. *Phys. Rev. B*, 83:235116, Jun 2011.

[190] Lukas Homeier, Timothy J. Harris, Tizian Blatz, Ulrich Schollwöck, Fabian Grusdt, and Annabelle Bohrdt. Antiferromagnetic bosonic t-J models and their quantum simulation in tweezer arrays, May 2023. arXiv:2305.02322 [cond-mat, physics:quant-ph].

[191] Michael Knap, Adrian Kantian, Thierry Giamarchi, Immanuel Bloch, Mikhail D. Lukin, and Eugene Demler. Probing real-space and time-resolved correlation functions with many-body ramsey interferometry. *Phys. Rev. Lett.*, 111:147205, Oct 2013.

[192] Jad C. Halimeh, Lukas Homeier, Annabelle Bohrdt, and Fabian Grusdt. Spin exchange-enabled quantum simulator for large-scale non-Abelian gauge theories, May 2023. arXiv:2305.06373 [cond-mat, physics:hep-lat, physics:quant-ph].

[193] Titus Franz, Sebastian Geier, Clément Hainaut, Adrien Signoles, Nithiwadee Thaicharoen, Annika Tebben, André Salzinger, Adrian Braemer, Martin Gärt-

tner, Gerhard Zürn, and Matthias Weidemüller. Absence of thermalization in an interacting system of thousands of quantum spins. 2022.

[194] Frank Wilczek. Quantum time crystals. *Phys. Rev. Lett.*, 109:160401, Oct 2012.

[195] Haruki Watanabe and Masaki Oshikawa. Absence of quantum time crystals. *Phys. Rev. Lett.*, 114:251603, Jun 2015.

[196] N. Y. Yao, A. C. Potter, I.-D. Potirniche, and A. Vishwanath. Discrete time crystals: Rigidity, criticality, and realizations. *Phys. Rev. Lett.*, 118:030401, Jan 2017.

[197] D. Jaksch, J. I. Cirac, P. Zoller, S. L. Rolston, R. Côté, and M. D. Lukin. Fast Quantum Gates for Neutral Atoms. *Physical Review Letters*, 85(10):2208–2211, September 2000.

[198] Harry Levine, Alexander Keesling, Giulia Semeghini, Ahmed Omran, Tout T. Wang, Sepehr Ebadi, Hannes Bernien, Markus Greiner, Vladan Vuletić, Hannes Pichler, and Mikhail D. Lukin. Parallel Implementation of High-Fidelity Multiqubit Gates with Neutral Atoms. *Physical Review Letters*, 123(17):170503, October 2019.

[199] Daniel Comparat and Pierre Pillet. Dipole blockade in a cold rydberg atomic sample [invited]. *Journal of the Optical Society of America B*, 27(6):A208, Jun 2010.

[200] Hofmann, Christoph S. Emergence of correlations in strongly interacting ultracold rydberg gases. *Dissertation, DOI: 10.11588/heidok.00014629*, 2013.

[201] Günter, Georg Gotthilf. Interfacing rydberg atoms with light and observing their interaction driven dynamics. *Dissertation, DOI: 10.11588/heidok.00016312*, 2014.

[202] Schempp, Hanna. Formation of aggregates and energy transport in ultracold rydberg interacting gases. *Dissertation, DOI: 10.11588/heidok.00017202*, 2014.

[203] Tebben, Annika. Rydberg electromagnetically induced transparency. *Dissertation, DOI: 10.11588/heidok.00030661*, 2021.

[204] Harold J. Metcalf and Peter van der Straten. *Laser Cooling and Trapping of Neutral Atoms*. John Wiley and Sons, Ltd, 2007.

[205] Bastian Höltkemeier. 2d-mot as a source of a cold atom target. *Diploma Thesis*, 2011.

[206] C. S. Hofmann, G. Günter, H. Schempp, N. L. M. Müller, A. Faber, H. Busche, M. Robert-de Saint-Vincent, S. Whitlock, and M. Weidemüller. An experimental approach for investigating many-body phenomena in Rydberg-interacting quantum systems. *Frontiers of Physics*, 9(5):571–586, October 2014.

[207] Wolfgang Petrich, Michael H. Anderson, Jason R. Ensher, and Eric A. Cornell. Behavior of atoms in a compressed magneto-optical trap. *J. Opt. Soc. Am. B*, 11(8):1332–1335, Aug 1994.

[208] C. G. Townsend, N. H. Edwards, K. P. Zetie, C. J. Cooper, J. Rink, and C. J. Foot. High-density trapping of cesium atoms in a dark magneto-optical trap. *Phys. Rev. A*, 53:1702–1714, Mar 1996.

[209] Rudolf Grimm, Matthias Weidemüller, and Yurii B. Ovchinnikov. Optical dipole traps for neutral atoms. volume 42 of *Advances In Atomic, Molecular, and Optical Physics*, pages 95–170. Academic Press, 2000.

[210] WILLIAM HAPPER. Optical pumping. *Rev. Mod. Phys.*, 44:169–249, Apr 1972.

[211] Ferreira Cao, Miguel. Control and characterisation of a rydberg spin system to explore many-body physics. *Dissertation, DOI: 10.11588/heidok.00023769*, 2017.

[212] Comsol multiphysics® v. 6.1. www.comsol.com. comsol ab, stockholm, sweden.

Acknowledgments

The work presented in this thesis represents a collective effort of many great people and would not have been possible without the tremendous support from various individuals. At this point, I would like to express my heartfelt gratitude to all those without whom this work would not have been possible. Especially during such difficult times with the COVID-19 pandemic and the lab lock-downs.

First and foremost, I would like to thank **Matthias Weidemüller**, my advisor and mentor during my time at the Heidelberg Rydberg experiment. I deeply enjoyed all the stimulating discussions and the inspiration that came from the open research environment you fostered. Under your guidance, I felt the freedom to explore my ideas, and I truly appreciated the opportunity to learn and grow. I am also immensely grateful for the opportunity to spend half a year abroad, obtaining a diverse view on science and life.

I would like to convey my gratitude to **Markus Oberthaler** for reviewing this thesis and to the other committee members, **Jörg Evers** and **Tilman Enss**.

I am especially grateful to **Gerhard Zürn**, who essentially introduced me to quantum physics during my third semester and started my passion for cold atom research. I am genuinely thankful for all the discussions we've had and the guidance you've provided over the past several years. I also want to acknowledge **Martin Gärttner** for his invaluable insights whenever I encountered theoretical questions.

I would like to express my appreciation to **Clement Hainaut**. I thoroughly enjoyed every moment we spent tackling lab and technical challenges, and in the end, we always found solutions. I will also fondly remember the occasional post-work beers we shared. Best of luck in France! To **Nithiwadee Thaicharoen** (Pound!), I extend my gratitude. You not only taught me a lot about Rydberg physics but also valuable life lessons. I vividly recall the sleepless nights when we fine-tuned lasers. I always cherished our discussions and your unwavering support. Best wishes for your journey in Thailand!

Of course, I want to acknowledge all the members of the Rydberg team with whom I've shared the last couple of years. **Titus Franz**, our time together in the lab and our inspiring discussions were truly enjoyable. I also remember our "after work" gatherings and the wine-fueled brainstorming sessions in Paris that led to great ideas and experiments. **Annika Tebben**, working with you was a fantastic start to my PhD journey. You are such an enjoyable person and I remember great discussions. **Andre Salzinger**, thanks to you, I discovered some great new songs and always at some fun in the lab! **Eduard Braun**, I appreciated our stimulating discussions and will forever remember our little "adventure" in Tucson. **Valentina Salazar**, it was a pleasure spending the last months of my thesis journey with you, and I wish you the best of luck! I'd like to thank **Adrian Braemer** for our inspiring discussions and collaboration on several projects. **Niklas Euler**, I also enjoyed our discussions and meetings. I extend my gratitude to all the master's and bachelor's students **Alexander Müller, Theresa Gier, Maximilian Müllenbach, Philipp Schultzen, Moritz Hornung, Charlos Brandl, Sebastian Bok, Mathurin Choblet, David Grimshandl, Lorenz Luger, Julia Siegl and Karen Wadenpfuhl** and wish them the best of luck in their future endeavors. **Oliver Vorbach**, thank you for great support on technical questions!

I am also grateful to **Mikhail Lukin** for providing me with the opportunity to spend half a year in his group at Harvard. I learned immensely during this time and forged valuable friendships. A special thanks to the Atom Array 2 team: **Tout Wang, Simon Hollerith, Mohamed Abobeih, Allen Chiu, Tim Guo, and Pavel Stroganov**. I had an amazing time, even if I may not miss the super spicy food! I fondly recall our memorable trips to Montreal. I also want to thank the entire Atom Array 1 team and the entire CUA for their inspiring discussions. During this time, I truly appreciated the interactions with my german fellows **Lukas Homeier** and **Hannah Lange**.

I am further grateful for being a part of the wonderful collaboration with **Antoine Browaeys** and his group. It was incredible to witness and realize such a collaboration across Europe during the COVID-19 pandemic when travel was restricted. I gained a wealth of scientific and non-scientific knowledge during this time.

I extend my appreciation to all the funding sources that supported this research **the Heidelberg Graduate School for Physics HGSFP, the Collaborative Research Centre SFB ISOQUANT, the DFG Priority Program GiRyd, the FET flagship project PASQuanS and the Excellence Cluster STRUCTURES**. A special thank you goes to **Claudia Krämer**, who consistently assisted me with administrative matters. I further would like to thank all my friends along the way. A special thanks to **Lennart Singer**, with whom I've shared my life for almost 25 years now.

Finally, I want to express my deepest gratitude to my family. To my parents **Ulrike** and **Charly** and to my sister **Anna**, who have always been there for me and supported me throughout my life, I cannot find words to convey how thankful I am for your unwavering love and support. Most importantly, I would like to thank you, **Cathy**, for the amazing time we've shared so far and for always being there for me. Last but not least, I would also like to thank you, **Amina**, for always bringing a smile to my face in every situation.